Study of Interface Effects on Magnetization Reversal in Magnetic Structures with Perpendicular Magnetic Anisotropy

Xiaoxuan Zhao

université PARIS-SACLAY

NNT : 2019SACLS523

Thèse de doctorat

Etude des effets d'interfaces sur le retournement de l'aimantation dans des structures à anisotropie magnétique perpendiculaire

Study of Interface Effects on Magnetization Reversal in Magnetic Structures with Perpendicular Magnetic Anisotropy

Thèse de doctorat de Beihang University et de l'Université Paris-Saclay
préparée à l'Université Paris-Sud

ED n°575 EOBE | Electrical, optical, bio-physics and engineering
Spécialité de doctorat: Electronique et Optoélectronique, Nano-Microtechnologies

Thèse présentée et soutenue à Pékin, le 6 décembre 2019, par

Xiaoxuan Zhao

Composition du Jury :

Arnaud Bournel Professeur, Université Paris-Saclay	Président
Stéphane Mangin Professeur, Université de Lorraine, Insitute Jean Lamour	Rapporteur
Jianhua Zhao Professeur, Académie Chinoise des Sciences	Rapporteur
Tianxiao Nie Professeur, Université de Beihang	Examinateur
Dafiné Ravelosona Directeur de recherche CNRS, Orsay, C2N	Directeur de thèse
Weisheng Zhao Professeur, Université de Beihang	Co-Directeur de thèse

Acknowledgements

A journey in pursuit of PhD degree that witnessed excitements and frustrations, innovations and stupidities, etc. is to draw to a close. During this period, the difficulties and obstacles I encountered constantly urge me to strive and work hard. Without the help of my supervisors, my colleagues, my friends and my family, I would not be where I am today. Please allow me to extend my heartfelt thanks to all those people using this opportunity.

My doctoral study began in September 2016. I would like to give my sincere gratitude first and foremost to my supervisor Prof. Weisheng Zhao in Beihang University for offering me the opportunity to conduct my PhD research in his group. His consistent and illuminating instruction and belief in us endow me with confidence and courage to go through my PhD learning. His support for students can be found in many details. Even if I study abroad, when I am in trouble, I know very well that he is behind me.

During my second year in September 2017, I went to the lab of Centre de Nanosciences et de Nanotechnologies (C2N) in Université Paris-Saclay, where I met my co-supervisor, Prof. Dafiné Ravelosona. I sincerely appreciate him for he opened the door to the *irradiation technique* for me and defined the research direction for my PhD thesis. I learnt a lot from him, from how tiny magnets work and how to make a professional presentation to French idioms and authentic French culture. The time working with him in Paris is memorable and meaningful.

I am truly grateful to the members of my Thesis Defense Committee for their efforts to review my thesis. I sincerely give my thanks to the rapporteurs who wrote the reports for the manuscript and to the examiner and the president for their reading and evaluating my manuscript.

I would like to thank all the teachers and colleagues from Integnano group of C2N. I am especially grateful to Dr. Nicolas Vernier, Dr. Liza Herrera Diez and Mr. Sylvain Eimer. Most of my study in C2N was performed with the help of Dr. Nicolas Vernier, who taught me the knowledge of Kerr image microscopy and magnetic fundamentals. He is so enthusiastic and always ready to offer his kind help in both academic studies and daily life for me. Thanks go to Dr. Liza Herrera Diez in C2N, for she gave me valuable suggestions on my published paper, and also took much patience in revising it. Special thanks go to Mr. Sylvain Eimer, who cared for me when I was in Paris. Without him, my life in France would be less colorful.

Also thanks go to Mme Sophie Bouchoule, Mme Laurence Stephen and Prof. Eric Cassan from Doctoral School, for their assistance in my registration and thesis defense.

I am deeply indebted to all researchers and teachers in Beihang University, for their supports in my PhD research. Thanks go to all my colleagues and friends in the lab in Beihang University for their encouragement and company.

I would like to thank China Scholarship Council (CSC) for the financial support.

Finally, I am thankful to my family and relatives, especially my parents Mr. Xingzeng Zhao and Mrs Jing Liu. I am blessed to have parents who always unconditionally support and love me. I gratefully acknowledge their sacrifice for their only child. Then a big thank you goes to Dr. Hongchuan Wang, for his love and always back me up.

Xiaoxuan Zhao

08 October 2019, Beijing

CONTENTS

Abstract 1
Résumé 3
General Introduction 5
Chapter 1 Background and State-of-the-Art 7
1.1 Magnetic Random-Access Memory (MRAM) 7
1.1.1 Spin-transfer torque (STT)-MRAM 10
1.1.2 Spin-orbit torque (SOT)-MRAM 13
1.2 Domain wall dynamics 16
1.2.1 Field-driven DW motion 17
1.2.2 Spin orbit torque driven DW motion 21
1.3 Spin-dependent Interfacial effects in HM/FM/Oxide structure 22
1.3.1 Perpendicular magnetic anisotropy in HM-CoFeB-MgO structures 23
1.3.2 Interfacial Dzyaloshinskii-Moriya Interaction (DMI) 26
1.4 Summary 30
Chapter 2 Experimental Methods 31
2.1 Sample Fabrication 31
2.1.1 Ultra-thin film Sputtering 31
2.1.2 Magnetic Annealing 32
2.1.3 Hall bar Fabrication 33
2.1.4 Light-ion irradiation 35
2.2 Sample measurements and characterizations 38
2.2.1 Vibrating sample magnetometry (VSM) and superconducting quantum interference device (SQUID) for anisotropy measurements 38
2.2.2 Magneto-Optical Kerr Effect (MOKE) for Hysteresis Loop Measurements 39
2.2.3 Kerr miscopy for DW Imaging 40
2.2.4 Brillouin light scattering (BLS) for DMI measurements 43
2.2.5 Spin-dependent Electrical Transport Measurements 44
2.3 Summary 45
Chapter 3 Precise Modulation of Spin-Dependent Interfacial Effects 46
3.1 Modulation of magnetic anisotropy through different methods 46
3.1.1 FM thickness dependence of magnetic anisotropies 46
3.1.2 Dependence of magnetic anisotropy on sputtering 49
3.1.3 Dependence of magnetic anisotropy on annealing 51

3.1.4 Ion irradiation for post-control of magnetic properties 54
3.2 Modulation of DMI through different methods 57
3.2.1 Dependence of DMI on FM thickness and annealing conditions 57
3.2.2 Influence of the interfacial disorder induced by irradiation 59
3.3 Summary 61
Chapter 4 Ultra-Efficient Magnetic Switching in W/CoFeB/MgO Structures through SOT 63
4.1 Ultra-low switching current in perpendicularly magnetized sample 63
4.2 Dependence of SOT switching on depinning field 66
4.3 Dependence of SOT switching on DMI 67
4.4 Influence of spin Hall angle on SOT switching 69
4.5 Summary 71
Chapter 5 Modulation of SOT Magnetic Switching in W/CoFeB/MgO Structures by Ion Irradiation 72
5.1 Enhancement of DW velocity through irradiation 72
5.2 Irradiation induced high-efficient SOT magnetization switching 75
5.3 Spin orbit torque driven multi-state resistance in irradiated Hall cross 77
5.4 Summary 84
Conclusions and Perspectives 85
General conclusion 85
Perspectives 86
Bibliography 87
List of Abbreviations 99
List of Publications 100
Résumé en Français 102

Abstract

Magnetic Random-Access Memory (MRAM), as one of the emerging technologies, aims to be a “universal” memory device for a wide variety of applications. The combination of the spin orbit torque (SOT) resulting from the spin Hall effect (SHE) and the Dzyaloshinskii–Moriya interaction (DMI) at interfaces between heavy metals and ferromagnetic layers has been demonstrated to be a powerful means to drive domain-wall (DW) motion efficiently, which is expected to be promising for the next generation of information carriers owing to ultra-low driving currents and ultra-fast DW motion. However, the crucial limitation of SOT induced DW motion results from the presence of pinning defects that can induce large threshold currents and stochastic behaviors. Such pinning defects are strongly related to structural inhomogeneities at the interfaces between the ultra-thin ferromagnetic layer and the other materials (insulator and/or heavy metals) that induce a spatial distribution of magnetic properties such as perpendicular magnetic anisotropy (PMA) or DMI. Therefore, understanding the role of the interface structure on DW motion and DMI is crucial for the design of future low power devices.

It is under this innovative context that my Ph.D. research focuses on the modulation of spin-dependent interfacial effects for efficient SOT switching. Based on the mainstream structures of MRAM, the interfacial anisotropy, DMI, DW motion and SOT phenomena in HM-CoFeB-MgO have been studied. The innovative approach shown in this thesis is the introduction of light ion irradiation to control the degree of intermixing at interfaces, for the modulation of spin-dependent interfacial effects. In W-CoFeB-MgO structures with high DMI, we have observed a large increase of the DW velocity in the creep regime upon He^+ irradiation, which is attributed to the reduction of pinning centers induced by interface intermixing. Asymmetric in-plane field-driven domain expansion experiments show that the DMI value is slightly reduced upon irradiation, and a direct relationship between DMI and interface anisotropy is demonstrated. Using local irradiated Hall bars in SOT devices, we further demonstrate that the current density for SOT induced magnetization switching through DW motion can be significantly reduced by irradiation. Ultra-efficient SOT switching and multi-level resistances can be then obtained, providing a way to build up ultra-low power and high density spintronic devices for neuromorphic computing.

Keywords: Spintronics, interface, perpendicular magnetic anisotropy, magnetic domain wall,

spin-orbit torque, irradiation

Résumé

Les mémoires MRAM (Magnetic Random Access Memory) sont l'une des technologies émergentes visant à devenir un dispositif de mémoire «universelle» applicable à une grande variété d'applications. La combinaison du couple de spin-orbite (SOT) résultant de l'effet Hall de spin (SHE) et de l'interaction de Dzyaloshinskii – Moriya (DMI) aux interfaces entre un métal lourd et une couche ferromagnétiques s'est révélée être un mécanisme efficace pour induire une propagation de parois magnétiques chirales à des faibles densité de courant. Les dispositifs à parois magnétiques devraient constituer la prochaine génération de supports d'information en raison de leur potentiel pour des densités de stockage très elevées.. Cependant, une limitation cruciale est la présence de défauts structuraux qui piègent les parois magnétiques et induisent des courants de seuil élevés ainsi que des effets stochastiques importants. L'origine du piégeage résulte de la présence de défauts structuraux aux interfaces entre la couche magnétique ultra-mince et les autres couches (isolants et/ou métaux lourds) qui induisent une distribution spatiale des propriétés magnétiques comme l'anisotropie magnétique perpendiculaire (PMA) ou le DMI. Comprendre l'influence de la structure des interfaces sur la propagation de parois et sur le DMI en particulier est cruciale pour la conception de futurs dispositifs basse consommation.

C'est dans ce contexte très novateur que mon doctorat s'est focalisé sur la manipulation de la structure des interfaces dans des couches ultra-minces à anisotropie magnétique perpendiculaire. Des structures de CoFeB-MgO ont été utilisées afin de mieux comprendre l'impact de la structure des interfaces sur l'anisotropie, le DMI, la propagation de parois et les phénomènes de SOT. L'approche innovante que nous avons utilisée est basée sur l'irradiation par des ions légers pour contrôler le degré de mélange aux interfaces. Sous l'effet du mélange induit par l'irradiation, nous avons observé dans des structures de W-CoFeB-MgO une forte augmentation de la vitesse de parois dans le régime de creep, compatible avec une réduction de la densité des centres de piegeage. Nous avons aussi démontré que l'anisotropie de l'interface K_i et le DMI mesuré par propagation assymmétrique de parois se comportent de la même façon en fonction du mélange aux interfaces.

Finalement, nous avons fabriqué des barres de Hall afin de mesurer la commutation de l'aimantation induite par SOT. Le centre des croix de Hall a été irradié afin de diminuer localement l'anisotropie. Nous avons observé une réduction de 60% de la densité de courant critique après l'irradiation correspondant au retournement des croix de Hall irradiés par

propagation de parois. Notre étude fournit de nouvelles pistes concernant le développement de mémoires magnétiques à faible consommation, de dispositifs logiques et neuromorphiques.

Mots clés: Spintronics, interfaces, anisotropie magnétique perpendiculaire, parois magnétiques, couple de spinorbite, irradiation

General Introduction

Spintronics, refers to the study of the electron spin in materials and devices that exploit the spin properties instead of (or in addition to) the charge degree of freedom. The development of spintronic technology together with other emerging technologies has brought the semiconductor industry to a “Beyond Moore” era. The study of the spin-dependent electron transport phenomena in ferromagnetic materials led to the discovery of the giant magnetoresistance (GMR) effect in the mid-80s, attributed to Peter Grünberg and Albert Fert who both received the Nobel Prize in physics in 2007, and the discovery of GMR is considered as the birth of spintronics. Due to its large magnetoresistance variation, GMR effect has successfully been integrated into read heads in hard-disk drives (HDDs) technology. The implementation of GMR in HDDs was followed by the discovery of CoFeB-MgO based magnetic tunnel junctions (MTJs) with tunnel magnetoresistance (TMR) ratio as high as 604%. This has led to the development of Magnetic Random-Access Memory (MRAM), a promising candidate for a universal memory, owing to its non-volatility, high switching speed, infinite endurance and ultimate density.

During the last decades, several generations of MRAM have been proposed depending on the writing schemes, including toggle MRAM controlled by a magnetic field, spin-transfer torque (STT) MRAMs that are currently on the market for embedded memory applications and the latest generation of spin-orbit torque (SOT) MRAMs that are the most promising in terms of low current density and high speed.

The typical structure for devices based on SOT switching is composed of a ferromagnetic layer (FM) in contact with a heavy metal layer (HM) and an oxide layer. In these structures, the interface effect becomes pre-dominant since the thickness of the layers is of the order or less than one nanometer. In this case, the magnetic anisotropy coming from the FM / Oxide and HM / FM interfaces favors an axis of easy magnetization perpendicular to the plane (PMA, perpendicular magnetic anisotropy). Another phenomenon that has drew great attention is the existence of an exchange coupling between the magnetic atoms and the atoms of the heavy metal, giving rise to the presence of the Dzyaloshinskii-Moriya interaction (DMI). This interaction is responsible for the existence of topological solitons such as chiral domain walls or skyrmions which can be moved very efficiently by SOT. On the other hand, the inhomogeneities at the interface induce a spatial distribution of the magnetic properties (PMA, DMI, ...), which can have an important influence on the processes of magnetization

reversal. A fundamental understanding of the interface structure on the magnetic properties is then a prerequisite to develop devices with high performances.

The main objective of this thesis is to study the modulation of spin-dependent interfacial effects and the efficient SOT switching. In order to modulate the structure of the interfaces, we have used in particular irradiation with light ions, which makes possible to control the structural properties of thin films at the atomic scale. We have used CoFeB-MgO thin films with PMA, which are the most promising materials for STT and SOT based devices.

The thesis is divided into five chapters as follows.

Chapter 1 is a presentation of the state-of-the-art of MRAM technology, as well as the basic principles for DW dynamics in films with PMA and a short description of interfacial effects in HM/FM/Oxide structures.

Chapter 2 presents the main experimental techniques used throughout this thesis for sample fabrication and characterization.

Chapter 3 is devoted to the study of influence of the interface structure on magnetic properties, like PMA and DMI. The influence of parameters related to the film growth process, post-annealing and ion-irradiation processes are thoroughly investigated.

Chapter 4 presents a SOT induced magnetic switching with ultra-low critical current in a perpendicularly magnetized structure. To provide a comprehensive understanding, spin Hall angle, DMI and DW dynamics are studied systematically.

Chapter 5 investigates the influence of interface intermixing induced by ion irradiation on SOT switching in devices based on Hall bar structures.

Finally, the thesis ends with a “Conclusions and Perspectives” in Chapter 6.

Chapter 1 Background and State-of-the-Art

This thesis aims at highlighting the influence of interfaces in ultra-thin magnetic films on PMA, DMI, DW motion and ultimately on magnetic switching induced by spin-orbit torque (SOT). The present chapter is devoted to providing a brief view of (i) MRAM technology, then introduces the mechanism of magnetization switching related to (ii) DW dynamics. Finally, the most important effects (iii) spin-dependent interfacial effects in HM/FM/Oxide structure are presented.

1.1 Magnetic Random-Access Memory (MRAM)

Memory is a key element in computer architecture, which can exert crucial influences on the speed, integration and power consumption of the device. Current computer systems are based on von Neumann architecture [1], as shown in Figure 1-1, including an arithmetic logical unit (ALU), a control unit, a memory unit, and an input/output unit. However, continuously scaling down the complementary metal oxide semiconductor (CMOS) technology node drives high power and interaction latency issues due to the increasing leakage currents [2] and large data traffic [3]. To overcome these power and latency issues, non-volatile computing memory devices have received much attention in academic and industrial research [4-6]. Among emerging non-volatile memories, MRAM has developed rapidly in the past few decades due to its fast speed, infinite endurance, and potential high density.

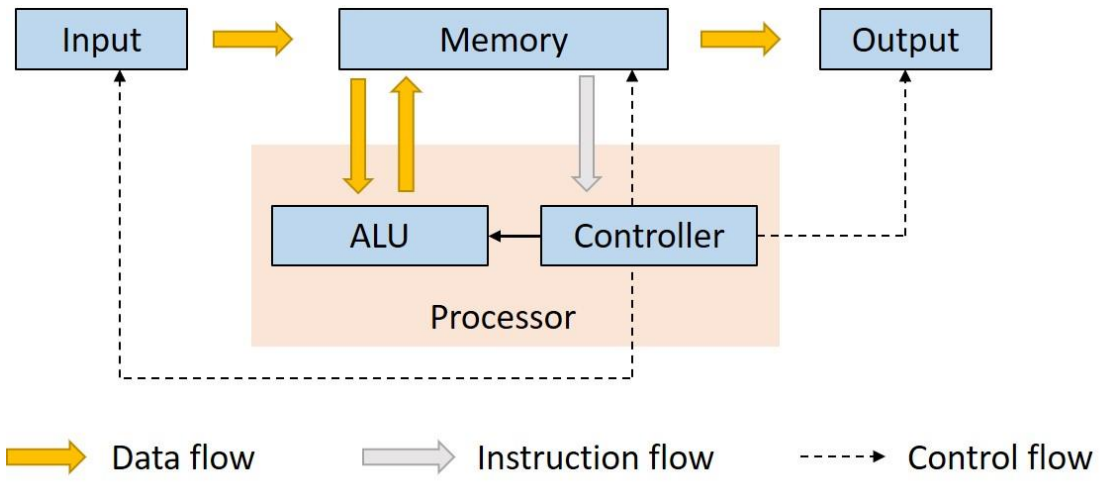

Figure 1-1. Configuration of von Neumann architecture.

In 1988, the discovery of giant magnetoresistance (GMR) in magnetic multilayers has highlighted a new path towards the design of spintronic devices based on manipulating both

the charge and spin of the electrons [7,8]. Afterwards, Tang *et al.* at IBM [9] proposed the spin-valve as reading element in HDD, which has increased the data storage density of HDD by more than 1,000 times in one decade[10,11]. In the mid-1990s, a new magnetic device, the magnetic tunnel junction (MTJ), began to emerge, which became the key element of an MRAM cell. MTJ, as a multi-layer structure, consists of two ferromagnetic electrodes separated by an ultra-thin oxide layer. The magnetization of one of the ferromagnetic layers is pinned, while the other one can be switched under an external excitation. We call the former one reference layer (RL) and the latter free layer (FL). The oxide insulating layer is a tunnel barrier (TB). When the magnetizations of RL and FL are parallel, the MTJ stays in the low resistance (R_P), whereas is the high resistance (R_{AP}), as shown in Figure 1-2. This corresponds to the binary system of "0" and "1".

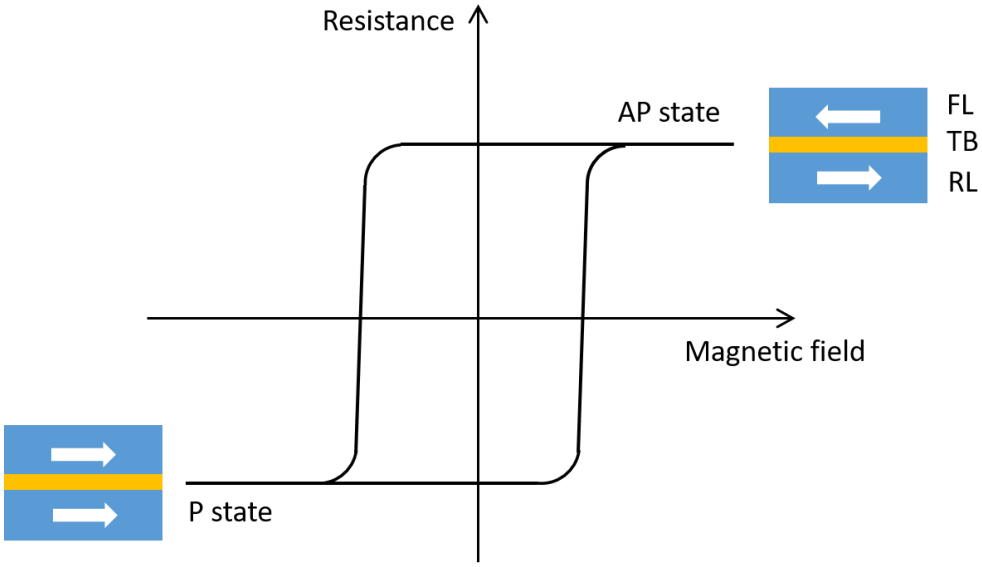

Figure 1-2. Schematic of the 2 states resistance depending on the relative magnetization directions of the RL and FL.

To measure the performance of MTJ, the tunnel magnetoresistance (TMR) ratio is defined as $\mathrm{TMR} = \frac{R_{AP}-R_P}{R_P}$. The higher the TMR ratio is, the higher the reading speed of the MTJ will be. In a ferromagnetic material, the distribution of the spin-up and spin-down electrons is asymmetric around the Fermi level, as shown in Figure 1-3[12]. It is called the spin-dependent tunneling and can be described by the spin polarization $\mathrm{P} = \frac{|n_\uparrow - n_\downarrow|}{n_\uparrow + n_\downarrow}$, where $n_\uparrow$ and $n_\downarrow$ are the density of electronic state of spin-up and spin-down near the Fermi level respectively. When the FL and RL stay parallel, the electrons in majority states in two layers have the same spin direction, resulting in a high tunneling probability, hence a high tunneling current and low resistance. When they stay antiparallel, high resistance appears [11,13].

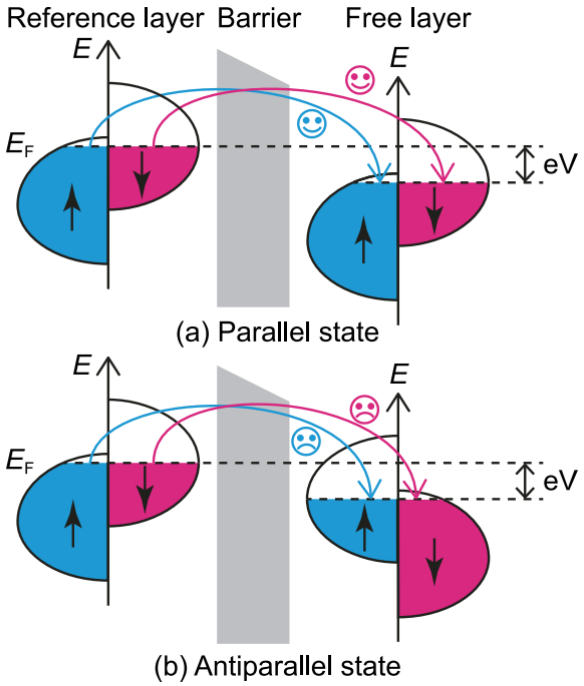

Figure 1-3. Principle of spin-dependent tunneling. Figure from Ref [12].

Researchers have put tremendous efforts into the pursuit of high TMR ratio. Al_2O_3 was firstly selected as the tunnel barrier [14,15], with typical TMR up to 18%. In 2002, first principles calculation predicted that the TMR can be as high as 1000% by replacing Al_2O_3 with monocrystalline MgO, due to its high matching degree with Fe ferromagnetic layers. Two years later, Parkin *et al* [16] and Yuasa *et al* [17] obtained a TMR of 220% in sputtered CoFeB/MgO/CoFeB multi-layers. Up to now, the highest TMR based on the MgO tunnel barrier is 604%, realized in a CoFeB/MgO/CoFeB pseudo-spin-valve [18].

Thanks to a high TMR utilizing MgO tunnel barrier, MTJ-based MRAM has flourished since the last decade. So far, MRAM technology has gone through three generations depending on their writing schemes: magnetic field driven MRAM, STT driven MRAM and SOT driven MRAM, as illustrated in Figure 1-4.

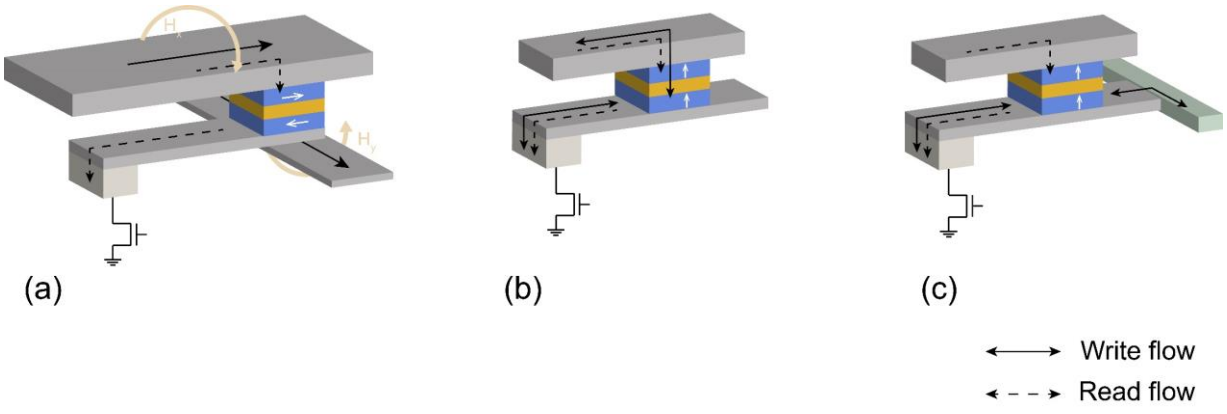

Figure 1-4. Schematic diagrams of (a) field switching MRAM cell, (b) STT-MRAM cell and (c) SOT-MRAM cell. The white arrows in MTJs represent the direction of the magnetization in ferromagnetic layers. The black solid (dashed) lines with arrows represent the writing (reading) flows.

The first generation of MRAM uses magnetic field for the writing process, as shown in Figure 1-4(a). The in-plane MTJ is sandwiched in between a word line and a bit line, along the easy axis and hard axis of MTJ, respectively. The MTJ is selected to be written only if the word and bit lines corresponding to the junction are energized at the same time [19,20]. However, this technology has two main weaknesses, which limit its wide application. One is the high power consumption. A large current is required to generate the pulse of magnetic field during writing. Usually 7-10 mA/line is suitable for the required switching field [21]. The other is the narrow write margin. A small current cannot switch the magnetization while a relatively large current may cause the misoperation of other MTJs, namely the half-selectivity disturbance. Although this problem was solved by Toggle MRAM [22], the magnetic field switching MRAM has been left out due to its high power consumption and low integration.

1.1.1 Spin-transfer torque (STT)-MRAM

Thanks to the discovery of the spin transfer torque (STT) effect[23,24], a new generation of MRAM has been proposed and so far has attracted significant attention in research and development (R&D). As shown in Figure 1-4(b), a typical memory cell includes an MTJ and a transistor (1MTJ 1T). The basic operation principle of STT-MRAM is presented in Figure 1-5. When a current flows from the reference layer to the free layer (as seen in Figure 1-5 (a)), it is polarized and has the same spin angular momentum as the RL. The transverse component of the moment exerted on the magnetization of FL is like a torque, which is considered as spin transfer torque. This torque manipulates the FL magnetization to lie parallel to the reference layer. Similarly, current in the opposite direction flows from FL to RL, electrons with opposite spin direction of RL are reflected into the FL, facilitating an anti-parallel state of the FL and RL, as shown in Figure 1-5(b).

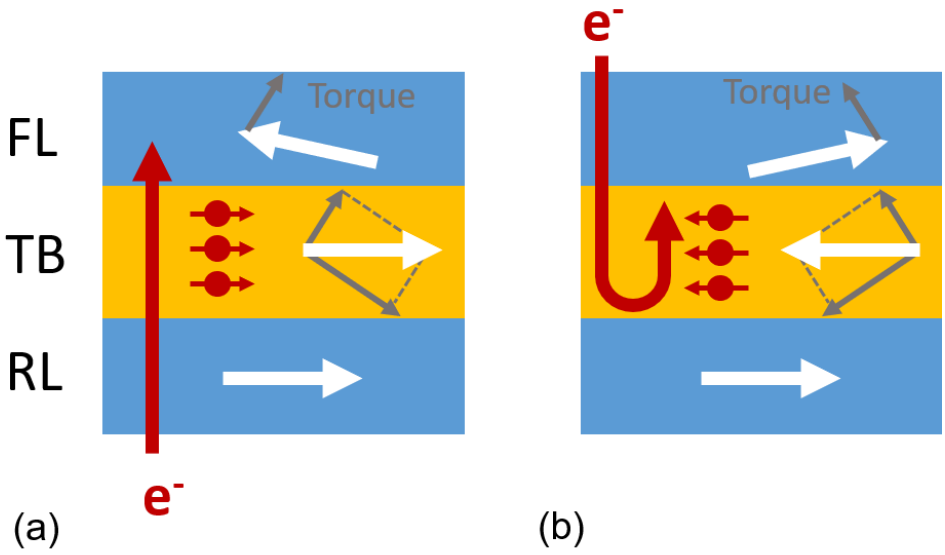

Figure 1-5. Illustrations of the basic operation principle of STT-MRAM. Write operation of the (a) parallel state (low resistance) and (b) anti-parallel state (high resistance).

The magnetization dynamics of the free layer resulting from the spin transfer torque can be expressed through the Landau-Lifshitz-Gilbert (LLG) equation by Macrospin approximation [25,26]:

$$\frac{\partial \boldsymbol{m}}{\partial t} = -\gamma\mu_0 \boldsymbol{m} \times \boldsymbol{H}_{eff} + \alpha \boldsymbol{m} \times \frac{\partial \boldsymbol{m}}{\partial t} - \frac{\gamma\hbar JP}{2et_F M_s} \boldsymbol{m} \times (\boldsymbol{m} \times \boldsymbol{m_r}) \quad (1.1)$$

where $\boldsymbol{m}$ and $\boldsymbol{m_r}$ are the unit magnetization of FL and RL, respectively; γ is the gyromagnetic ratio; μ_0 is the permeability; $\boldsymbol{H}_{eff}$ is the effective field including the extra field, demagnetized field and anisotropy field; α is the Gilbert damping constant; $\hbar$ is the reduced Planck constant; J is the writing current density; P is the spin polarization; e is the electron charge; t_F is the thickness of FL and M_s is the saturated magnetization of FL. Three terms on the right side of the equation represent the effective field torque, Gilbert damping torque and spin transfer torque, respectively. The first torque induces precession of the magnetization vector around the effective magnetic field, while the damping torque and the collinear spin transfer torque compete with each other, as shown in Figure 1-6. As long as the current is larger than the threshold value, the transfer torque can circumvent the damping torque and induce a magnetization switching.

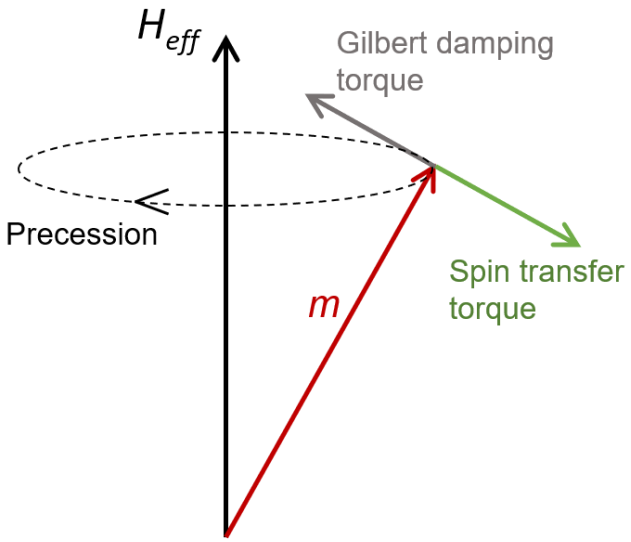

Figure 1-6. The magnetization dynamics under the effective field torque, Gilbert damping torque and spin transfer torque.

Compared to the first generation of MRAM using a magnetic field, STT-MRAM has been a significant discovery since it highlights a path towards the manipulation of magnetization with much less power and in a much more local way [27]. Thus, STT-MRAM has led to a booming interest in the semiconductor industry during the last decade. In 2005, the first STT-MRAM chip using 65 nm node came out under the common efforts of Renesas Technology and Grandis Inc. [28]. In the same year, Sony Corporation of Japan released a 4 kbit STT-MRAM based on a 1MTJ 1T structure [29]. The magnetization of MTJ lied in the sample plane, with an oval shape of 100×150 nm^2, TMR of 160% and a critical switching current J_c of 2.5×10^6 A/cm^2. In 2007, Hitachi and Tohoku university launched a STT-MRAM test chip with a storage capacity of 2 Mb. In this chip, not only the storage capacity has been greatly improved, the performance in terms of power consumption and reliability has also been enhanced. The unit writing energy consumption was only 1-2 pJ [30]. Three years later, Tohoku university successfully developed a magnetic tunnel junction with perpendicular magnetic anisotropy (PMA), expanding the device process node to sub-20 nm [31]. In 2016, a perpendicular MTJ with 11 nm diameter STT-MRAM [32] was co-demonstrated by IBM and Samsung, with an error rate of 7×10^{-10} at a write current pulse of 7.5 μA, 10 ns. In the International Solid-State Circuits Conference (ISSCC) 2019, Intel announced that they were ready to ship the batch production of STT-MRAM with 22 nm FinFET process [33].

Despite this rising interest in the STT-MRAM, there are still some technical bottlenecks. From Figure 1-4(b), we can see that both the write and read currents flow through the MTJ, which will result in the aging of the MgO tunnel barrier, hence reduce the endurance and

reliability of the device [34]. Moreover, continuously scaling down of process node (< 45 nm) can reduce the gap between the write and read currents, inducing undesirable writing when reading [35].

1.1.2 Spin-orbit torque (SOT)-MRAM

Recently, SOT switching magnetization has been proposed and attracted considerable attention [36,37]. This approach has practical implications for designing domain-wall based memories or for three-terminal magnetic tunnel junction bits with the lateral writing current decoupled from the perpendicular readout current.

The basic structure of SOT-MRAM is a nonmagnetic heavy-metal stripe in contact with the free layer of MTJ. Because of the spin orbit coupling (SOC) in the heavy metal, a transverse current through the heavy metal stripe leads to a torque at the HM/FM interface, inducing the magnetization reversal. This spin orbit torque may arise from the Rashba effect [36,38,39] and/or the spin Hall effect (SHE) [40-42], where the underlying physics is still under debate.

On the one side, Miron *et al.* considered that the Rashba interaction plays a key role in the reverse mechanism, which is induced by the asymmetric non-magnetic heavy metal and magnetic metal interface. When the current is injected in the plane of the HM, electrons experience an effective magnetic field

$$\boldsymbol{H_R} = \alpha_R \boldsymbol{z} \times \boldsymbol{J_c} \tag{1.2}$$

where α_R is the Rashba constant, $\boldsymbol{z}$ is a unit vector perpendicular to the film plane (the z direction) and $\boldsymbol{J_c}$ is the vector current density, as shown in Figure 1-7(a).

On the other side, Liu *et al.* hold that the spin accumulation induced by SHE is the intrinsic mechanism of the magnetization switching. In practical terms, when a current $\boldsymbol{J_c}$ flows through the heavy metal, where the SOC is strong, the electrons of spin up and spin down will accumulate at the upper (or lower) and lower (or upper, depending on the spin Hall angle Θ_{SHE} of the materials) interface, leading to a pure spin current $\boldsymbol{J_s}$ along *z* axis:

$$\boldsymbol{J_s} = \Theta_{SHE} \sigma \times \boldsymbol{J_c} \tag{1.3}$$

where σ is the unit vector of the electron spin.

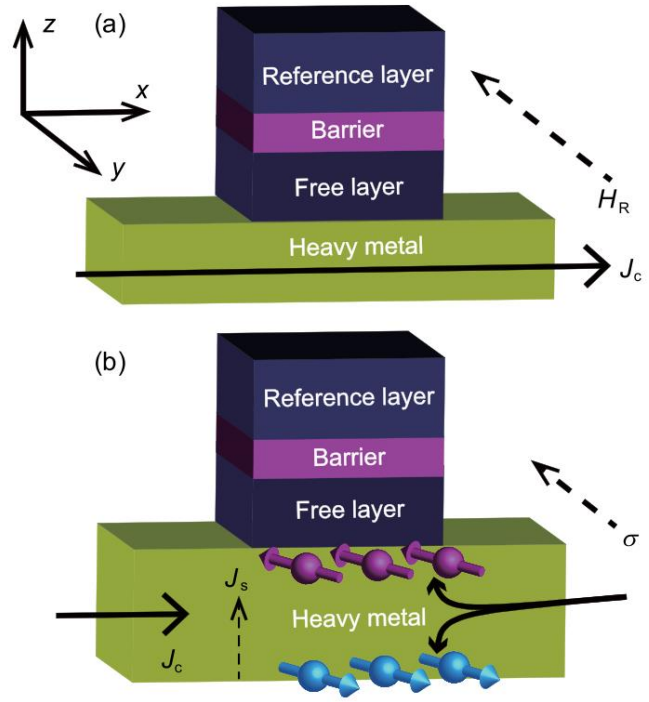

Figure 1-7. Three-terminal MTJ switched by spin orbit torque. (a) Induced by Rashba effect; (b) induced by Spin Hall effect. Figure from Ref [12].

Despite the origin of the SOT, it can be quantified as an antidamping-like torque ($\boldsymbol{\tau_{DL}}$ or $\boldsymbol{\tau_{\parallel}}$) and field-like torque ($\boldsymbol{\tau_{FL}}$ or $\boldsymbol{\tau_{\perp}}$)[43-46]:

$$\boldsymbol{\tau_{DL}}\ (\boldsymbol{\tau_{\parallel}}) \sim \boldsymbol{m} \times (\boldsymbol{y} \times \boldsymbol{m}) \tag{1.4}$$

$$\boldsymbol{\tau_{FL}}\ (\boldsymbol{\tau_{\perp}}) \sim \boldsymbol{m} \times \boldsymbol{y} \tag{1.5}$$

where $\boldsymbol{m}$ is the magnetization vector, $\boldsymbol{y}$ is the electron polarization direction vector of spin polarized current arising from SOC. Figure 1-8 presents the directions and amplitudes of $\boldsymbol{\tau_{\perp}}$ and $\boldsymbol{\tau_{\parallel}}$ corresponding to different directions of magnetization. In particular, the effective magnetic fields produced by the two torques, $\boldsymbol{B_{\perp}}$ and $\boldsymbol{B_{\parallel}}$ are shown in Figure 1-8.

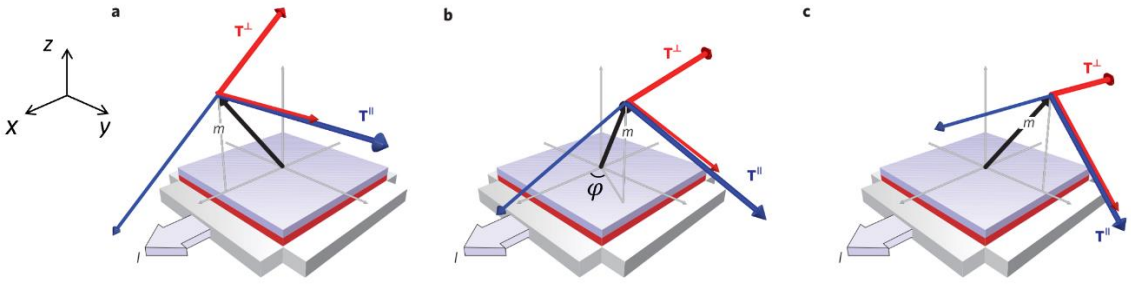

Figure 1-8. Torque schematics and magnetization measurements. The thick arrows indicate the direction and amplitude of $\boldsymbol{\tau_{\perp}}$ (red) and $\boldsymbol{\tau_{\parallel}}$ (blue) for (a) $\boldsymbol{\varphi = 0°}$, (b) $\boldsymbol{\varphi = 60°}$, and (c) $\boldsymbol{\varphi = 90°}$. The thin arrows indicate the equivalent effective fields $\boldsymbol{B_{\perp}}$ (red) and $\boldsymbol{B_{\parallel}}$ (blue). Figure from Ref [43]

The working principle of SOT on magnetization reversal can be also well depicted by

Landau-Lifshitz-Gilbert (LLG) equation with two torque terms [47] added:

$$\frac{\partial \boldsymbol{m}}{\partial t} = -\gamma\mu_0 \boldsymbol{m} \times \boldsymbol{H}_{eff} + \alpha \boldsymbol{m} \times \frac{\partial \boldsymbol{m}}{\partial t} + \gamma\mu_0 H_{SOT}^{DL} \boldsymbol{m} \times (\boldsymbol{y} \times \boldsymbol{m}) + \gamma\mu_0 H_{SOT}^{FL} \boldsymbol{m} \times \boldsymbol{y} \tag{1.6}$$

where γ is the gyromagnetic ratio; μ_0 is the permeability; $\boldsymbol{H}_{eff}$ is the effective field and α is the Gilbert damping constant. H_{SOT}^{DL} and H_{SOT}^{FL} are the effective field induced by damping-like torque and field-like torque, depicted as

$$H_{SOT}^{DL} = \frac{J_{SOT}\theta_{SH}\hbar}{2et_F\mu_0 M_s} \tag{1.7}$$

$$H_{SOT}^{FL} = \eta H_{SOT}^{DL} \tag{1.8}$$

where θ_{SH} is the HM spin Hall angle, $\hbar$ is the reduced Planck constant, t_F is the thickness of the adjacent FM layer, J_{SOT} is the SOT current density, and η is the ratio between the strength of these two torques.

The threshold SOT current density J_{th} derived from a quasi-static approximation is as follows [48]:

$$J_{th} = \frac{2et_F M_s}{\hbar\theta_{SH}} \left(\frac{H_{K,eff}}{2} - \frac{H_x}{\sqrt{2}}\right) \tag{1.9}$$

where $H_{K,eff}$ and H_x represent the effective anisotropy field and in-plane field, respectively. It is worth noting that this formula is rather accurate with only DLT considered. However, despite that, to gain a low threshold current density, large spin Hall angle, thin FM layer and relatively low saturated magnetization are indispensable, which can be achieved by materials choices and interface manipulation.

The main challenge for SOT memory device is the requirement of an external magnetic field. From the schematic diagram of the SOT, only 90° switching can be realized with SOT. After SOT current is removed, the magnetization will randomly process to +z or -z direction because of thermal disturbance. Therefore, the injected SOT current itself cannot play a decisive role in switching for the perpendicular magnetization. An in-plane magnetic field along *x* axis is necessary to break the mirror symmetry and determine the switching direction [38,40]. However, the external magnetic field not only increases the complexity of the device design, but also increases the power consumption and reduces its reliability. This limits the development of SOT-MRAM. Therefore, how to use the spin orbit torque to directly reverse the perpendicular magnetization without external magnetic field has become one of the hottest issues. Currently, various methods have been proposed in order to realize the field-free switching. Some researchers employed the anti-ferromagnetic metal to replace the non-magnetic metal to provide SOT. The anti-ferromagnetic metal induces an exchange bias

along the writing current, equivalent to an external magnetic field [49,50]. In addition, ingenious device geometry can also help realize the field-free switching [51]. The displacement of the DWs observed in magnetic wires with different shapes and orientations is found to be highly dependent on the angle between the direction of the current and domain wall motion. Another approach consists in manipulating the structure of the interface. For example, different degrees of oxidation at the CoFeB/TaO_x interface induce a torque along *z* axis, hence allowing the switching of the perpendicular magnetization without external field [52]. The ability of controlling the magnetization switching by manipulating the device geometry and film interface provides much of the early motivation for this thesis.

1.2 Domain wall dynamics

Magnetic domain is a basic phenomenon in magnetism. The investigation of domain wall dynamics is of importance for understanding magnetization switching. Meanwhile, the region between two uniformly magnetized domains, i.e magnetic DW, is the essence of the racetrack memory [53], which was proposed by IBM in 2008. Figure 1-9 shows the concept of racetrack memory device, where a nanostrip is divided into magnetic domains separated by DWs (Figure 1-9 (c)). In such application, the up (blue) and down (red) domain represent the logic bit “0” and “1”. As an example, after 4 current pulses are injected into the nanowire, the pattern is shifted from 4 positions to the right. Domains can be moved back and forth depending on the polarity of the current flowing through the wire, as well as the spin Hall angle of the magnetic materials [54]. In this case, all DWs obtain the same speed due to Zhang-Li torque [55], leading to the same domain width and negligible readout errors. This concept is only valid under current pulses, while the external magnetic field will force the domains to align in the direction of the field and all the information will be erased.

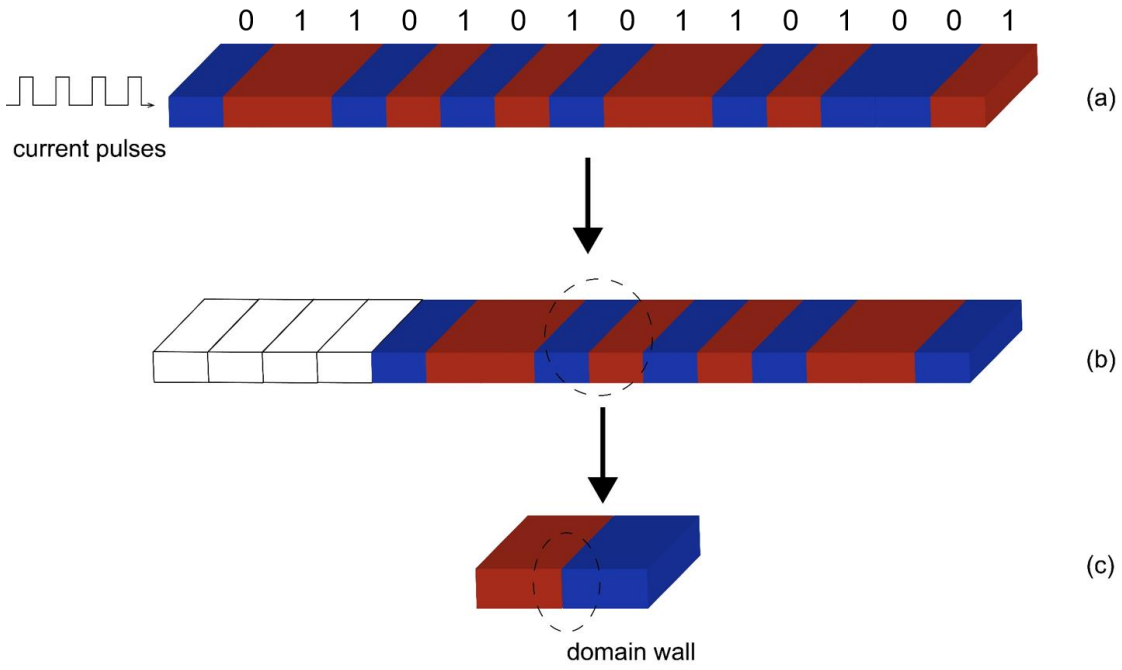

Figure 1-9: Schematic of a racetrack memory device, representing a nanostrip divided into domains separated by DWs. The domains represent the logic bits "0" (blue) and "1" (red). (a) Initial states of the memory device. (b) After 4 current pulses, the whole bit pattern shifts 4 positions to the right. (c) Domain wall between two domains.

1.2.1 Field-driven DW motion

Understanding the dynamics of an elastic interface in presence of random disorder is a key issue in many physical systems. This is the case for a magnetic DW in a thin ferromagnetic layer with PMA driven by a magnetic field. It has been shown from theory [56-59] and experiment [60-62] that 3 dynamical regimes of DW velocity versus magnetic field are presented, as shown in Figure 1-10. At low applied fields, pinning due to structural defects dominates the DW dynamics, leading to a glass-like motion, which is the so-called creep regime described by universal power laws. In this region, pinning tends to stabilize DW positions [61], induce DW roughness, and introduce stochasticity [63]. At sufficiently high magnetic fields, the DW propagates in the so-called flow regime where the velocity is proportional to the applied field and is limited only by intrinsic dissipation or friction-like force [64], i.e. the Gilbert damping parameter [65]. The region between the creep and flow regime is the intermediate depinning regime.

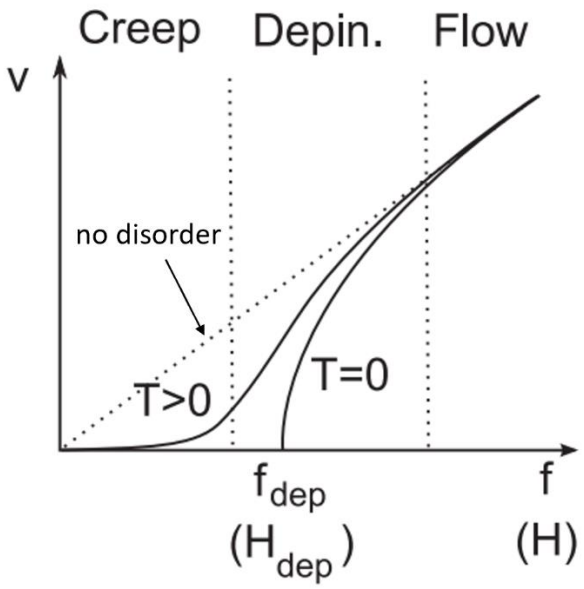

Figure 1-10. Theoretical velocity as a function of driving force at finite temperature (T > 0) and at T= 0. The creep, depinning, and flow regimes are labeled. In a "perfect" medium with no disorder, the velocity is proportional to the driving force (dashed line). Image from Ref.[66].

In the thermally activated creep regime ($f \ll f_{dep}$, finite T), the velocity of the DW motion follows the creep law [60,67]:

$$v = v(H_{dep},\ T)\exp[-(\frac{U_c}{k_B T})(\frac{H_{dep}}{H})^{\mu}] \tag{1.10}$$

where $v(H_{dep},\ T)$ is a constant related to the depinning field H_{dep} at 0 K and the temperature, U_C is the scaling energy constant, k_B is the Boltzmann constant, T is the temperature, H is the external applied field, and μ is the critical exponent. For a 1D DW propagating in a weak pinning disordered medium, μ=1/4 is in good agreement with the experiment data [57]. Since pinning dependent motion of elastic interfaces is observed in a large variety of other systems [68] such as ferroelectric materials [69], contact lines in wetting [70], crack propagation [71], and earthquake models [72]., V. Jeudy *et al.* has proposed a unique universal function in terms of pinning energy barrier to describe the creep law [68]:

$$v = v(H_{dep},\ T)\exp\left[-\frac{\Delta E}{k_B T}\right] \tag{1.11}$$

with

$$\Delta E = U_C[\left(\frac{H_{dep}}{H}\right)^{\mu} - 1]. \tag{1.12}$$

For $H \to 0$, $\Delta E \to U_C\left(\frac{H_{dep}}{H_{ex}}\right)^{\mu}$ and v is in accordance with that described in Eq. (1.10). For $H \to H_{dep}$, there is a linear vanishing of the energy barrier ($\Delta E \to 0$), which indicates the upper boundary of the creep regime: H_{dep}. According to Eq. (1.11-1.12), a linear relationship can be found between $\ln(v)$ and $H^{-1/4}$. As an example in Figure 1-11, it can be

observed that the measured data for different films with PMA are in good agreement with the prediction of Eq. (1.10).

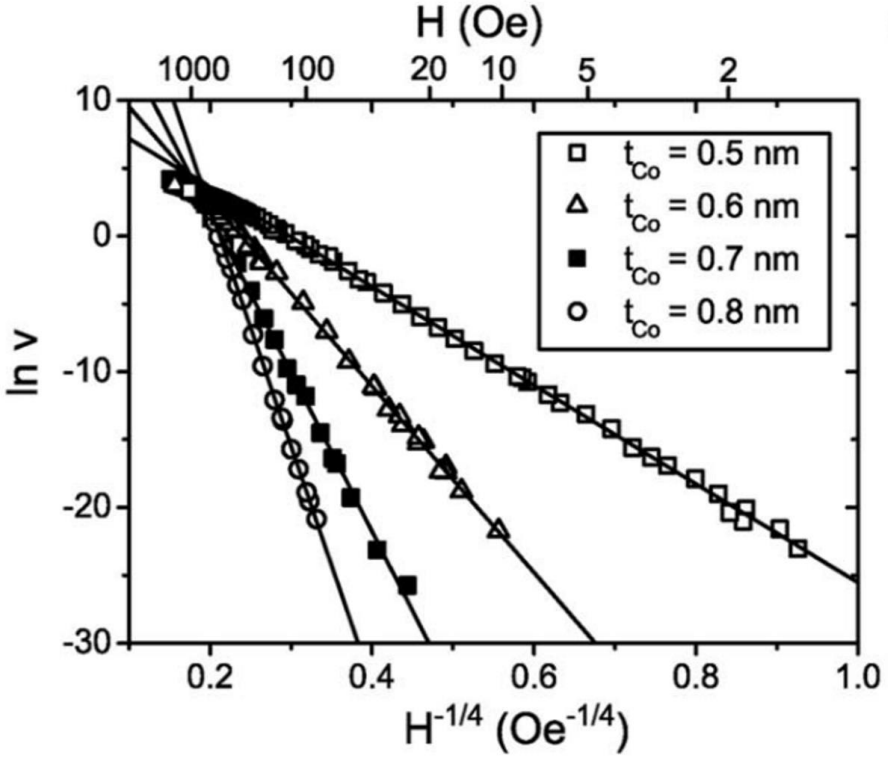

Figure 1-11. Natural logarithm of the DW velocity for Pt/Co/Pt films with four different Co thicknesses plotted against $H^{-1/4}$ that agrees with the creep theory prediction in Eq. (1.13). Image from Ref [66].

It is found that H_{dep} is also very important since it strongly depends on the structural disorder of the magnetic films such as interface intermixing, interface roughness or grain boundaries [73]. R. Diaz Pardo and V. Jeudy *et al.* provided a fitting procedure to extract H_{dep}[74]. In detail, the variation with temperature of the velocity at the threshold ($H = H_{dep}$) can be written as:

$$v\left(H_{dep}, \mathrm{T}\right) = v_T \left(\frac{T}{T_{dep}}\right)^{\Psi} \tag{1.13}$$

while the variation with magnetic field at zero temperature ($T \ll T_{dep}$) is

$$v\left(H, T \ll T_{dep}\right) = v_H \left(\frac{H - H_{dep}}{H_{dep}}\right)^{\beta} \tag{1.14}$$

where v_T and v_H are depinning velocities, T_{dep} is a characteristic temperature related to the pinning strength of the material, ψ and β are the critical exponents.

According to this method, the depinning field can be extracted by fitting Eq. (1.11-1.14). As an example shown in Figure 1-12, DW velocities in Pt/Co/Pt for different temperatures are measured. By fitting the universal creep law in Eq. (1.11) and the depinning law in Eq (1.13), depinning field could be extracted.

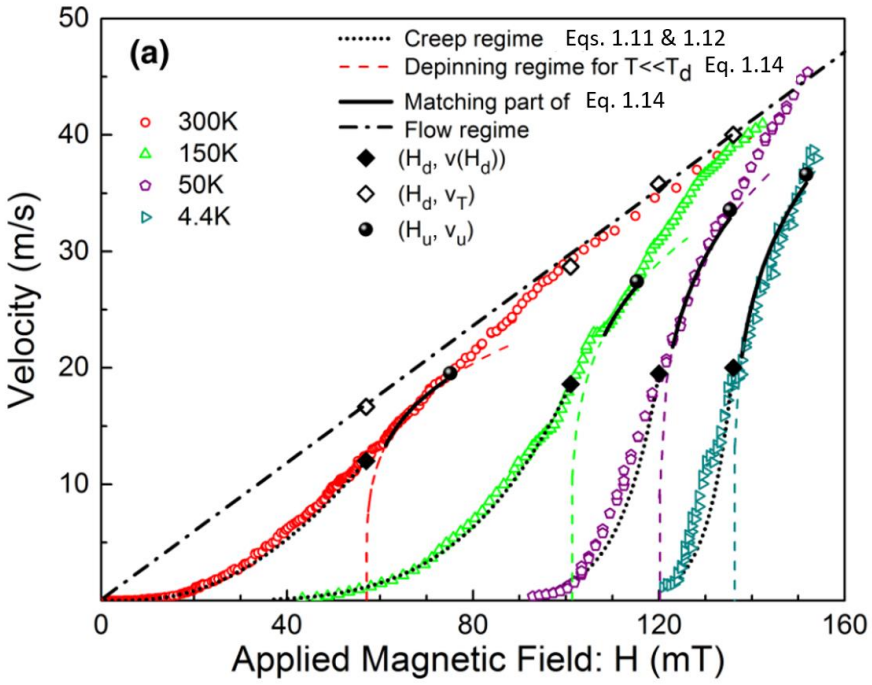

Figure 1-12. Domain-wall velocity in Pt/Co/Pt measured for different temperatures to show the high and low drive regimes. The creep regime [0 <H <$H_{dep}(T)$] is highlighted by the black dotted curves corresponding to fits of Eq. (1.14) with μ = 1/4 and ends for velocities v ($H_{dep}(T)$, T) indicated by black diamond symbols. The depinning regime extends from the depinning threshold $H = H_{dep}(T)$ to the universality limit $H_u(T)$ (indicated by black solid spheres). The depinning velocities v_T ($H_{dep}(T)$,T) deduced from with part of all velocity curves as indicated by black solid segments. The linear flow regime, indicated by a straight dashed-dotted line, is Eq. (1.16) correspond to empty diamonds. Image from Ref. [74] .

Since DW dynamics is sensitive to the structure inhomogeneous, it has been studied by introducing interface disorder. For instance, Herrera Diez *et al.* found that a significant decrease in DW velocity in creep regime was induced by ion irradiation in Ta/CoFeB/MgO thin films with PMA[73]. This could be explained by the interface disorder induced by irradiation, which leads to a reduction of effective magnetic anisotropy and an extension of creep region of DW motion (corresponding to an increase of H_{dep}). Later on, this group presented that the DW velocity was increased upon irradiation on the contrary in higher field region, namely the flow region, in the same film system [75]. This is an interesting result because it seems to withstand the common perception that the flow area is not sensitive to disorders. Authors explained this from the aspect of the intrinsic parameters, which are strongly influenced by interface disorder. These studies clearly show that understanding the role of interface disorder is crucial for the design of future low power devices based on chiral DW motion.

1.2.2 Spin orbit torque driven DW motion

Successful control of DW motion under current is a necessary step toward the realization and scalability of DW devices such as the race track memory concept [53]. The current-induced domain wall motion (CIDWM) in ferromagnetic nanowires has been intensively investigated since its first demonstration [23,24]. For a long period, CIDWM has been considered to be driven by STT, including the adiabatic and nonadiabatic STTs [76,77]. However, it cannot explain the direction of DW motion against the electron flow in Pt/Co/oxide structures [78-80]. In such structure with perpendicular magnetic anisotropy, the SOT induced by SHE and/or Rashba effect at the HM/FM interface have been proposed as a possible origin of CIDWM. The structure with PMA normally facilitates Bloch type DWs due to the existence of demagnetizing field, as shown in Figure 1-13 (a). In this scenario, the magnetization in the DW is collinear with the electron polarization direction $\boldsymbol{y}$, making both $\boldsymbol{\tau_{DL}}$ and $\boldsymbol{\tau_{DL}}$ equal to zero. Hence, pure SOT current is incapable for driving DWs [81-83], while an in-plane field is necessary. By applying such in-plane field, the magnetization in the DW is partially titled along $\boldsymbol{x}$ direction, according to what the nonzero SOT can act on the magnetization. However, as mentioned before, this external field must be removed from an application perspective.

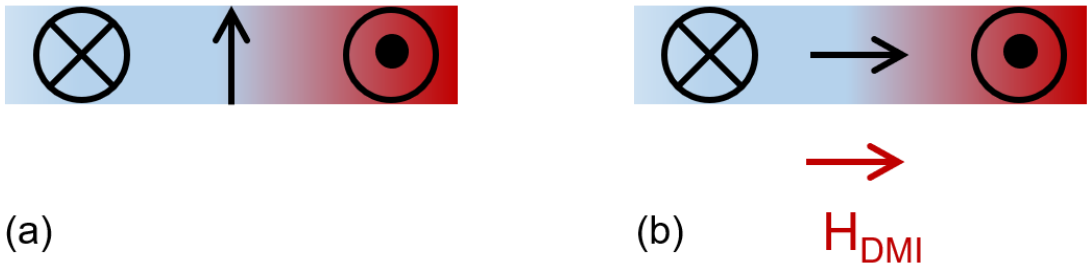

Figure 1-13. The top view of the Bloch type (a) and Néel type (b) DWs in a perpendicularly magnetized structure. The blue and red regions represent the down and up domains, respectively.

Later studies have shown that the effective DMI field has the capability of promoting and stabilizing the Néel type DWs [44,84,85], which can be competent to drive the SOT induced DW motion. In this case, the magnetization in the DW aligns transversely with $\boldsymbol{y}$ direction, as shown in Figure 1-13(b). The combination of SHE, which produces current-induced torque, and the DMI, which stabilizes chiral DWs, induces uniform motion of Chiral DWs with rather high efficiency. The current generates an effective field associated by a Slonczewski-like torque [40,81], written as:

$$\boldsymbol{H_{SL}} = H_{SL} \cdot (\boldsymbol{m} \times (\boldsymbol{z} \times \boldsymbol{j_e})) \tag{1.15}$$

where H_{SL} is the effective torque field, $\boldsymbol{m}$, $\boldsymbol{z}$ and $\boldsymbol{j_e}$ are unit vectors along the magnetization, z axis and electron flow, respectively [86]. In 2013, Beach *et al.* first

experimentally confirmed the highly efficient DW motion induced by sole SOT in Pt/Co system [44]. Figure 1-14 presents this left handed Néel DWs with oppositely internal magnetization for up–down and down–up transitions. The effective field $\boldsymbol{H_{SL}}$ that moves the two DWs in the same direction against the electron flow is evidenced due to the sign of the Spin Hall angle.

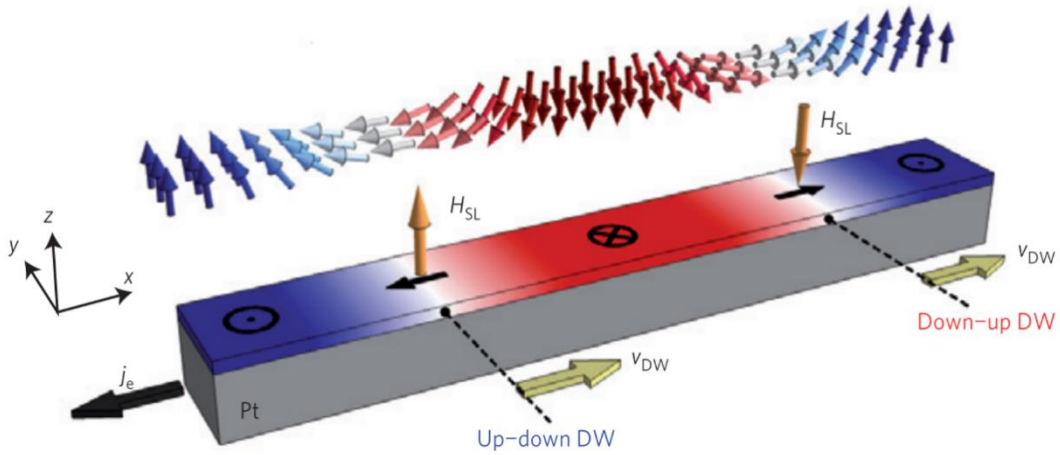

Figure 1-14. Illustration of left-handed chiral Néel DWs. H_{SL} moves adjacent up–down and down–up domains with velocity v_{DW} in the same direction against electron flow j_e. Image from Ref [44].

Magnetic skyrmion is another promising spin component, which can be regarded as a superposition of two bending DWs, hence can also be efficiently driven by SOT [87]. It is considered to be more promising than chiral DWs as new information carriers in racetrack memory, due to its smaller size and lower depinning current density. However, the small size of skyrmion, usually in the range of several nanometers to several micrometers, is comparable to the size of structure inhomogeneous, such as extrinsic defects and grain boundaries. This makes the understanding and minimizing interface disorder a crucial topic and also provides the early motivation for this thesis.

1.3 Spin-dependent Interfacial effects in HM/FM/Oxide structure

By continuously scaling down the technological nodes, interfacial effects become even more apparent and play significant roles in spintronics. For example, in the SOT induced magnetization switching, the thickness of the cobalt layer is chosen to be 0.6 nm to maximize both the PMA and the Rashba effect due to structure inversion asymmetry at the platinum and AlO_x interfaces [36]. In this thesis, we will highlight two interfacial effects: perpendicular magnetic anisotropy (PMA) and Dzyaloshinskii-Moriya interaction (DMI) in in HM-CoFeB-MgO ultra-thin films, which attract great interest in current research on SOT.

1.3.1 Perpendicular magnetic anisotropy in HM-CoFeB-MgO structures

In a ferromagnetic material, the magnetization will be easier or harder to magnetize in terms of the direction, which is considered as the magnetic anisotropy. For most magnetically anisotropic materials, there are two favorable directions of spontaneous magnetization, and the two directions are a 180° rotation apart. The line parallel to these directions is called the *easy axis*, along which the total energy of the material system will be the lowest. On the contrary, the direction that facilitates the highest energy is the so-called *hard axis*. The energy consumed to rotate the magnetization from the easy axis to hard axis is the magnetic anisotropy energy (MAE).

The primary origin of magnetic anisotropy is the magnetic dipolar interaction and spin-orbit coupling. The dipolar interaction is a long-range effect, whose contribution is dependent on the shape of the sample, hence it is usually called the shape anisotropy. The spin-orbit coupling between the electron spin and orbit momentum leads to the anisotropy along different crystallographic orientations. It is referred to as the magnetocrystalline anisotropy [88,89]. Besides, tension and/or stress could also lead to an anisotropy, which is called the magnetoelastic anisotropy.

Shape anisotropy

When a particle is not perfectly spherical, the demagnetizing field will not be equal for all the directions, creating one or more easy axes. Thus, the shape anisotropy could be characterized by the demagnetizing field, as

$$\boldsymbol{H_d} = -\boldsymbol{N} \cdot \boldsymbol{M} \tag{1.16}$$

where $\boldsymbol{N}$ is the demagnetizing factor, which has three components (N_x, N_y, N_z) in a three-dimensional object, and their relationship can be expressed as $N_x + N_y + N_z = 1$. For a thin film, the dimension of film thickness is much smaller than the film width and length. In this case, $N_z \to 1$, while N_x and $N_y \to 0$.

The shape anisotropy induced magnetic anisotropy energy could be expressed as[90]

$$E_d = -\frac{\mu_0}{2} \int \boldsymbol{M} \cdot \boldsymbol{H_d}\, dV \tag{1.17}$$

Considering the demagnetizing factor, the anisotropy energy density is

$$K_d = -2\pi M_s^2 \tag{1.18}$$

Magnetocrystalline anisotropy

The magnetocrystalline anisotropy of bulk materials with high symmetries such as Fe and Co is not as large as 10^{-6}-10^{-5} eV/atom. But in the ferromagnetic systems, in which the FM1/FM2 and FM/HM interface with large asymmetry, a large SOC and large magnetocrystalline

anisotropy are consequently exhibited. The magnetocrystalline anisotropy energy density in such heterostructure could be as high as 10^{-4}-10^{-3} eV/atom [91,92]. The magnetocrystalline anisotropy from the bulk and interface both contributes to the total anisotropy.

Magnetoelastic anisotropy

Magnetoelastic anisotropy usually comes from the stress induced lattice mismatch, in which the stress could be caused by the temperature gradient and non-uniform deposition process, etc. The anisotropy caused by this effect is small and negligible.

In the ferromagnetic thin film, the effective anisotropy energy density could be expressed as:

$$\begin{aligned} K_{eff} &= K_b + K_i/t_{FM} + K_d \\ &= K_b + K_i/t_{FM} - 2\pi M_s^2 \end{aligned} \tag{1.19}$$

Thus, the total anisotropy energy can be expressed as:

$$\begin{aligned} E_{ani} &= K_{eff} t_{FM} S \\ &= [(K_b - 2\pi M_s^2) t_{FM} + K_i]\mathrm{S} \end{aligned} \tag{1.20}$$

where *S* is the area of ferromagnetic film. From Eq. (1.20), we can see that the contributions from the bulk anisotropy K_b increase with the growth of the FM thickness, while the interfacial contribution is independent of the thickness.

In 1985, P.F. Carcia *et al.* obtained the first perpendicular magnetic anisotropy (PMA) in Co/Pd multilayer structure when the thickness of Co is less than 0.8 nm. They attributed this to Co/Pd interface anisotropy and the stress effect in Co film [93]. Later on, the HM/FM/Oxide structure has more widespread application prospect in MRAM since the oxide layer can be integrated in an MTJ with large TMR. In 2010, H. Ohno *et al.* observed the PMA in Ta/CoFeB/MgO layers when the thickness of CoFeB is less than 1.3 nm [31]. The effect anisotropy constant K_{eff} can be expressed as:

$$K_{eff} = K_b - \frac{\mu_0 M_s^2}{2} + \frac{K_i}{t_{CoFeB}} \tag{1.21}$$

where K_b is the bulk crystalline anisotropy and K_i is the interfacial anisotropy, $\frac{\mu_0 M_s^2}{2}$ is the demagnetization energy density and t_{CoFeB} is the thickness of ferromagnetic layer CoFeB. Figure 1-15 illustrates the linear fitting of $K_{eff} \cdot t_{CoFeB}$ as a function of t_{CoFeB}. The slope of the linear extrapolation is $K_b - \frac{\mu_0 M_s^2}{2}$, whose value is consistent with the calculated $-\frac{\mu_0 M_s^2}{2}$, indicating that K_b is negligible. Hence, the perpendicular anisotropy in this system is entirely due to the interfacial anisotropy.

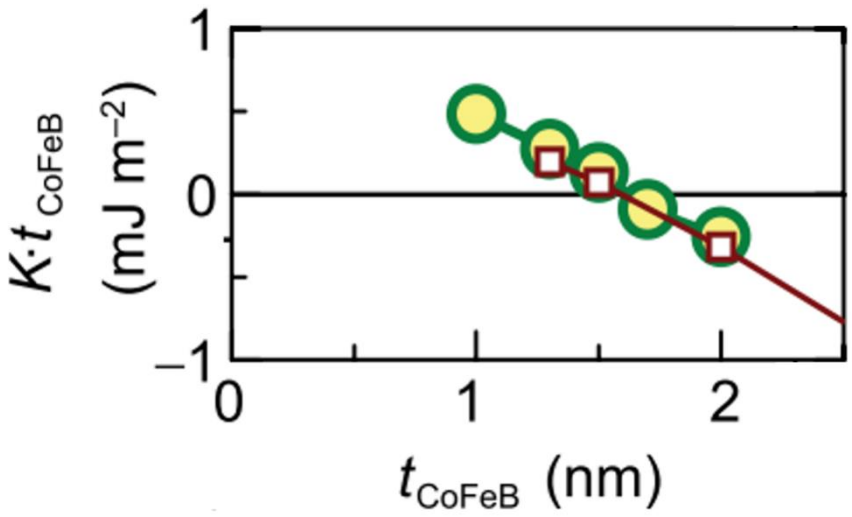

Figure 1-15. t_{CoFeB} **dependence of the product of** K_{eff} **and** t_{CoFeB}**, where the intercept to the vertical axis and the slope of the linear extrapolation of the data correspond to** K_i **and** $K_b - \frac{\mu_0 M_S^2}{2}$**. Circles and squares are obtained from magnetization and FMR measurements, respectively. Figure from Ref.** [31].

Later, theoretical evidence provided by the first-principles calculations shows that the O-p_z orbital around the Fermi level in MgO hybridized at the interface with the (d_{z^2}, $d_{xz(yz)}$) orbitals of the transition metal Co and Fe[94,95] is the main contribution to the interfacial PMA. Moreover, experiments have shown that another interface between FM and HM, also has huge impacts on PMA. In 2011, Worledge *et al.*[96] found that CoFeB/MgO bilayer deposited on Ta exhibits PMA after annealing while on Ru does not. First-principles calculations reveal that at HM/FM interface, the hybridization of the Co (Fe) (d_{xy}, $d_{x^2-y^2}$) orbitals and the (p_y, p_z) orbitals of the non-magnetic HM atoms also contribute to the PMA, and even generate stronger PMA than that at the CoFe/MgO interface [97,98]. The configuration of the invested structures is shown in Figure 1-16 (a-d), the layer-resolved magnetic anisotropy energy (MAE) is calculated and depicted in Figure 1-16 (e) and (f). Different elements lead to quite different MAEs, which can be explained with the variations of SOC and orbital hybridizations at the CoFe/HM interface.

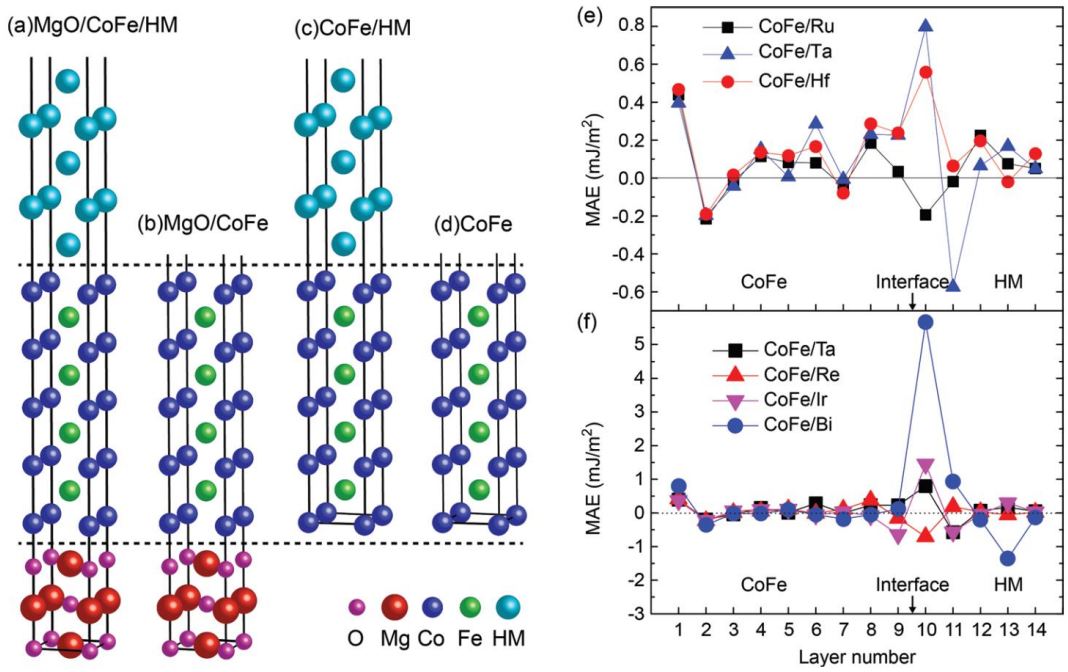

Figure 1-16. Schematics of atomic structures for a) MgO/CoFe/HM, b) MgO/CoFe, c) CoFe/HM, and d) CoFe thin films. e, f) Layer-resolved MAEs of different CoFe/HM structures. Nine CoFe monolayers (layer 1–9), five HM monolayers (layer 10–14), and a vacuum layer are included in the structures. Images from Ref [97,98].

Apart from the term of material choices to tune PMA, experiment methods are also proved to be effective for that. In widely studied Ta/CoFeB/MgO structure, PMA highly relies on the annealing temperature. It is enhanced with the increasing temperature at first, however, when the temperature exceeds a certain degree, usually 350℃ for Ta-based structure, the film cannot remain PMA. This phenomenon could be explained by the element diffusion to the adjacent layer [99-103]. Moreover, the oxidation conditions (i.e. overoxidation or underoxidation) [104] at MgO/HM interface, stoichiometry of Co and Fe [105,106] and irradiation induced interface disorder[73], also lead to a significant change in PMA. The influence of annealing and irradiation on PMA will be discussed in more detail combined with our experiment results.

1.3.2 Interfacial Dzyaloshinskii-Moriya Interaction (DMI)

The interfacial Dzyaloshinskii-Moriya interaction (DMI) has attracted considerable interest recently due to its potential to the generation of skyrmions[107,108], stabilization of chiral domain walls[44,109] and SOT induced switching[110]. Its main origins and applications are shown in Figure 1-17.

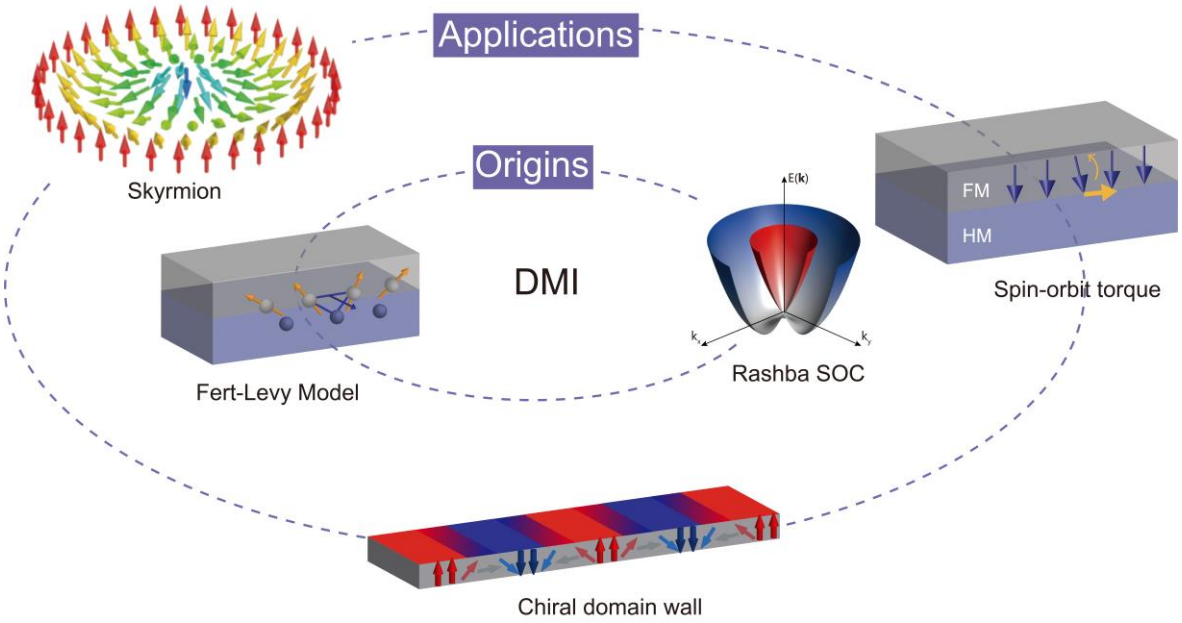

Figure 1-17. A schematic illustration of the Dzyaloshinskii-Moriya interaction origins of DMI at different interfaces (inner ellipse) and the related performance properties of spintronic devices (outer ellipse).

In magnetic materials, the adjacent spin sites $S_{i,j}$ tend to be parallel or antiparallel due to the Heisenberg exchange. The corresponding exchange energy can be written as [111]:

$$E_H = -\sum_{i,j} J_{ij} \boldsymbol{S_i} \cdot \boldsymbol{S_j} \tag{1.22}$$

where $\boldsymbol{S_i}$ and $\boldsymbol{S_j}$ are neighbouring spins and J_{ij} is the corresponding exchange constant. When it is positive, interaction corresponds to ferromagnetic exchange, while the negative sign represents the antiferromagnetic exchange. In both cases, the exchange interaction is symmetric, that is to say, the right-handed chiral domain and the left-handed one have the same energy. However, in a magnetic system with DMI, this symmetry is broken, indicating that two different chiral domains have different energies. The energy induced by DMI can be written as [112]:

$$E_{DM} = \sum_{i,j} \boldsymbol{d_{ij}} (\boldsymbol{S_i} \times \boldsymbol{S_j}) \tag{1.23}$$

where $\boldsymbol{d_{ij}}$ is the Dzyaloshinskii–Moriya vector, and it can be written as $\boldsymbol{d_{ij}} = d_{ij} \cdot (\boldsymbol{z} \times \boldsymbol{u_{ij}})$. $\boldsymbol{z}$ and $\boldsymbol{u_{ij}}$ are unit vectors, respectively perpendicular to the film plane and pointing from site i to site j. For $d_{ij} > 0$, the chiral spins tend to be arranged like ↑→↓, namely clockwise rotations from S_i to S_j. We denominate it the right-handed chirality. Correspondingly, the left-handed chirality favors the anticlockwise ↑←↓ spin [113-116].

In HM/FM/Oxide structures, the DMI is considered to arise from two different origins, the Fert-Levy model at FM/HM interface [117,118] and the Rashba spin-orbit coupling at FM/Oxide interface [119,120].

The nonmagnetic atoms with large SOC mediate the DMI between two ferromagnetic atoms,

resulting in a DMI vector perpendicular to the plane of the triangle formed by the three atoms and along the FM/HM interface. This 3-site indirect exchange mechanism which can be used to describe the DMI at FM/HM interface is referred to as the Fert-Levy model [107,117,118]. According to a calculation utilizing Vienna Ab-initio Simulation Package (VASP) [121], layer resolved DMI for Co (3)/Pt (3) bilayers and the distribution of the SOC energy are presented in Figure 1-18. It can be found that the predominant contribution of the large total DMI is attributed to the isotropic exchange coupling between the interfacial Co and Pt atoms. And the total DMI is decreased when intermixing between Co and Pt layers at interface occurs. The large DMI strength between spins of the interfacial Co atoms originates from the large SOC energy change in the adjacent interfacial Pt layer which is consistent with the Fert-Levy model [122]. Moreover, Belabbes A. *et al.* calculated the chemical trend of DMI for a series of *3d* transition metals deposited on different *5d* heavy metals using the first-principles calculations with the FLAPW method [123]. They attributed the DMI changes at various FM-HM interfaces not only related to the strength of spin-orbit coupling in the *5d* heavy metals but also to the orbital hybridization between the *3d* states and the *5d* states around the Fermi level at the interface. It is controlled by the Hund's exchange field of *3d* states of the magnetic transition metals according to the Hund's first rule. In more detail, the spin-flip mixing of the *3d* orbital states and the electron hopping with the intermediate spin-orbit active 5d states play a significant role in controlling the sign and the strength of DMI.

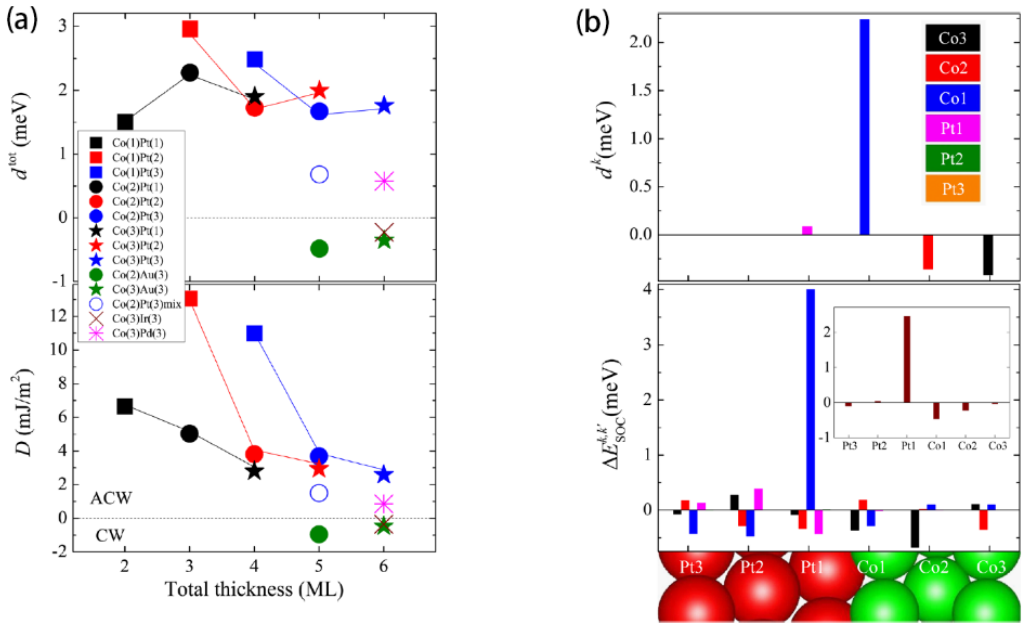

Figure 1-18. (a) Schematic of the total DMI parameter d^{tot} and the micromagnetic DMI coefficient D of the Co/Pt bilayers (b) Sketch of the layer resolved DMI parameter d^k for Co(3)/Pt(3) bilayers and the distribution of the SOC energy difference associated with the layer resolved DMI $\Delta E_{SOC}^{k,k'}$ and the total

DMI $\Delta E_{SOC}^{tot,k'}$. Image from[121].

In addition, it has been shown that the interface of FM and oxide [119,120], even graphene [124], could also induce DMI. Such DMI cannot be explained by the hybridization between 3d states of the magnetic transition metal and 5d states of heavy metal around the Fermi level. Yang *et. al* [120] reported a 60 percent increase of DMI in Pt/Co/MgO structures compared to Pt/Co bilayers. Moreover, according to the *Ab initio* calculation, at the interface of MgO/Co, the SOC energy is located in the interfacial Co, rather than the 5d heavy metal, indicating a different mechanism from the HM/FM interface. Since metal and oxygen ions carry large positive and negative charges, the oxide compounds are naturally highly ionic [125]. This property with the combination of the breaking inversion symmetry, results in an embedded electric field along the normal direction of the interface, and SO interaction is at the essence of the so-called Rashba effect [126]. Usually we regard the partial Rashba Hamiltonian as $H_R = \frac{\alpha_R}{\hbar}\boldsymbol{\sigma} \cdot (\boldsymbol{p} \times \boldsymbol{z})$, which is supposed to break the structural inversion symmetry [47,127-130]. By taking into account the Rashba coefficient α_R, Yang *et. al* [120] calculated the Rashba splitting for the MgO capped 3 ML of Co, getting the value of d^{tot} between 0.81 and 1.55 meV. This smaller value, compared with their DFT results of 1.88 meV, could be attributed to the fact that the Rashba-type DMI was calculated by using only one band close to Fermi level, but in fact other bands from Fermi level may also contribute to the total DMI. Belabbes *et al.*[131] further studied the physical mechanism of the DMI at Oxide/FM interface by calculating the control of DMI through interface oxidation using density-functional theory (DFT) with FLAPW method as implemented in the FLEUR code. They used the system of O/Fe/Ir (001) to explore the impact of the surface oxidation on DMI, and drew a conclusion that the sign and the strength of DMI strongly depend on the charge transfer and related hybridization between 2p-O and 3d-Fe states around the Fermi level which induces an electric surface dipole moment. In other words, the DMI of Oxide/FM structures is related to a large charge transfer and the large interfacial electric field that compensates the small spin-orbit coupling of the atoms at the interface.

Tunable DMI in Pt/Co/MgO structure is studied due to its high SOC at the interface. By inserting a dust of Mg between Co/MgO interface, DMI can be strongly enhanced by 5 times with the increasing MgO thickness, due to the increase of Co-O band [132]. For the HM/CoFeB/MgO system, the induced DMI is slightly inferior, but there are more possibilities influencing interfacial DMI. Torrejon *et al.*[133] and Gross *et al.* [115] controlled the interfacial DMI as well as the magnetic chirality by changing heavy metals in HM/CoFeB/MgO

structure. Moreover, thermal annealing is found to be helpful for enhancing DMI in Ta/CoFeB/MgO due to the diffusion of B atom, similar to the mechanism of PMA.

1.4 Summary

In this chapter, we have reviewed the different concepts of MRAM technology and in particular we have discussed the importance of DMI and SOT in DW based devices driven by currents. We have also highlighted the important impacts of interface conditions on spin-dependent interfacial effects, such as PMA and DMI, as well as DW dynamics.

Chapter 2 Experimental Methods

In this chapter, the fabrication and characterization techniques used in this PhD research will be introduced. The first part will describe the sample fabrication process, including film deposition, annealing, Hall bar fabrication process flow, and in particular light-ion irradiation, which is a useful method to control magnetism at the atomic scale. The relevant and useful characterization techniques we have used will be described in the second part. These techniques include characterization of the thin film morphology, magnetization, and electrical transport properties.

2.1 Sample Fabrication

2.1.1 Ultra-thin film Sputtering

Heavy metal (HM)/ ferromagnetic metal (FM)/oxide heterostructure with perpendicular magnetic anisotropy (PMA) has a great potential to hold high thermal stability, large TMR value and low critical switching current, which are required for the MRAM [31]. To optimize the performance of this structure, high quality thin films with an accurate control of the film thickness is the key point. During the past few decades, magnetron sputtering has been widely used in both industrial and academic domains, as it can provide high growth rate, relatively good yield, and precise thickness control at the atomic scale over 300 mm wafer [134,135].

Magnetron sputtering is a kind of Physical Vapor Deposition (PVD) technique. Figure 2-1 shows the schematic diagram of the sputtering process. With the presence of electric field (between the anode and cathode), the electrons are accelerated and collide with the incident argon atoms. The ionized argon ions (Ar^+) then strike the target surface with extremely high energy under the effect of electric field. Finally, the sputtered target atoms fly towards the substrate allowing the growth of a thin film at an atomic scale. Note that usually a magnetic field is also applied in addition to the electric field to force the electrons to move spirally by Lorentz force, hence increasing the chance of electrons to collide with the Ar gas.

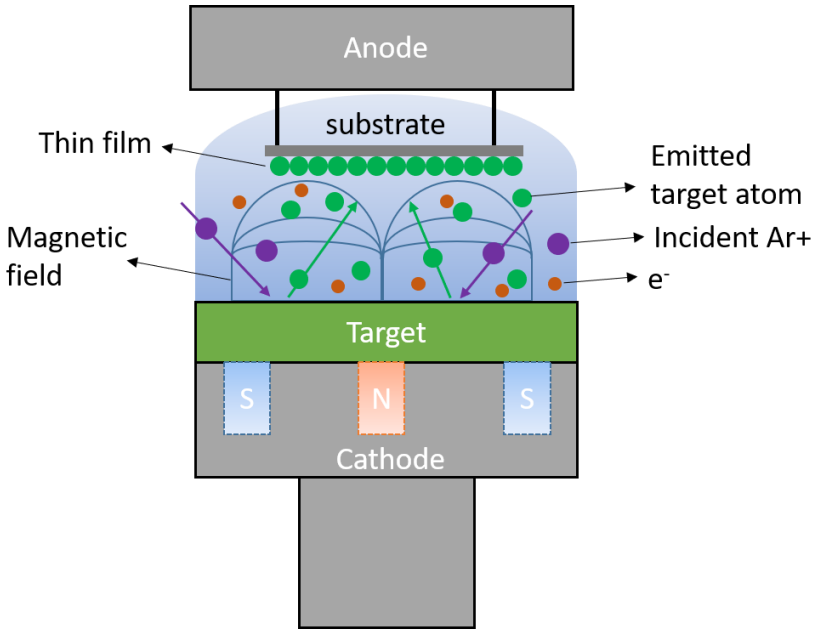

Figure 2-1. Schematic diagram of the deposition process in a magnetron sputtering chamber. Note that here we only show the chamber with a single target, whereas typical tools can include 6-8 targets.

In order to grow our CoFeB-MgO based ultra-thin films with PMA, we have used a sputtering system of AJA, as shown in Figure 2-2, as well as a Rotaris tool from Singlus Technologies. These industrial R&D tools allow for the growth of ultrathin layers with an atomic control of their thickness on large scale (200-300mm).

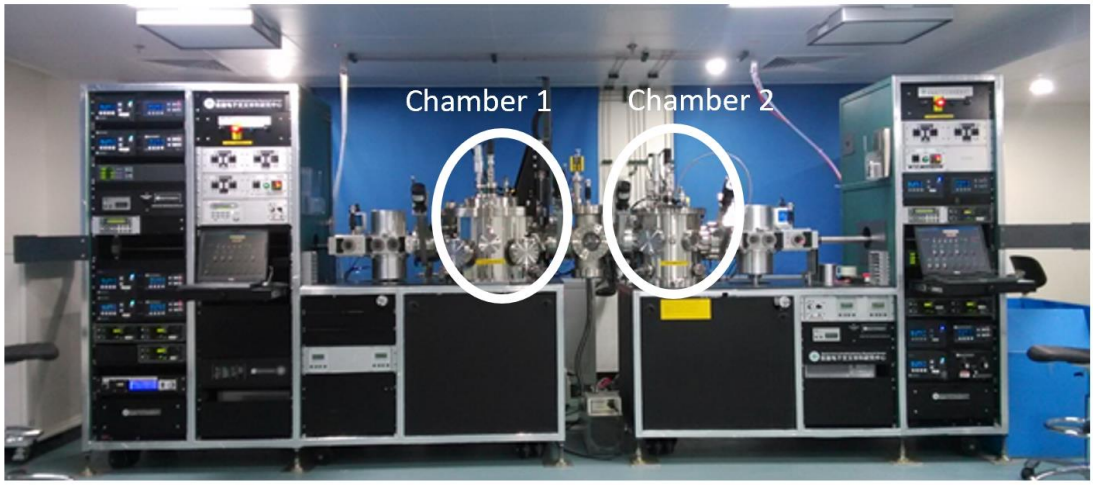

Figure 2-2. One of the sputtering system used in my PhD: AJA sputtering equipment. Two chambers are connected by a transfer chamber, in which there are 8 and 7 target holders, respectively.

2.1.2 Magnetic Annealing

Following the deposition of ultra-thin films, annealing treatment at high temperatures (typically >300°C) has been applied to induce crystallization of the CoFeB-MgO layers. In fact, a perfect crystallization of MgO is the prerequisite to obtain a high TMR value [136,137] as

well as high PMA [138]. Previous researches have shown that doping the CoFe layer with B leads to an amorphous nature of the CoFeB film, which favors a polycrystalline MgO films with good bcc (001) lattice when the structure is deposited at room temperature. The following annealing process at high temperature induces the crystallization of the CoFeB and MgO layers, enabling high performance of CoFeB-MgO based MTJ structure [139]. As shown in Figure 2-3, during annealing, the lightest B atoms are driven out of the CoFe layers inducing its crystallization [99], and a bcc lattice based on the template of textured MgO.

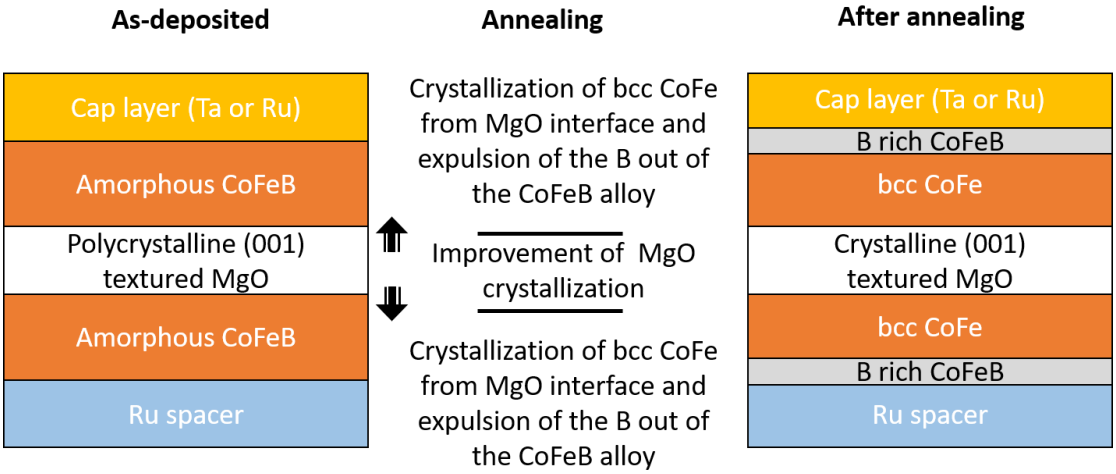

Figure 2-3. The change in crystal structure under annealing at temperatures above 300°C.

The annealing process includes *in situ* and *ex situ* annealing according to whether the chamber is integrated to the sputtering chamber [134]. Usually the *in situ* annealing just follows the MgO deposition on top of the first CoFeB layer in order to obtain monocrystal MgO film. After all functional films are deposited, the wafer will be put into the *ex situ* annealing chamber to induce the crystallization of the second CoFe(B) layer. It is worth noting that an extra magnetic field is also necessary sometimes to assist the annealing process to define the magnetization direction for in plane magnetized MTJs.

2.1.3 Hall bar Fabrication

After the film deposition and annealing procedure, specific samples are used to fabricate microwires with electrode pads, namely Hall bar devices, for the further measurements of spin orbit torque switching. Figure 2-4 presents the full fabrication process flow of microwires used in this thesis. After deposition, samples are first rinsed into anhydrous alcohol and ultrasound for 3 minutes (step 1) in order to clean up the surface.

Before spin coating (step 2), we have used mixed O_2 and Ar_2 plasma to remove the organic impurities and adsorb water molecules from the surface, hence enhancing the adhesion

between the photoresist and the sample surface. In step 2, the photoresist is deposited by a spin coater with a spinning speed of 4000 rpm, 60 s. Here we have used the negative resist ma-N 1420, for the exposed region is hard to dissolve in developer, as shown in step 4.

After the sample has been coated with photoresist and baked for one minute, it is exposed to UV-light (ultraviolet light) through a mask to produce the pattern image on the resist. Step 3 in Figure 2-4 shows the process of optical lithography.

After exposure for 18 seconds, samples are soaked into developer to remove the resist in the non-irradiated area. The developing time is 130-150 s for 10 μm wire and 190-210 s for 3-5 μm wire.

Then the sample is etched through the resist mask using ion beam etching (IBE). It is a dry etching method using accelerated Ar^+ to sputter thin films. The etching process recipe is as follows: injection of Ar gas at 5 sccm and 4.5×10^{-4} mBar, acceleration voltage of 750 V, beam current of 210 mA, rotation of the wafer holder at 10 rpm. Etching stops at the substrate layer.

After etching, the samples are soaked in acetone for at least 1 hour to dissolve the remaining photoresist. Ultrasonic bath for several minutes can help to speed up this process. Samples then are blow-dried with nitrogen. To ensure that all the resist has been removed, a 30s oxygen plasma bath is helpful.

Step 7-11 corresponds to the fabrication process of electrode pads. Positive photoresist BP-212-7S is spin coated on the sample surface at 4000 rpm, then after an aligment procedure the sample is exposed to UV-light during 3.6 s. After 50s in developer, the shape of the pad is transferred into the resist. Electrodes of Ti (20 nm)/Au (80 nm) are then deposited by electron beam evaporation. The last step is dissolving the remaining resist in acetone for 6 hours, followed by a 1-minute ultrasonic bath.

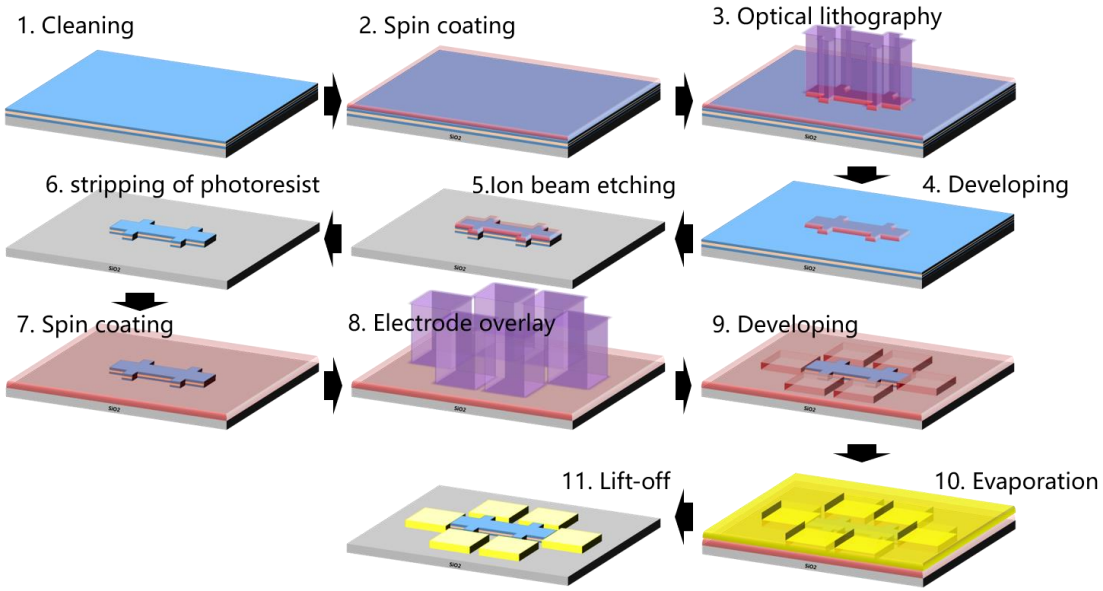

Figure 2-4. The fabrication process flow of magnetic microwires with 6 electrode pads.

It is worth noting that a very important step in the full process flow is the alignment. Figure 2-5 (a) shows the alignment mark patterned during the first optical lithography step (step 3), and (b) the mark in the second lithography layout. Step 8 corresponds to the alignment of (a) and (b) in order to contact the electrode pad with the magnetic wires precisely. Figure 2-5 (c) presents the observed mark after full fabrication process.

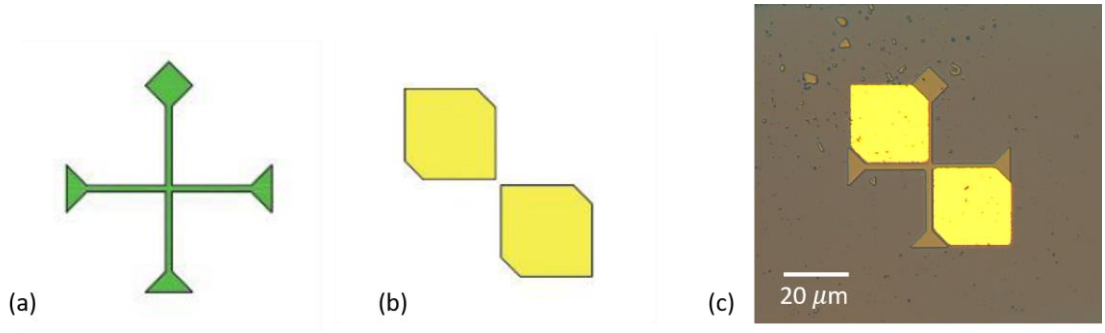

Figure 2-5. (a) Schematic diagram of the alignment marks during the first optical and (b) second lithography steps. (c) Scanning electron Microscope image showing a good alignment The square on the top indicates the up direction of the sample.

2.1.4 Light-ion irradiation

Irradiation is a powerful tool that can modify the structural properties of magnetic materials at the atomic scale. Since magnetic properties strongly depend on local structural properties, magnetic properties can be tailored through ion irradiation. Instead of implanting ion where ionic species are implanted into the active layer, ion irradiation is related to ionic species going through the layers and implant deep into the substrate. While ions going through the sample, atomic displacements are induced, leading to the modification of the structure and the related magnetic parameters, as shown in Figure 2-6. In order not to induce defects in the materials through cascade collisions or energy spikes such as Ar^+ or Ga^+ heavy ions used for etching materials, it is crucial to use light ions such as He^+. The typical energy of He^+ ranges from 10 to 100 keV [140,141]. in which the average energy transferred by the ions is very low (~100-200 eV) [142]. In this case, only short-range atomic displacements (1-2 inter-atomic distances) occur, providing very precise control over the “mixing rate”.

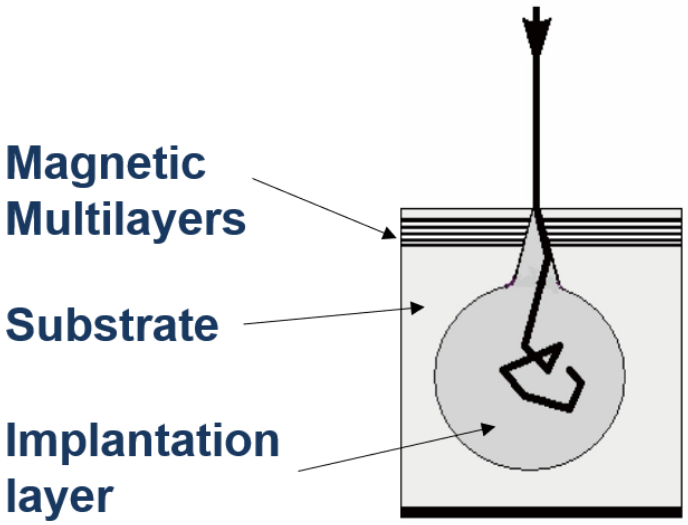

Figure 2-6. Schematic of the irradiation process. The energetic ions thread the multi-layers, after the energy exchange, finally stop at the substrate.

In this thesis, we use He^+ ions with an energy of 15 keV and fluences (irradiation doses, ID) ranging from 2×10^{18} to 3×10^{19} ions/m^2. The irradiation experiments are all conducted at room temperature. We also use an ion beam facility developed in the laboratory, which integrates and Electron Cyclotron Resonance (ECR), a curved magnetic to select the right ionic species, a Einzel lens to focus the beam and an electrostatic scan unit to scan the beam (1mm) over the sample up to 2×2 cm^2.

In chapter 3, we will present some results of irradiation on full films, while in chapter 5, local irradiation through a mask in Hall devices is used to study SOT switching. In detail, we spin coated the 2 μm positive photoresist on the samples after the standard Hall bar fabrication process. Then, an extra lithography is conducted to open some areas. As shown in Figure 2-7, the red squares in (a), (b) and (c) represent the regions without photoresist. We denominate these devices in Figure 2-7 as Type A, B, C, and D. These samples are then irradiated to locally modify the magnetic properties. Afterwards, the photoresist is removed by acetone.

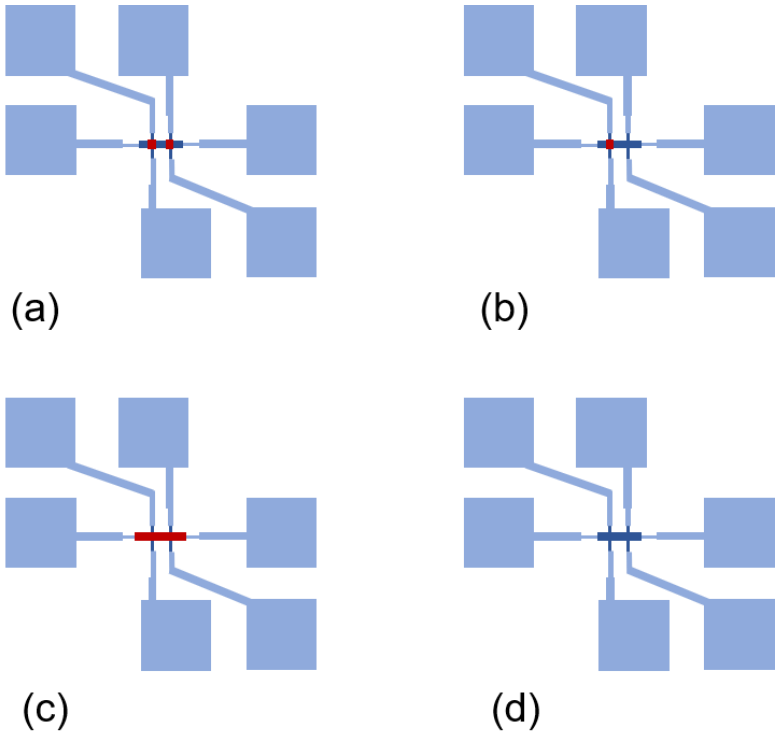

Figure 2-7. Schematic of the Hall bars used for irradiation. (a) Type A, two Hall crosses are irradiated, (b) Type B, one of the Hall crosses is irradiated, (c) Type C, the main Hall path (current path) is completely irradiated and (d) Type D, control group, no irradiation.

As mentioned above, the magnetic anisotropy is directly related to the competition of various energies, including the magneto-crystalline anisotropy, the magnetostriction anisotropy [143] and the interfacial anisotropy, Co/Pt or Co/Pd system is the ideal research subject in which the interface anisotropy is predominant. After the irradiation is applied, the PMA in such structure is reduced due to the irradiation-induced intermixing at the interface [144-146]. Extended X-ray absorption fine structure (EXAFS) spectra has shown a CoPt-rich composition at the interface due to the migration of Co and Pt [147]. Later, the irradiation research focuses on the perpendicularly magnetized Ta/CoFeB/MgO structure. PMA and saturated magnetization both deteriorated after irradiation[73,148], which is due to the diffusion of Fe into Ta, resulting in an attenuated hybridization between the Fe-3d and O-2p orbitals[94]. Figure 2-8 presents the Fe intensity ration (Fe intensity divided by the Fe intensity of the pristine film) monitored at the CoFeB/MgO interface. An irradiation-induced decrease in the Fe content at the MgO/CoFeB interface and a Fe accumulation close to the sample's surface at the CoFeB/Ta interface can be observed, which is the evidence of an irradiation induced Fe content depletion at the CoFeB/MgO interface [73].

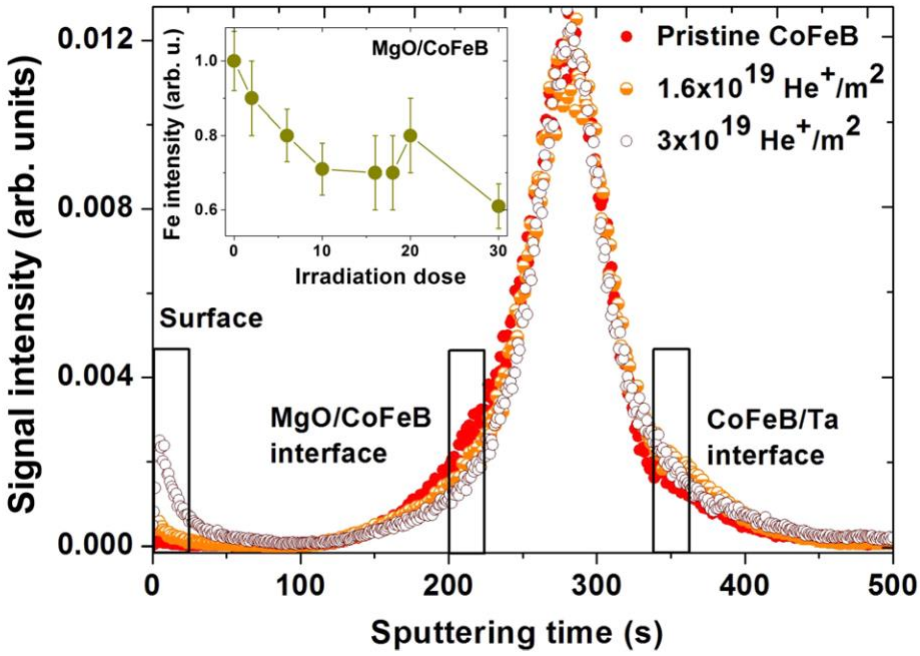

Figure 2-8. Signal intensity of Fe as a function of the sputtering time. The evolution of the Fe intensity ratio at the MgO/CoFeB interface is shown in the inset for the full range of *ID*s. Figure from Ref [73].

Recent studies have also shown that using He+ ion irradiation induced intermixing in Ta-CoFeB-MgO films could also lead to a slight increase on DMI [75], which is attributed to the irradiation induced asymmetric disorder on a scale of 0.1nm between the bottom and top interfaces. In addition to these interfacial effects mentioned above, the DW dynamics, especially the DW motion in the creep regime is also governed by the interface condition. Interestingly, the DW velocity shows the opposite trend upon irradiation in different material systems [73,149]. This stimulated our interest in digging out the underlying mechanism about how the irradiation influences the DW dynamics. It is also an important component of this thesis, which will be discussed in more detail in Chapter 5.

2.2 Sample measurements and characterizations

2.2.1 Vibrating sample magnetometry (VSM) and superconducting quantum interference device (SQUID) for anisotropy measurements

Vibrating sample magnetometry (VSM) and superconducting quantum interference device (SQUID) are similar techniques used to measure the hysteresis loop, from which we can obtain important magnetic properties, such as the coercivity (H_c), the anisotropy field (H_k), the saturation magnetization (M_s) and the direction of magnetization. The basic principle of them is that small piece of samples vibrates in the magnetic field with a fixed frequency, and the test coil detects the inductive electromotive force induced by the alternating magnetic field

in space. This inductive electromotive force is proportional to the magnetization of the measured sample. The difference between SQUID and VSM is that SQUID integrates a superconducting loop with Josephson junctions, which is used to detect the flux change and convert the flux change into voltage. This can largely improve the sensitivity of SQUID down to 10^{-8} emu, while the VSM sensitivity ranges from 10^{-5} to 10^{-6} emu.

By rotating the sample plane, perpendicular and in-plane magnetic field both can be applied on the sample. For the perpendicularly magnetized sample, one can get the hysteresis loop in the easy axis by applying perpendicular field while the in-plane field is for the hard axis. Typically, M_s could be extracted by using VSM or SQUID when magnetic field is applied along the easy or hard axis, while H_k can be obtained under the hard axis field. Thus, the effective anisotropy energy can be obtained by

$$K_{eff} = \frac{1}{2}\mu_0 M_s H_k \tag{2.1}$$

and the interface anisotropy energy in a CoFeB-MgO system can be derived from

$$K_i = (K_{eff} + \mu_0 M_s^2/2) \cdot t_{FM} \tag{2.2}$$

where t_{FM} is the thickness of ferromagnetic layer.

It is worth noting that M_s measured under the easy-or hard-axis should be the same. But in fact, in both VSM and SQUID magnetometry, the values of M_s obtained from the easy-and hard- axis can often exhibit a certain degree of discrepancy due to the sample geometry effect. The solution is to use a standard sample with a certain shape to calibrate the setup. Based on the experience, when thin films are measured, a practical method to correct for the geometry factor is to simply scale the out-of-plane moment (inaccurate) to that of the in-plane moment (accurate).

2.2.2 Magneto-Optical Kerr Effect (MOKE) for Hysteresis Loop Measurements

Magneto-Optical Kerr Effect (MOKE) is a local effect to detect the magnetic properties by using polarized light. When a linear polarized laser (Left- and Right- circularly polarized light) reflects from a magnetic material, the two circular lights travel with different velocities resulting in a phase shift between left-and right-circularly polarized light. In addition, the different absorption for left-and right-circularly polarized light, namely the circular dichroism, results in a difference on the polarization amplitude, leading to ellipticity. This arises from the interaction between the oscillation electric field of the incident laser and the sample magnetization [150]. Thus, Kerr rotation as a function of the magnetic field can be used to determine the hysteresis loop of the samples. The Kerr rotation is in general proportional to

the magnetization. This method enables us to determine whether the sample has perpendicular anisotropy or in-plane magnetization as well as the coercive field. MOKE magnetometry is a very powerful technique in spintronics due to its high sensitivity to magnetization (down to 10^{-12} emu [151]), as well as its ability to locally probe the magnetic property on scale of the focused laser beam (typically ~1 μm).

According to the magnetization direction of the measured material with respect to the plane of incident light, the magneto-optical Kerr effect can be divided into 3 geometries: the polar, longitudinal and transverse, as shown in Figure 2-9. For the polar MOKE in Figure 2-9 (a), the material magnetization is perpendicular to the sample surface but in the plane of light incidence; for the longitudinal MOKE in (b): the magnetization lies in the plane of light incidence as well as the plane of sample surface, while in (c) for the transverse MOKE: magnetization lies in the plane of sample surface but perpendicular to that of light incidence. Since the easy axis of magnetization presented in this research is perpendicular to the sample surface, the main technique used is the polar MOKE.

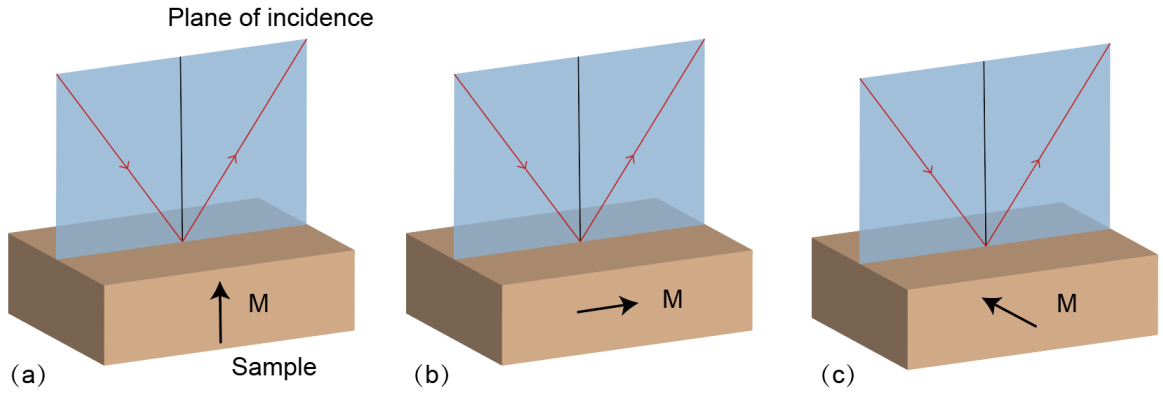

Figure 2-9. Geometry of three modes of MOKE. (a) Polar MOKE; (b) Longitudinal MOKE and (c) Transverse MOKE.

2.2.3 Kerr miscopy for DW Imaging

MOKE can also be used in a microscope to image the magnetic state of magnetic materials.

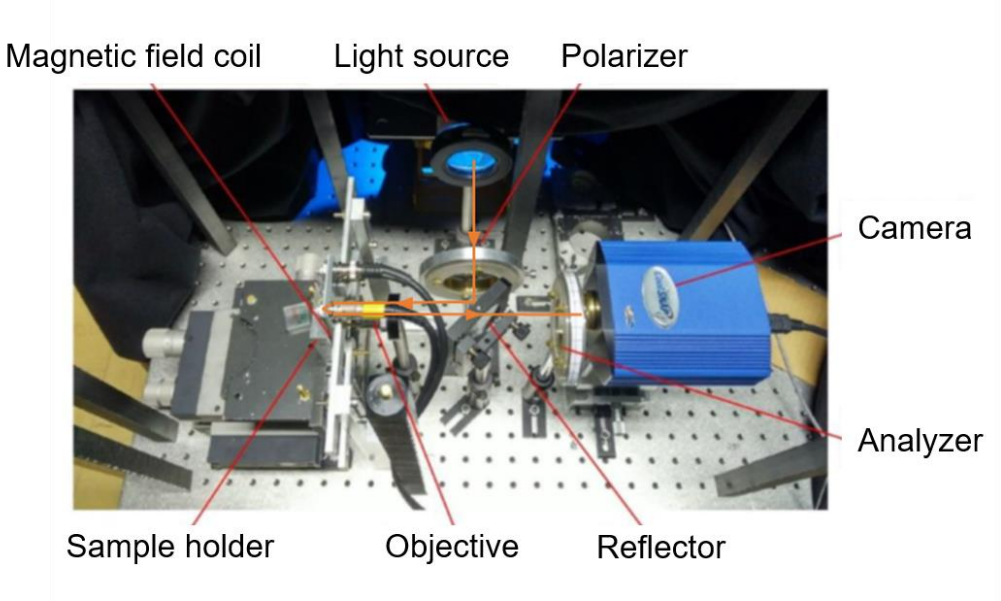

Figure 2-10. Polar Kerr microscope setup used to measure the domain wall velocity in this thesis. It was designed by Dr. Nicolas Vernier in C2N.

In this case, the typical configuration and the light path (orange lines and arrows) for a polar Kerr microscope are shown in Figure 2-10. The light emitted by a red laser diode, goes first through a polarizer, then it is reflected by a beam splitter and enters into the objective. The sample is placed very close to the objective. The light is then reflected by the sample surface with a rotation of polarization and travels back into the objective. After the reflector and analyzer, the light is finally captured by a charge coupled device (CCD) camera. A magnetic field is applied during the experiment either though an electromagnet or a micro-coil placed right behind the sample. Figure 2-11 presents a typical Kerr image of DW expansion, where the light contrast indicates the direction of magnetization. DW velocity can be measured through two consecutives images.

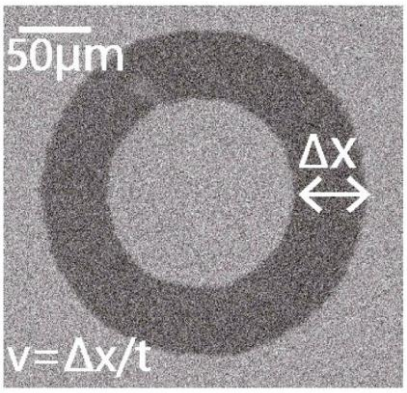

Figure 2-11. Typical image of DW expansion under a perpendicular field pulse allowing the measurement of DW velocity in a perpendicularly magnetized W(4 nm)/$Co_{20}Fe_{60}B_{20}$(0.6 nm)/MgO(2 nm)/Ta(3 nm) film.

Besides the BLS method described in the next paragraph, the DMI parameter can be

measured using DW experiments revealed by Kerr microscopy. In this case an additional in-plane magnetic field coil needs to be applied. The configuration is presented in Figure 2-12. Similar to the process of measuring DW velocity, the sample is first saturated by a perpendicular magnetic field, then a reversed domain bubble is created by a magnetic pulse in the opposite direction. Here, the first image is captured. In-plane and perpendicular field are then applied simultaneously in order to induce the asymmetric expansion of the domain. In this step, a second Kerr image is taken. Based on the image difference, with the presence of DMI, we can observe an asymmetric expansion of domain bubbles as illustrated in Figure 2-13. The DW displacement is along or against the in-plane field $d+$ or $d-$, and the DW velocity $v+=d+/t$ and $v-=d-/t$ can be obtained, where t is the pulse duration of the perpendicular field. Velocities under the same perpendicular field and various in-plane fields can be then determined. The effective DMI field is considered equal to the in-plane field corresponding to the minimum velocity [152].

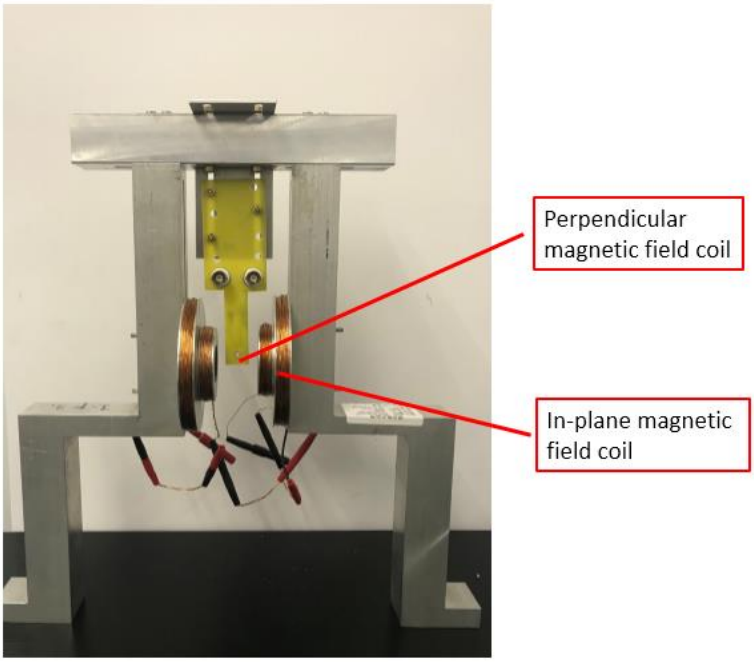

Figure 2-12. The configuration of the integrated perpendicular and in-plane magnetic field coils. It was designed by Dr. Xueying Zhang in Beihang University.

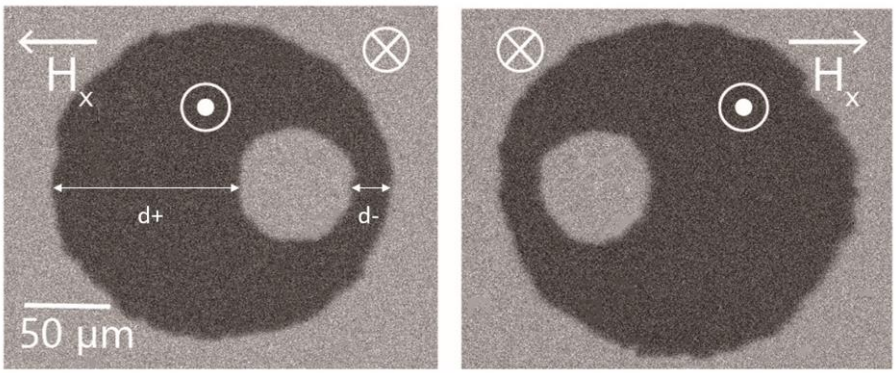

Figure 2-13. The asymmetric expansion of domain bubbles under an in-plane field of $\mu_0 H_x = \pm 23.2\ mT$ and perpendicular field of $\mu_0 H_z = 3.6\ mT$ of the same sample.

2.2.4 Brillouin light scattering (BLS) for DMI measurements

Brillouin light scattering (BLS) is another common method to estimate the DMI value. This methodology is based on the asymmetric spin-wave dispersion caused by the presence of the Dzyaloshinskii–Moriya interaction [153]. The typical configuration is shown in the inset of Figure 2-14. The magnetic field is applied in the sample plane and perpendicular to the incident plane of light, corresponding to the Damon-Eschbach (DE) geometry [154-156]. A shift in the frequency of the light is measured corresponding to the magnon creation and the magnon annihilation through the spin waves propagating along the -x and +x directions (so-called Stokes and anti-Stokes peaks, respectively). Figure 2-14 shows the Stokes and anti-Stokes peaks under the two opposite directions of the applied magnetic field, with a fixed incident angle, namely a fixed wave vector k_{SW} defined by $k_{SW} = 4\pi \sin(\theta_{inc})/\lambda$, in which θ_{inc} is the laser incidence angle and λ is the wavelength.

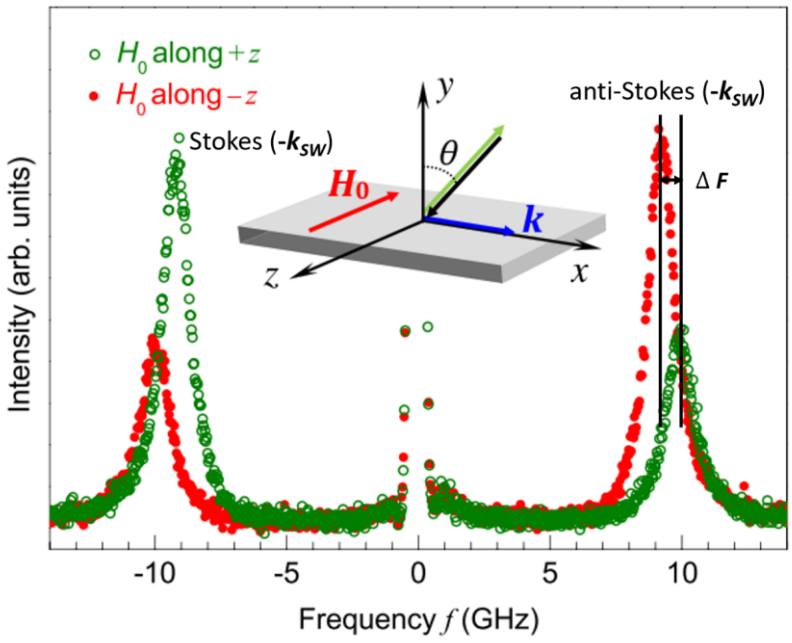

Figure 2-14. Brillouin spectra of a Pt/Co/Ni film, which is recorded at a fixed incident angle of $\theta = 45°$ ($|k| = 17.3\ \mu m^{-1}$) under oppositely oriented external magnetic fields $\mu_0 H_0 = 97\ mT$. Inset: schematic of the Cartesian coordinate system and 180° backscattering geometry. The incident and scattered light beams lie in the *x*-*y* plane and are at an angle θ to the *y* axis. The magnon wave vector is denoted by k_{SW}. Figure from Ref [154].

By measuring the frequency shift under different incident angles, the DMI value can be extracted from a linear behavior between the frequency difference ΔF and the spin wave vector k_{SW} as the following equation:

$$\Delta F = F_S - F_{AS} = \frac{2\gamma}{\pi M_s} D k_{SW} \tag{2.3}$$

where F_S and F_{AS} are the frequencies corresponding to the Stokes and anti-Stokes peaks, respectively. γ is the gyromagnetic constant, D is the DMI constant. This method can directly extract D without the dependence on parameters such as A_{ex} and K_{eff} [153].

2.2.5 Spin-dependent Electrical Transport Measurements

In addition to the magnetic properties measurement, electrical transport properties are also very useful to determine local magnetic properties in nanodevices. The main electrical transport measurements used in this thesis is based on anomalous Hall effect (AHE), which is a valid method to extract perpendicular magnetization [157], and characterize the SOT switching.

In the ferromagnetic metal material, the lateral resistivity ρ_{xy} relates not simply to the ordinary Hall resistance (Ordinary Hall effect) affected by the external magnetic field H and the Lorentz force, but to an anomalous term proportional to the perpendicular magnetization M_z. When the magnetization of the sample is saturated, the anomalous term keeps a constant. It can be expressed by

$$\rho_{xy} = R_0 H + \mu_0 R_S M_z \tag{2.4}$$

where R_0 and R_S are the ordinary and anomalous Hall constants, respectively. Usually R_S is an order of magnitude larger than R_0, closely associated with the temperature. The intrinsic origin of AHE is still a pending issue, while the most acceptable explanation is the electron skew scattering or side jump induced by SOC when electrons move along the long axis.

Therefore, AHE can be used to characterize the magnetic properties of the sample. In this PhD research, we applied a constant in-plane magnetic field that is collinear with the current. In this case, the perpendicular magnetization switching property can be reflected by the resistance change with the sweeping current.

The measurement system is a physical properties measurement system-vibrating sample

magnetometer (PPMS-VSM), combined with a Keithley 6221 current source, and a 2182 nanovolt metre in a Hall bar device. The configuration is shown in Figure 2-15. The long bar is the current path, while the voltage is measured by two electrode pads extending from the current path. The LabView program is used to control the magnitude and direction of the vertical magnetic field generated by the superconducting magnet. And the resistance that changes with the magnetic field or current can be presented in real time.

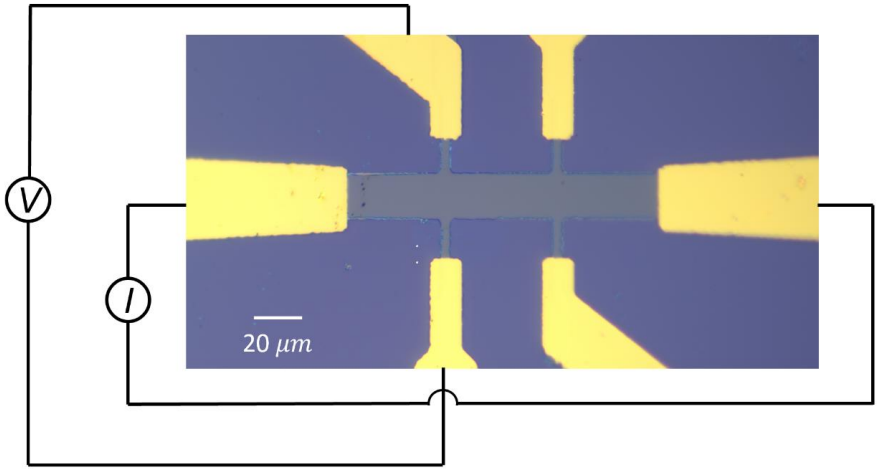

Figure 2-15. Hall bar device and the configuration of electrical transport measurement.

2.3 Summary

In this section, we present the sample fabrication process, including films deposition, annealing Hall bar fabrication process and ion irradiation. Then characterization techniques for measuring both magnetic parameters and electrical transport properties used in my Ph.D. research are demonstrated.

Chapter 3 Precise Modulation of Spin-Dependent Interfacial Effects

In this chapter, I will explore the precise modulation of spin-dependent interfacial effects, including PMA and DMI, through thin film deposition, post-annealing and ion-irradiation process. The investigated samples are SiO_2/ Ta (3)/ MgO (1)/ $Co_{20}Fe_{60}B_{20}$ (*t*)/ Ta (2)/ Ru (5) and W(4)/$Co_{20}Fe_{60}B_{20}$(*t*)/MgO(2)/Ta(3) (thicknesses in nm), which was deposited on highly resistive Si wafers using dc/rf magnetron sputtering at room temperature. The former structure was deposited by AJA magnetron sputtering system located in Beihang University, while the latter was deposited by Rotaris sputtering system located at Singulus Technologies AG.

3.1 Modulation of magnetic anisotropy through different methods

3.1.1 FM thickness dependence of magnetic anisotropies

In this section, we grow the films with the structure of SiO_2/ Ta (3)/ MgO (1)/ $Co_{20}Fe_{60}B_{20}$ (t)/ Ta (2)/ Ru (5) using AJA magnetron sputtering system at a base pressure of 1×10^{-8} mTorr (numbers in parenthesis are nominal thicknesses in nanometers). The sputtering conditions are shown in Table 3-1. We have varied the CoFeB thickness by controlling the sputtering time. The film thickness has been calibrated by X-Ray Reflectivity.

	Ta	MgO	CoFeB	Ta
Ar pressure (mT)	4	6	4	4
Power supply (W)	49	60	60	49
Sputtering time (s)	86	495	-	58
Thickness (nm)	3	1	t	2

Table 3-1. Sputtering conditions of thin films with structure SiO_2/ Ta (3)/ MgO (1)/ $Co_{20}Fe_{60}B_{20}$ (t)/ Ta (2)/ Ru (5) (The conditions of top-capping layer Ru are not shown here, due to its triviality for this system).

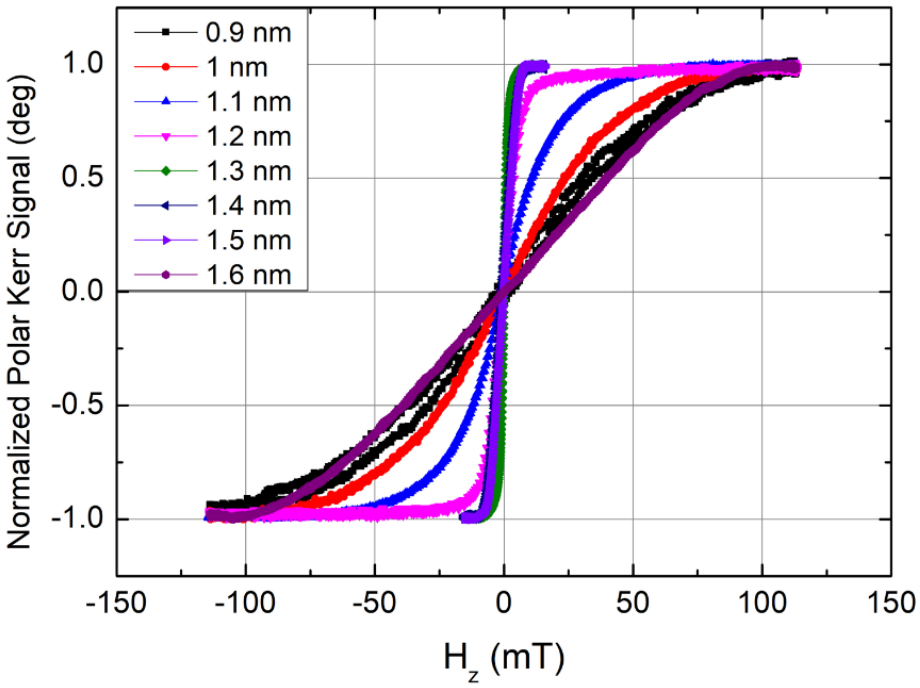

Figure 3-1. Polar Kerr signal vs. perpendicular magnetic field for pristine SiO_2/ Ta (3)/ MgO (1)/ $Co_{20}Fe_{60}B_{20}$ (t)/ Ta (2)/ Ru (5) samples with different CoFeB thicknesses.

Figure 3-1 presents the out-of-plane hysteresis loops of the pristine films (no annealing) for different CoFeB thicknesses. The loops are obtained by using polar-MOKE, in which an out-of-plane field is applied. As we can observe, for the thicknesses of 0.9 and 1.0 nm (black and red), samples show paramagnetism, which is confirmed by the in-plane hysteresis loop in Figure 3-2 (a). This paramagnetism is attributed to the overall weak magnetism resulting from the relatively small FM thickness. When the FM thickness is slightly increased above 1.1 nm, the magnetization tends to be perpendicular to the film plane. Because in relatively thin ferromagnetic materials, the bulk anisotropy constant is small and can be neglected, only interface and shape anisotropy contribute to the total anisotropy [31]. In the competition between these two anisotropies, the interfacial one is dominant, leading to the out-of-plane anisotropy. As we can see in Figure 3-2 (b), the out-of-plane hysteresis loop is sharper than that of the in-plane with 1.3 nm CoFeB as a result of a strong PMA. For the non-annealed films, the magnetization maintains PMA up to a thickness of CoFeB of 1.5 nm. In Figure 3-2 (c), PMA decreases due to a larger contribution of the shape anisotropy.

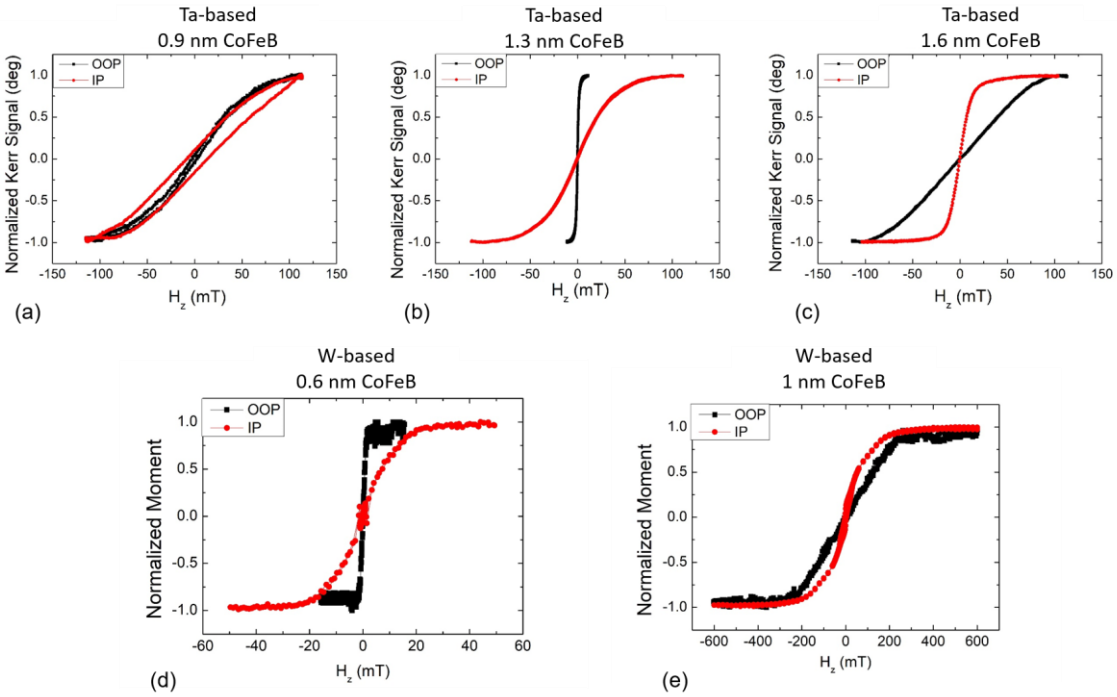

Figure 3-2. The in-plane (red dots) and out-of-plane (black squares) hysteresis loops for the pristine sample with (a) 0.9 nm, (b) 1.3 nm and (c) 1.6 nm thick CoFeB on Ta and (d) 0.6 nm, (e) 1 nm CoFeB on W. All samples are not annealed.

In Figure 3.2 (d) and (e), we present the hysteresis loops of tungsten based structure: W (4)/$Co_{20}Fe_{60}B_{20}$ (t)/MgO (2)/Ta (3). It is clear that 0.6 nm CoFeB favors the perpendicular anisotropy while that of 1 nm tends to be in-plane.

It is worth noting that the thickness window that favors PMA are quite different between Ta- and W-based samples. One reason might be that the magnetic properties of CoFeB layers deposited on top and bottom of MgO layer are different due to the different thickness of dead layers [31,158]. The other reason for this could be the different sputtering conditions in different systems. Thus, well-controlled sputtering condition is crucial to modulate the magnetic anisotropy which will be detailed in next section.

All samples presented above are non-annealed. In particularly, Table 3-2 shows the relevant magnetic parameters of annealed W (4)/$Co_{20}Fe_{60}B_{20}$ (0.6 and 1)/MgO (2)/Ta (3) samples, which also highlight the FM thickness dependence of PMA.

	M_s (10^6 A/m)	H_K (kOe)	K_{eff} (10^5 J/m^3)	K_i (mJ/m^2)
1 nm CoFeB	1.36	3	2.04	1.37
0.6 nm CoFeB	0.85	9.3	3.95	5.09

Table 3-2 Magnetic parameters of annealed W (4)/$Co_{20}Fe_{60}B_{20}$ (0.6 and 1)/MgO (2)/Ta (3) samples. These two samples are both annealed at 400℃, 2 hours in the same chamber. M_s and H_K are measured by SQUID. K_{eff} and K_i are calculated according to Eq. (2.1) and (2.2), respectively.

3.1.2 Dependence of magnetic anisotropy on sputtering

This part is mainly focused on the samples with structure of SiO_2/ Ta (3)/ MgO (1)/ $Co_{20}Fe_{60}B_{20}$ (t)/ Ta (2)/ Ru (5), which were deposited in our lab by AJA system. In the course of the experiment, I found that sputtering parameters, especially the Ar pressure and power supply of the target could influence the magnetic anisotropy through interface roughness. We have prepared 3 sets of samples as shown in Table 3-3. Sample II corresponds to different Ar pressures whereas power supply is varied for sample III keeping the other parameters constant.

		Ta	MgO	CoFeB	Ta
I	Ar pressure (mT)	4	6	4	4
II				10	
III				4	
I	Power supply (W)	49	60	60	49
II				60	
III				90	
I	Sputtering time (s)	86	495	481	58
II				481	
III				321	
I/ II/ III	Thickness (nm)	3	1	1.4	2

Table 3-3. Sputtering parameters for 3 sets of samples.

Based on our experiment results, the Ar pressure makes no difference on the sputtering rate, while the power supply does. This is because with the increase of Ar pressure, the target particles sputtered out will also increase. However, the collisions in the chamber between the Ar^+ and target atoms are going to increase as well, which may hinder the deposition of target atoms. Thus, within a certain range, the influence of Ar pressure on the sputtering rate can be neglected. However, Ar pressure has a great influence on the sample surface and/or the interface. Figure 3-3 shows the atomic force microscopy (AFM) images of sample type I and II. Obviously, type I with lower Ar pressure has a smoother surface while some bumps appear

in type II.

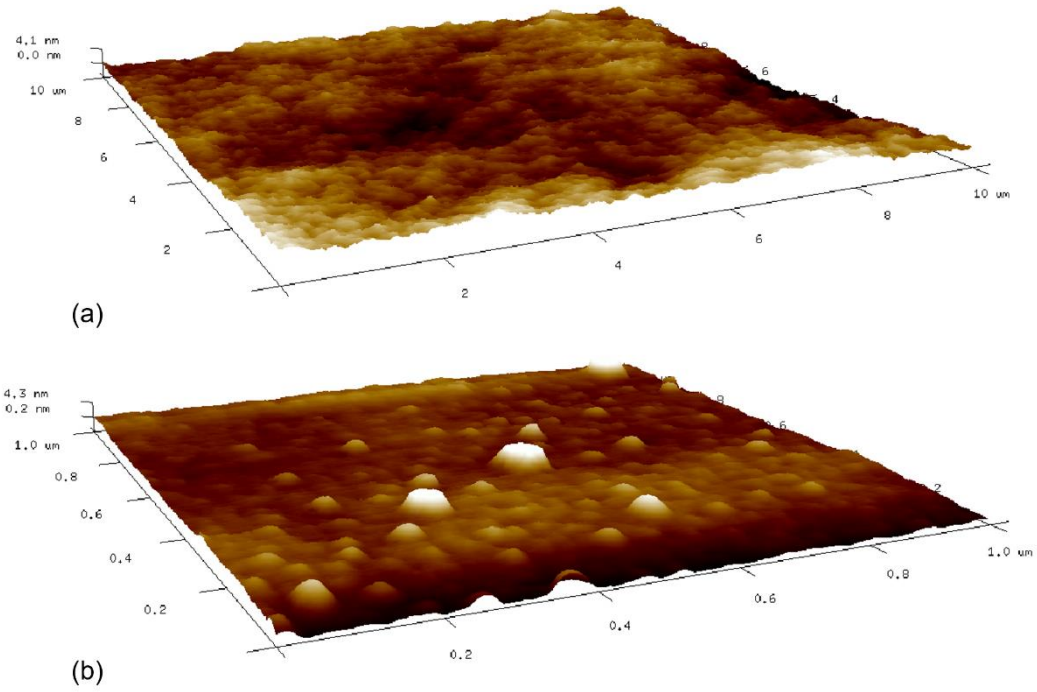

Figure 3-3. Atomic force microscopy (AFM) images of sample (a) type I and (b) II.

The target power supply strongly modifies the sputtering rate, as seen in Figure 3-4, where the sputtering rate of CoFeB layer as a function of the power supply shows a linear behavior. But the surface morphology is not significantly affected according to AFM.

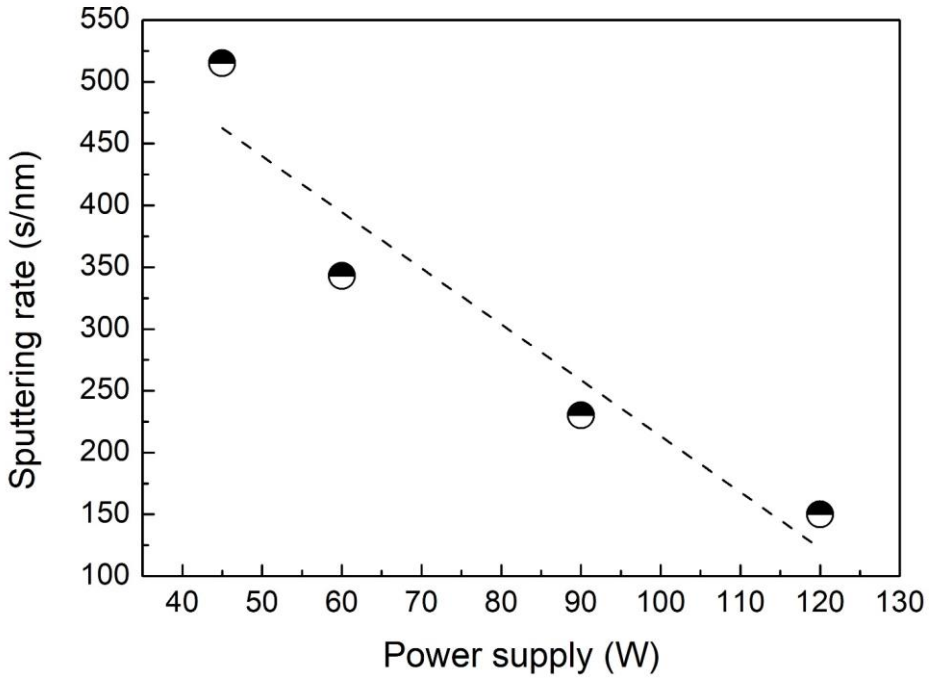

Figure 3-4. Sputtering rate of CoFeB film as a function of the target power supply at a constant Ar pressure of 4 mT.

The out-of-plane hysteresis loops of samples of type I, II and III are shown in Figure 3-5. Type I with the lowest Ar pressure and power supply exhibits very square hysteresis loops compatible with strong PMA. The squareness of the loops indicates that magnetization reversal is dominated by the nucleation of some reversed domains probably at some extrinsic defects followed by rapid DW propagation [60]. On the contrary, the tilted reversal loop of type II samples is caused by the DW propagation dominated reverse, which further reveals that the rough interface of CoFeB can be attributed to a magnetization reversal dominated by multiple domain nucleations where the propagation is blocked by strong pinning defects. Clearly, this indicates more rough and intermixed interfaces for samples of type II.

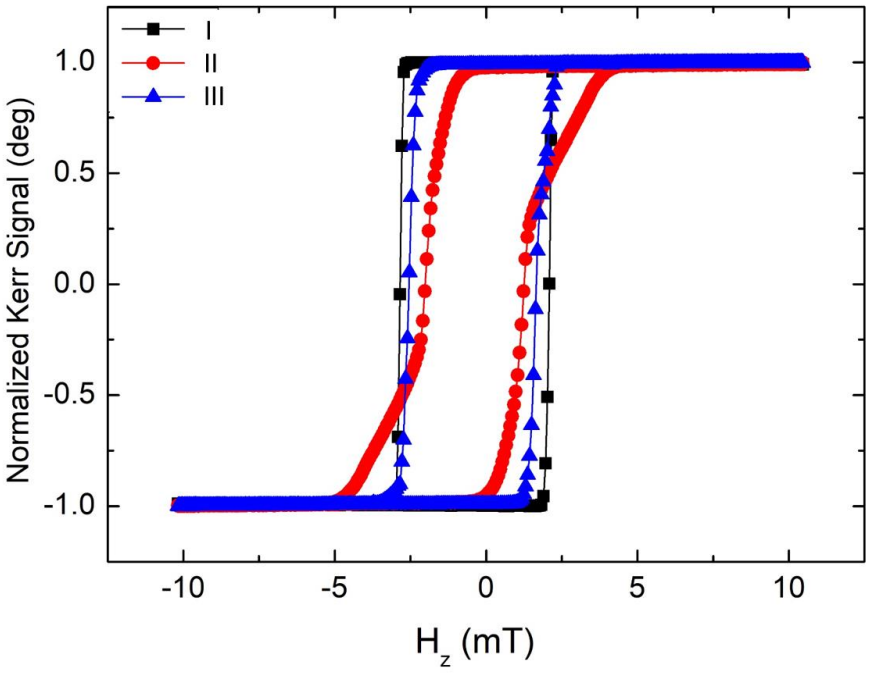

Figure 3-5. Out-of-plane hysteresis loops of samples of type I, II and III. Samples are annealed at 300℃, 1 hour after deposition. Measurements are conducted by using polar MOKE.

3.1.3 Dependence of magnetic anisotropy on annealing

Previous studies have demonstrated that annealing process could improve the magnetic anisotropy in the HM/CoFeB/MgO layers [99,159,160]. Both saturated magnetization and effective anisotropy increase to a maximum upon annealing and then decrease, as shown in Figure 3-6. The first increase of *M/V* (where *M* is the magnetization and *V* is the magnetic

volume) and K_{eff} is attributed to the absorption of B into Ta, leading to the crystallization of the amorphous CoFe layer from the bcc (001) MgO layer [99]. This facilitates the creation of a sharper interface between CoFeB and MgO. The following downturn of the two parameters results from the formation of an additional magnetic dead layer between the Ta and CoFe(B) layers.

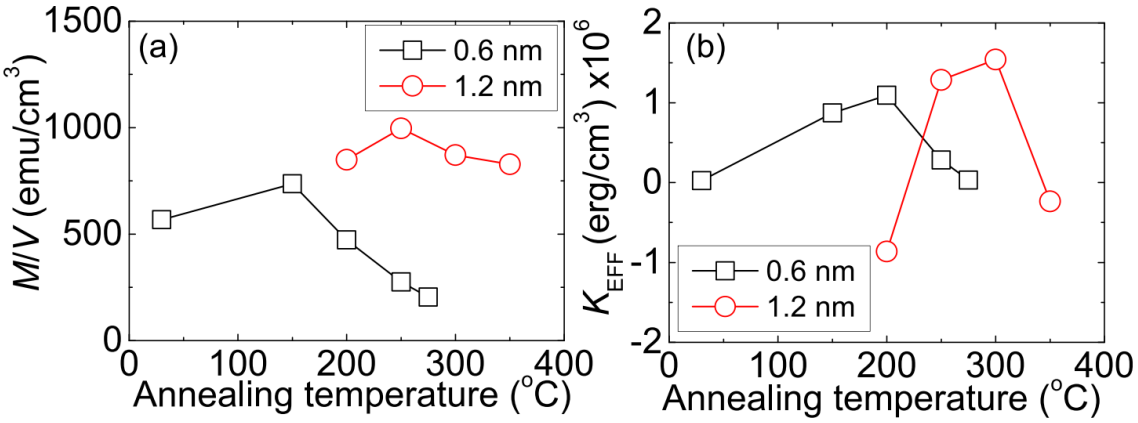

Figure 3-6. Annealing temperature dependence of (a) magnetic moment per unit volume (*M/V*) and (b) K_{eff} for films Ta (1nm)/ CoFeB (*t*)/ MgO (2)/ Ta(1): *t* is 0.6 nm for the black squares and 1.2 nm for the red circles. Images from Ref. [99].

In this thesis, we have investigated the influence of annealing on the magnetic properties of SiO_2/ Ta (3)/ MgO (1)/ $Co_{20}Fe_{60}B_{20}$ (1.4/1.5/1.6)/ Ta (2)/ Ru (5) structures, with the CoFeB sputtered at 4 mT Ar gas. The annealing parameters include the value of temperature, duration and perpendicular magnetic field. Figure 3-7 shows the out-of-plane hysteresis loops with different annealing conditions. For the thinner CoFeB layers (1.4 and 1.5 nm, Figure 3-7(a) and (b)), the coercive field increases with the temperature from 250℃ to 350℃. It is clearly seen that 350°C 1 hour thermal annealing is needed to induce sharper hysteresis loop and higher PMA. In addition, perpendicular magnetic field shows no effect on the hysteresis loops as we expect for PMA materials. The easy axis is only induced by the presence of interfaces and the crystal structure.

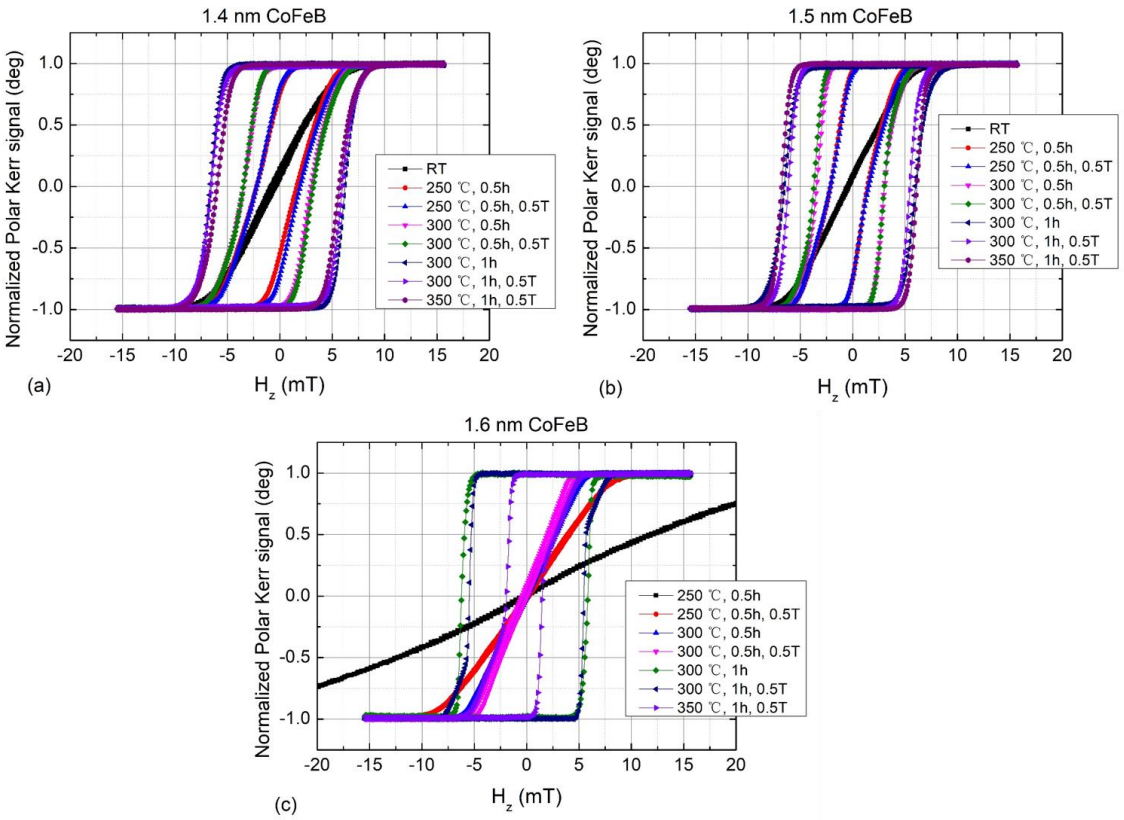

Figure 3-7. Out-of-plane hysteresis loops under different annealing conditions for samples with (a) 1.4 nm, (b) 1.5 nm and (c) 1.6 nm thick CoFeB layer.

In Figure 3-2(c), the as-deposited sample with 1.6 nm thick CoFeB layer exhibits an in-plane easy axis. Unlike 1.4 and 1.5 nm thick CoFeB layers, whose optimal PMA appears at 350°C 1 hour, 1.6 nm thick CoFeB exhibits strongest PMA at 300°C 1 hour, as shown in Figure 3-7(c). The annealing temperature of 350°C results in a degeneration of PMA.

From the comparison of 3 samples with different CoFeB thicknesses, one can see that for the as-deposited sample that exhibits weak PMA, annealing can enhance the anisotropy by sharping the interface and inducing the CoFeB crystallization. For pristine samples with thicker FM layer showing in-plane anisotropy, annealing can induce out-of-plane anisotropy. However, in this case, the diffusion of B into Ta is more limited [99], resulting in a narrow window for optimizing the anisotropy. In particular those thick CoFeB based samples are more sensitive to intermixing, which could explain that at 350°C, PMA is degraded.

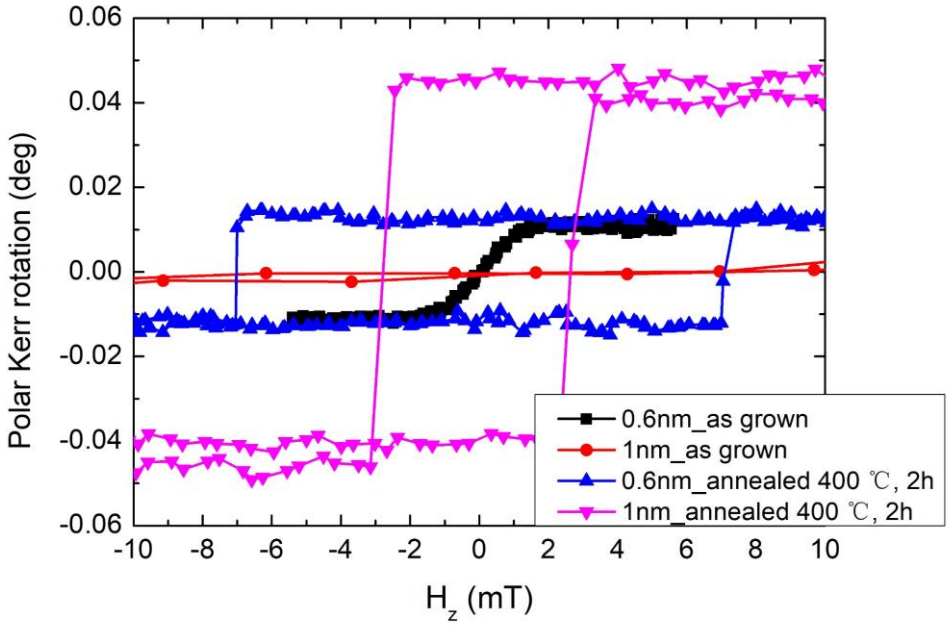

Figure 3-8. Out-of-plane hysteresis loops of sample SiO_2/W (4)/CoFeB (0.6/1)/MgO (2)/Ta (3), as-deposited and annealed at 400℃, 2 hours.

This part we also studied the W-CoFeB-MgO structure. We have first investigated annealed and not annealed SiO_2/W (4)/CoFeB (0.6 and 1)/MgO (2)/Ta (3) structures. In Figure 3-8, we present the out-of-plane hysteresis loops for the as-deposited and annealed samples. Similarly, after annealing, the perpendicular magnetic anisotropy is enhanced for both CoFeB thicknesses. Here, 400℃, 2 hours is the optimized annealing condition for W, which is higher than that of Ta. This can be explained by the fact that B diffusion is more difficult into W than Ta due to a different enthalpy of mixing. Also, for the same reason, W is more robust upon intermixing with Co and Fe (see Figure 3-11), making it favorable to sustain high annealing temperatures as it is done for embedded MRAM.

3.1.4 Ion irradiation for post-control of magnetic properties

In this part, we focus on annealed SiO_2/W (4)/CoFeB (0.6)/MgO (2)/Ta (3). The samples were irradiated by He^+ ions with an energy of 15 keV and fluences (irradiation doses, ID) ranging from 2×10^{18} to 3×10^{19} ions/m^2.

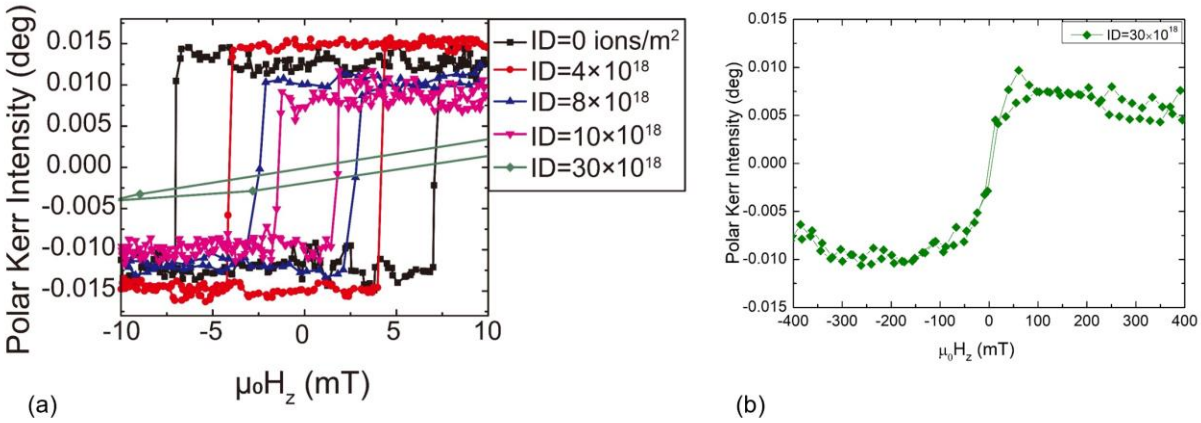

Figure 3-9. Hysteresis loops of annealed SiO_2/W (4)/CoFeB (0.6)/MgO (2)/Ta (3) samples irradiated (a) at different irradiation fluences (IDs), (b) specially at ID= 3×10^{19} ions/m^2 with large magnetic field region.

As shown in Figure 3-9 (a), the coercive field is reduced when the He^+ fluence is increased. For the largest dose of 3×10^{19} He^+/m^2, as shown in Figure 3-9 (b), the easy axis of magnetization tends to be in plane (it is hard to saturate the magnetization with perpendicular field). Figure 3-10 (a) and (b) show the saturation magnetization M_s, the effective anisotropy K_{eff} and the interface anisotropy K_i as a function of *IDs*. Here, M_s and H_k are measured by superconducting quantum interference device (SQUID) magnetometry under perpendicular and in-plane magnetic fields, respectively.

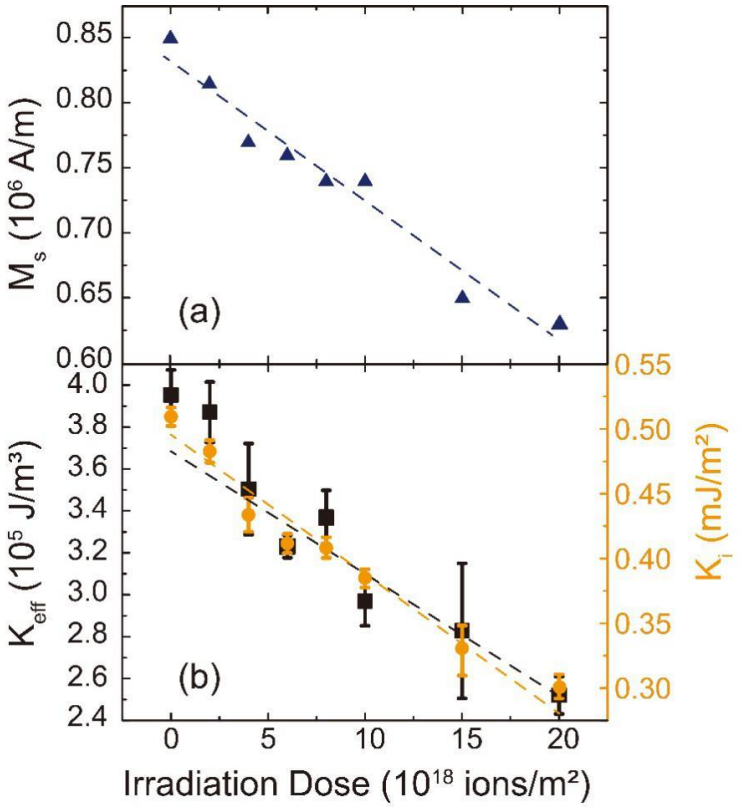

Figure 3-10. (a) Saturation magnetization M_s as a function of fluence. (b) Effective anisotropy (black

squares) and interface anisotropy (orange dots) as a function of fluence. Error bars correspond to uncertainties in the estimation of the anisotropy field H_k.

Upon irradiation, M_s, K_{eff} and K_i show a linear reduction as a function of fluence. This has been confirmed in Ta-CoFeB (1nm)-MgO systems, where the main effect of ion irradiation is to induce Fe diffusion into Ta [73]. Here also, the reduction of M_s is attributed to a diffusion of Fe into the W layer (intermixing at the bottom interface) due to a negative enthalpy of mixing while the top CoFeB-MgO interface is more robust upon intermixing (Fe-Mg and Co-Mg have a positive enthalpy of mixing). The enthalpies of mixing of the used elements are summarized in Figure 3-11[161]. Based on this, we illustrate the schematic of the interface configurations for the pristine and irradiated W-CoFeB-MgO films, where the influence on top interface is neglected, as shown in Figure 3-12. Before irradiation, the interface is sharp, though some disorders, terraces separated by atomic steps, arise from sputtering process. After irradiation, the interface disorder is related to intermixing.

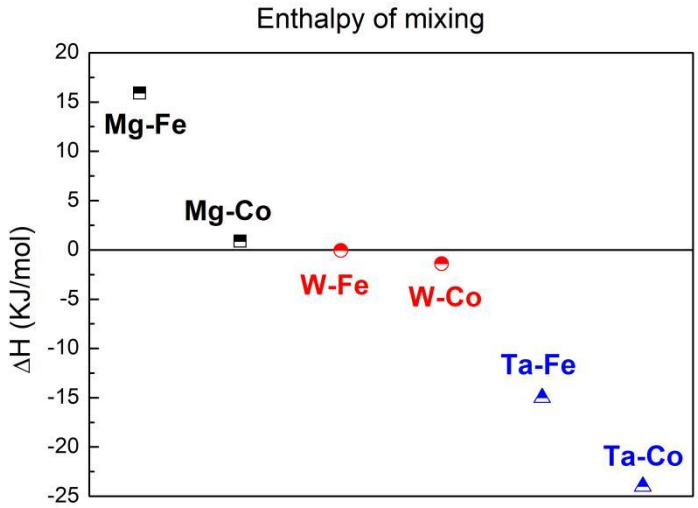

Figure 3-11. Enthalpy of mixing for binary alloys based on W, Ta, Fe, Co and Mg elements. A negative enthalpy of mixing favors intermixing of both elements.

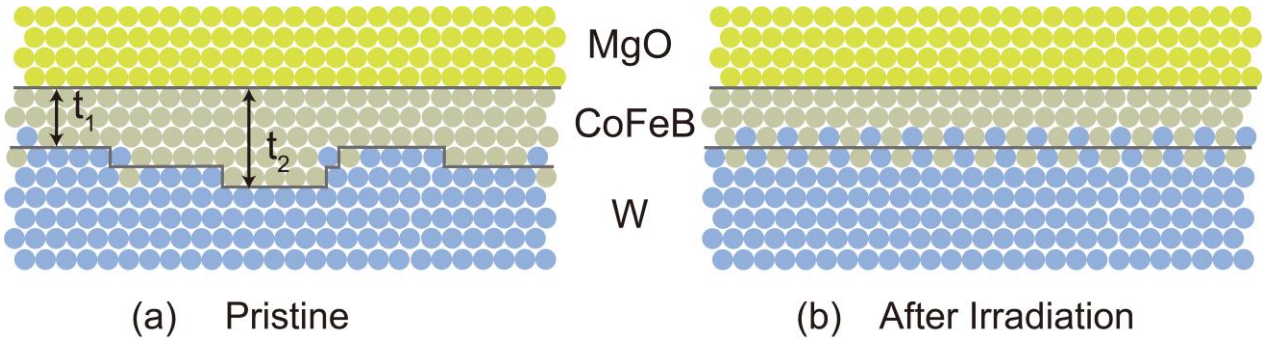

Figure 3-12. Schematic of the interface structure in (a) pristine and (b) irradiated W-CoFeB-MgO films. The dots in yellow represent the MgO layer, while those in gray and blue correspond to the CoFeB and W layers, respectively.

Further than that, as for Ta-Fe alloys, which form a dead layer at the CoFeB-Ta interface [99,162,163], W-Fe alloys are also expected to be paramagnetic for a low concentration of Fe [164]. This explains that the overall magnetization is linearly reduced upon irradiation induced intermixing at the W-CoFeB interface. In addition, the primary source of reduction of interfacial anisotropy upon irradiation is related to the diffusion of Fe from the top CoFeB-MgO interface to the W layer reducing the hybridization between the Fe-3d and O-2p orbitals [94].

Reasons mentioned above also explain the reduction of coercive fields seen in Figure 3-9. Indeed, as the hysteresis loops are square, the magnetization reversal is dominated by the nucleation of reversed domains at some specific locations followed by rapid DW propagation. Thus, the coercive field here corresponds to the nucleation field. As the nucleation fields depend on the anisotropy [165], the reduction of the coercivity field upon irradiation is linked to the reduction of anisotropy.

Due to the large influence of ion irradiation on the interfacial PMA, the domain wall dynamics can be also modulated, which drives lower current induced motion. This effect will be detailed in the chapter 5, which is one of the major contributions of this thesis and help to realize multi-state resistance in a Hall bar cross.

3.2 Modulation of DMI through different methods

As the Dzyaloshinskii-Moriya interaction (DMI) originates from the interfacial spin-orbit coupling, the interface manipulations, including the sharpness by annealing and introducing the disorder by irradiation are considered. In this section, we will focus on the sample of W(4)/$Co_{20}Fe_{60}B_{20}$(*t*)/MgO(2)/Ta(3) (thicknesses in nm), which is deposited on highly resistive Si wafers using dc/rf magnetron sputtering at room temperature.

3.2.1 Dependence of DMI on FM thickness and annealing conditions

In this part, we have determined the DMI values of the as-deposited and annealed W-CoFeB(0.6 nm/1 nm)-MgO samples by Brillouin light scattering (BLS). A linear behavior between the frequency shift and spin wave vector is observed for all the samples, as seen in Figure 3-13. According to the Eq. 2.3, the DMI coefficient can be extracted.

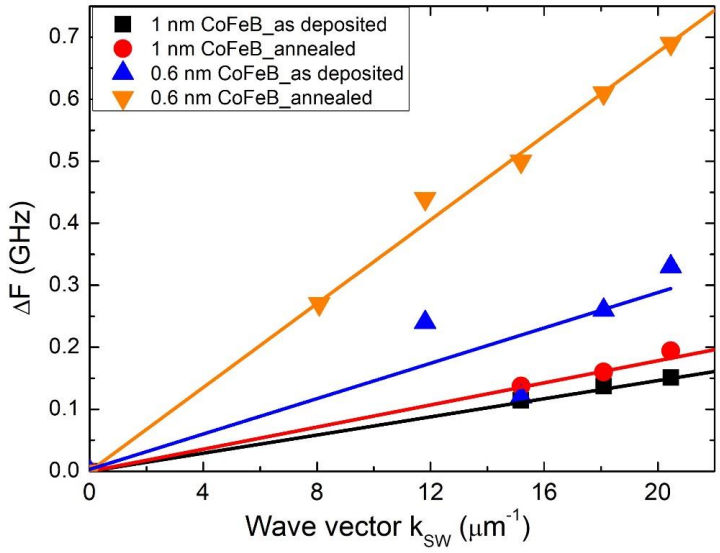

Figure 3-13. Linear fit of the frequency difference ΔF as a function of wave vector k_{SW} for the as-deposited and annealed 1 nm CoFeB samples and 0.6 nm CoFeB samples.

	DMI (mJ/m^2)	
	As deposited	Annealed
1 nm CoFeB	0.072±0.006	0.105±0.003
0.6 nm CoFeB	0.112±0.004	0. 239±0.002

Table 3-4. DMI values obtained from BLS for the as-deposited and annealed 1 nm CoFeB samples and 0.6 nm CoFeB samples.

From Table 3-4, we can observe that thinner ferromagnetic layer and FM crystallization induced by annealing favor higher DMI values. The thickness dependence of DMI evidenced the interfacial origins of it. Based on Ref. [166], if DMI is purely interfacial origin, one expects a variation with thickness according to $D(t) = D_s/t$, where D_s is the interfacial DMI constant. For our as-deposited samples, D_s of 1 nm thick CoFeB is 7.2×10^{-11} mJ/m^3 while 0.6 nm thick is 6.72×10^{-11} mJ/m^3. The variations of D with t are consistent, considering less than 10% error from the measuring and fitting procedures.

As for the annealing effect, the crystallization of CoFe favors sharper interfaces between W/CoFeB and CoFeB/MgO [113], thus enhancing the DMI since interface DMI is expected to be higher for a sharp interface (Figure 3-12 (a)) than for an intermixed interface (Figure 3-12 (b)) since pairwise interaction between 2 magnetic atoms mediated by a heavy metal atom is maximized. Finally, positive DMI constant corresponds to a right-handed magnetic chirality,

in line with previous studies on W-CoFeB-MgO films [167].

3.2.2 Influence of the interfacial disorder induced by irradiation

To further investigate the effects of interface morphology on DMI, we have also studied the influence of interfacial disorder in annealed W/CoFeB(0.6nm)/MgO structures, which exhibit the largest DMI value. The DMI of irradiated samples with 0.6 nm thick CoFeB has been checked by both BLS and magnetic bubble expansion under both perpendicular and in-plane magnetic fields. However, as shown in Figure 3-14 for BLS measurements, non-linear dependence at high *k*-vector k_{SW} for ID= 8×10^{18} ions/m^2 and ID= 20×10^{18} ions/m^2 as well as non-zero intercepts, make it difficult to extract the DMI value. We believe that this is related to an inhomogeneous component arising from disorder, affecting the BLS linewidth in this measurement [75].

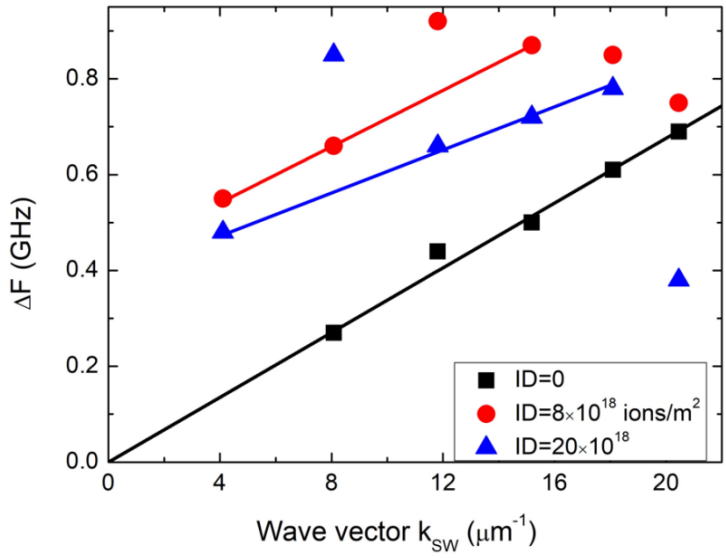

Figure 3-14. Linear fit of the frequency difference ΔF as a function of wave vector k_{SW} for the annealed 0.6 nm CoFeB sample with different fluences.

Then we determine the DMI by using magnetic bubble expansion in the creep regime under both perpendicular and in-plane magnetic fields. As shown in Figure 2-8(a), the radial symmetry is broken due to the presence of an internal effective DMI field [152]. The asymmetric DW velocities for the non-irradiated sample and irradiated one at ID= 4×10^{18}, 8×10^{18} and 1×10^{19}ions/m^2 are shown in Figure 3-15. The DMI constant *D* is then directly calculated from $\mu_0 H_{DMI} = D/M_s\Delta$, where Δ is the DW width defined by $\sqrt{A/K_{eff}}$, *A* is the exchange stiffness constant, taken here as 15 pJ/m [168] and assumed to be a constant for all

the samples. It is worth noting that the values of *D* obtained from DW motion experiments and BLS can often exhibit a certain degree of discrepancy due to the different scales in which these two techniques probe the sample.

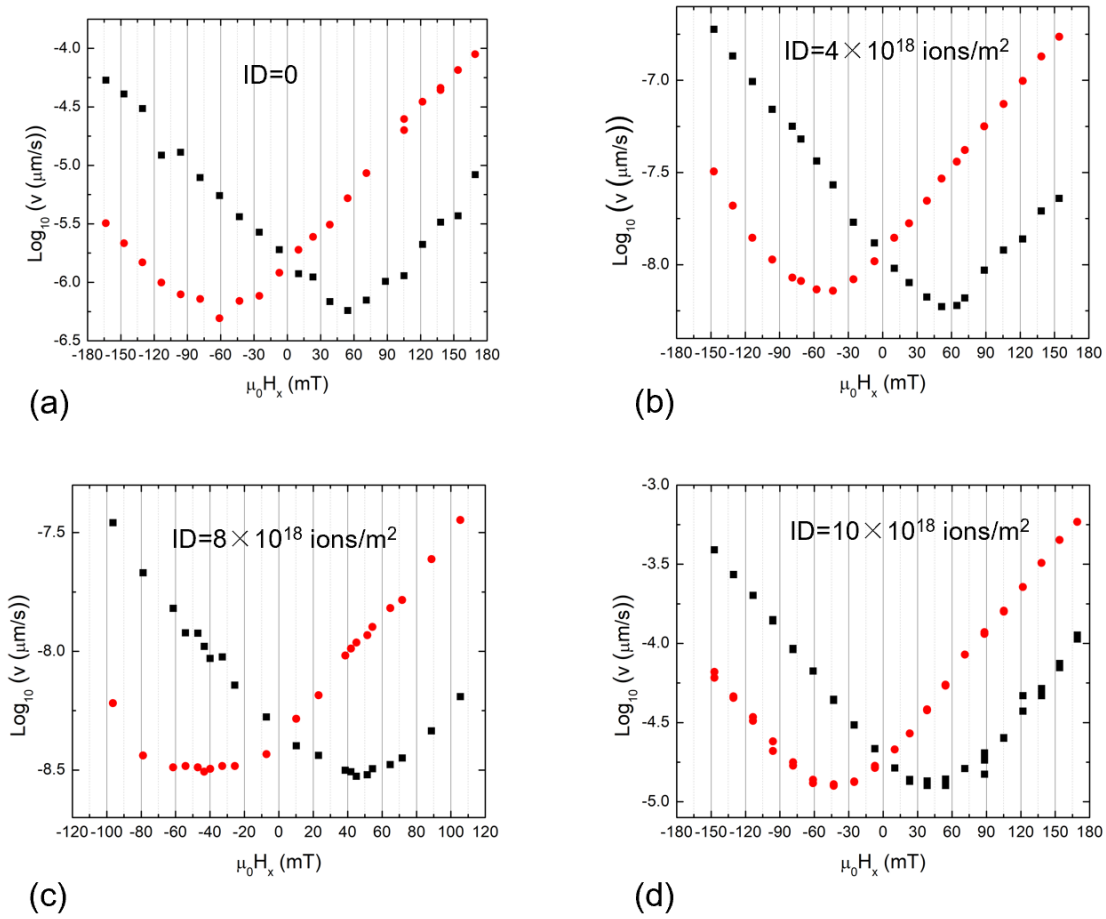

Figure 3-15. DW velocity as a function of $\mu_0 H_x$ for different fluences. A perpendicular field pulse is used to expand the bubble (3.2 mT, 6.4 mT, 3.8 mT and 2.95 mT for ID=0, 4×10^{18}, 8×10^{18} and 10×10^{18} ions/m^2, respectively). The investigated sample structure are annealed SiO_2/W (4)/CoFeB (0.6)/MgO (2)/Ta (3).

The right axes in Figure 3-16 show the DMI value as a function of the fluence up to 1×10^{19} ions/m^2, where a slight linear decrease is observed from 0.30 ± 0.02 to 0.21 ± 0.02 mJ/m^2 upon intermixing. It is shown that the CoFeB/W interface exhibits a positive DMI constant [169,170], while the MgO/CoFeB interface has the opposite sign[120,169]. As we have shown in section 3.1.4, the main effect of ion irradiation is to induce the intermixing at the bottom heavy metal (HM)/ferromagnetic metal (FM) interface. Such intermixing modifies the atomic environment of magnetic and heavy metals atoms at the interface (from interface roughness to intermixing), which can reduce the DMI value [121,170]. In particular, interface DMI is expected to be higher for a rough interface (Figure 3-12 (a)) than for an intermixed interface (Figure 3-12 (b)) since pairwise interaction between 2 magnetic atoms mediated by a heavy metal atom is maximized.

Our results are in line with those of S. Tacchi *et al.* who demonstrated a DMI enhancement with Pt thickness in Pt/CoFeB systems due to cumulative itinerant electron hopping between the atomic spins at the interface and the nonmagnetic atoms in the heavy metal [171]. In our case, the allowing of the W layers reduces the scattering of itinerant electron with non-magnetic atoms in the HM, resulting in an overall reduction of DMI. As a result, the bottom interfacial DMI is weakened, leading to a reduction in the overall still positive DMI.

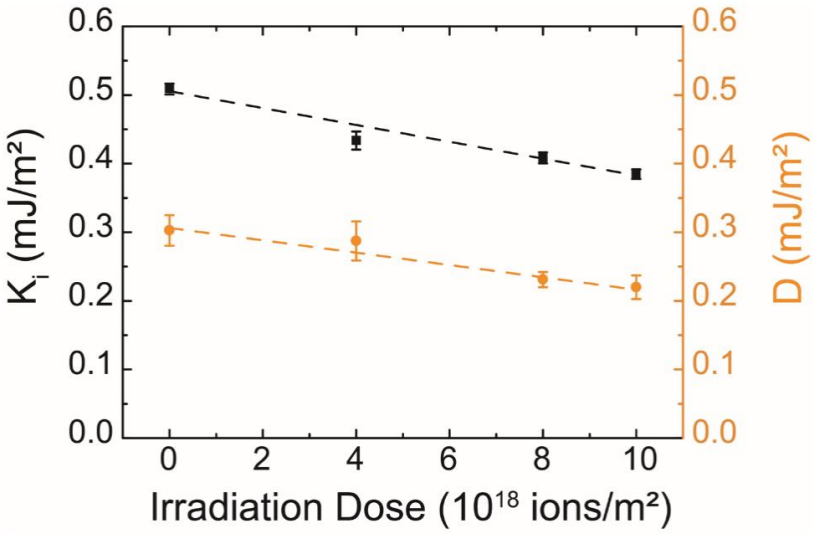

Figure 3-16. Interface anisotropy energy K_i (black squares) and DMI constant (orange dots) as a function of the fluence. The investigated sample structure is annealed SiO_2/W (4)/CoFeB (0.6)/MgO (2)/Ta (3).

For comparison, the interfacial anisotropy K_i and the DMI value with the same units (mJ/m^2) are plotted as a function of the fluence on the same graph as seen in Figure 3-16. First, it can be noticed that both K_i and DMI exhibit a linear decrease *vs* ID with a very similar trend. Considering the slope coefficient β_{K_i} and β_{DMI}, defined as the relative change in K_i and DMI constant over the change in the irradiation fluence, namely $\Delta K_i/\Delta ID$ and $\Delta DMI/\Delta ID$ respectively, we find β_{K_i}=0.0121 mJ/10^{18} ions and β_{DMI}=0.0094 mJ/10^{18} ions. This direct relationship between the relative variation of DMI and interface anisotropy upon intermixing indicates that they have the same origin, the exchange interaction between magnetic and heavy metal atoms is mediated by spin orbit coupling [87,123,172].

3.3 Summary

In this chapter, we have reported the precise modulation of spin-dependent interfacial effects including the magnetic anisotropy and Dzyaloshinskii-Moriya interaction. We have first

shown in agreement with previous studies that thermal annealing in Ta-CoFeB-MgO structures has a strong influence on the PMA through the crystallization process and the interface sharpness. A more original study has focused on interface engineering using ion irradiation. Asymmetric in-plane field-driven domain expansion experiments show that the DMI value is slightly reduced upon irradiation and a direct relationship between DMI and interface anisotropy has been demonstrated.

Chapter 4 Ultra-Efficient Magnetic Switching in W/CoFeB/MgO Structures through SOT

In this chapter we study the efficient SOT induced switching in a W/$Co_{20}Fe_{60}B_{20}$/MgO device with PMA and explore the effect of different physical parameters, such as DW depinning field, DMI strength and spin Hall angle (SHA) on the switching process.

The studied stack structures are W(4)/$Co_{20}Fe_{60}B_{20}$(t)/MgO(2)/Ta(3) (thicknesses in nm), which was deposited on highly resistive Si wafers using dc/rf magnetron sputtering at room temperature. After deposition, the sample was annealed at 400 ℃ for two hours to obtain a good PMA. The multilayer films were patterned into standard Hall bars (length of 130 μm and width of 20 μm) using optical lithography and dry etching for SOT switching and second harmonic measurements. Cr(10 nm)/Au(100 nm) metal stacks were deposited as contacts for electrical measurements. The SOT switching and second harmonic measurement were all performed in VersaLab. For the switching measurement, ten microseconds current pulse were applied sweeping from 10 mA to -10 mA. The magnetic hysteresis loop was probed by the polar magneto-optical Kerr effect (P-MOKE) magnetometry, as well as the vibrating sample magnetometry (VSM) to obtain the saturated magnetization and anisotropy field. All measurements were conducted at room temperature.

4.1 Ultra-low switching current in perpendicularly magnetized sample

We firstly explored the sample with 0.6 nm thick CoFeB, which exhibits high PMA (K_{eff} =3.95×10^5 J/m^3) and DMI (0.239 mJ/m^2 by BLS and 0.32 mJ/m^2 by DW expansion). Figure 4-1(a) shows the current induced SOT switching under different assisting in-plane magnetic field. When I increase the applied current to a threshold value, the anomalous Hall resistance shows a jump, indicating the magnetic switching of the CoFeB layer. The critical switching currents are symmetric for both switching directions. When the in-plane magnetic field changes from positive to negative direction, the magnetic state *vs.* the current direction is also reversed. The phase diagram of the critical switching current density *vs*. the strength of the in-plane magnetic field is summarized in Figure 4-1(b). Obviously, when a larger in-plane magnetic field is applied, a smaller critical switching current is required, which is due to the symmetry breaking caused by the assisting in-plane magnetic field. Larger in-plane field promotes the tilting of the magnetization to the longitudinal direction, for which a smaller

current can lead to the magnetic switching. When a 100 mT in-plane field is applied, the switching current density is measured to be 3.03×10^6 A/cm^2, considering the resistivity of CoFeB (170 μΩ·cm) and W (210 μΩ·cm)[41,173].

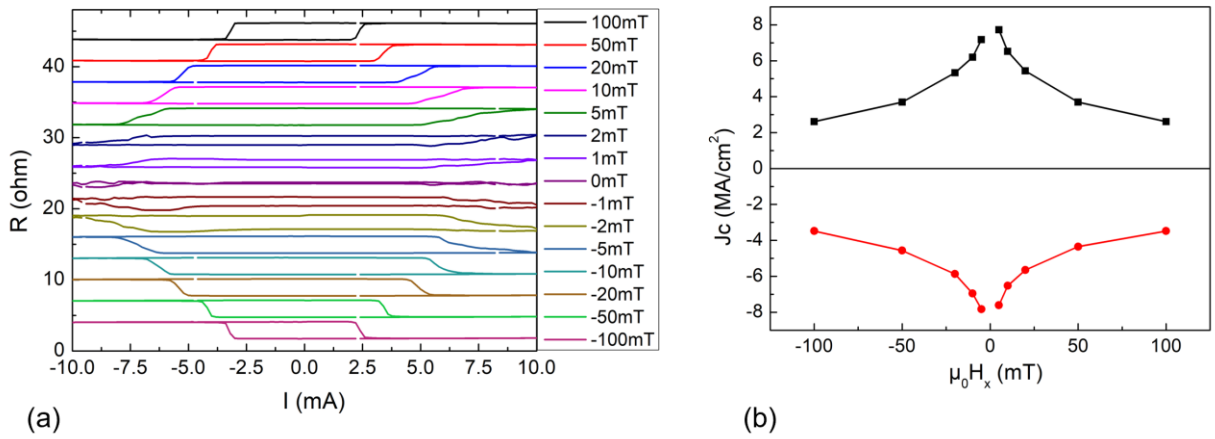

Figure 4-1 (a) The current induced SOT switching under different in-plane magnetic field measured in VersaLab. (b) The phase diagram of critical current density and assistant in-plane magnetic field. The investigated sample is the annealed SiO_2/W (4)/CoFeB (0.6)/MgO (2)/Ta (3).

Then the sample with 1 nm thick CoFeB is studied. The phase diagram of the critical switching current density *vs*. the strength of the in-plane magnetic field is summarized in Figure 4-2. Similarly, the critical switching current density increases with the decrease of in-plane field. When the in-plane field decreases to 4 mT, the current required for the magnetic switching incrases substantially. As the in-plane field further decreases, the magnetization cannot be fully switched. The critical switching current density could be as low as 1.15×10^6 A/cm^2 when a 60 mT in-plane field is applied. This critical current density is much smaller than those obtained in other structures with strong PMA such as: Ta/$Co_{40}Fe_{40}B_{20}$[41,46,174], Pt/Co[40], and W/Hf/$Co_{40}Fe_{40}B_{20}$[175].

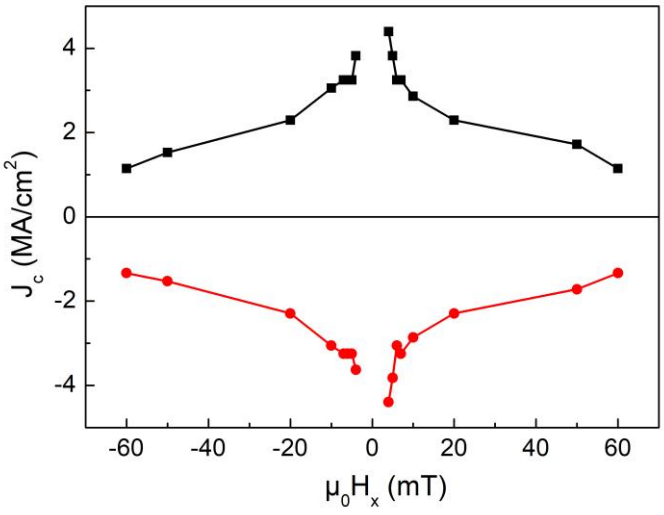

Figure 4-2 Phase diagram of critical current density versus assistant in-plane magnetic field for the sample with 1 nm thick CoFeB.

To get a deeper understanding of this ultra-low current density, the SOT switching process in the Hall bar device with 1 nm thick CoFeB has been observed by a high-resolution Kerr microscope. In this experiment, a permanent in-plane field of 10 mT is applied. After saturating the sample in one direction with a large perpendicular magnetic field, successive current pulses are applied along the longitudinal direction. Figure 4-3 (a-h) shows a series of Kerr image presenting the magnetic switching process induced by current pulses. When the current is reversed, a DW nucleates from the other edge and propagates in the opposite direction, as shown in Figure 4-3 (i-p). The magnitude of each current pulse is 3.8×10^6 A/cm^2 with a duration of 1 ms. We can see that the switching starts by a DW nucleation from one side of the sample and propagates towards the other side, leading to the complete switching, except for one small part in the corner. The DW nucleation in the edge may be eased by a reduction of the anisotropy due to some unavoidable damages during the device fabrication [176]. By changing the magnitude and duration of the applied current pulse, we find that although the DW nucleation is very easy even for a small current in this sample, the DW propagation is observable only when the current density reaches 3×10^6 A/cm^2. This critical current corresponds to the switching current by VersaLab under an in-plane field of 10 mT. This consistency suggests that the determinant factor for the SOT induced switching in our sample is DW propagation rather than the nucleation of magnetic DW.

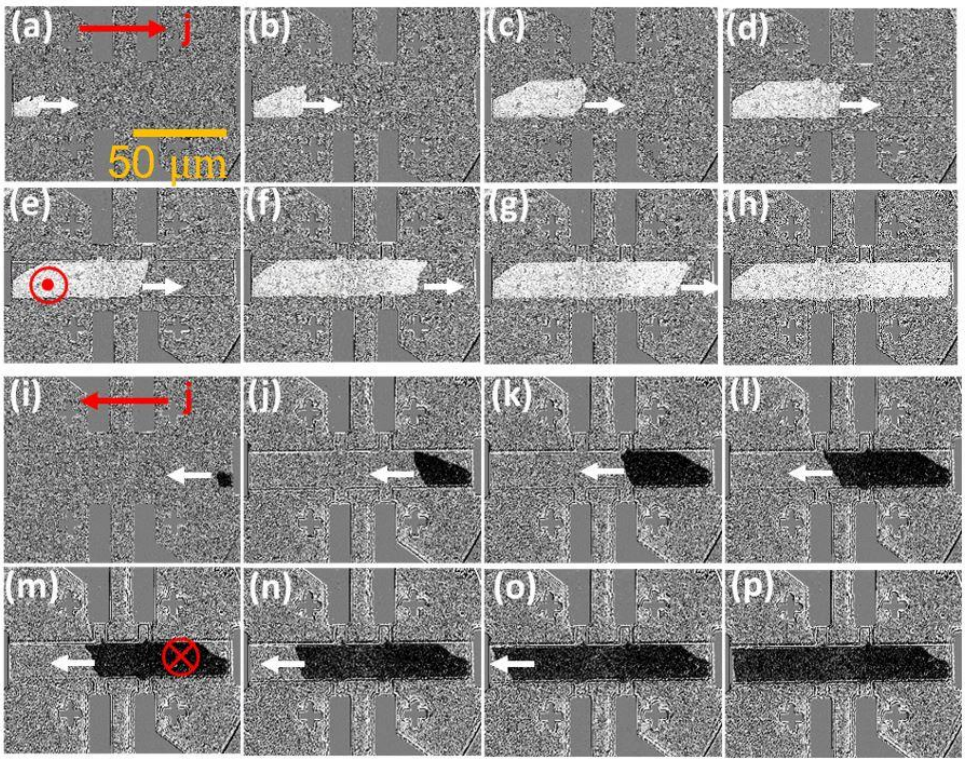

Figure 4-3. Kerr images showing the SOT induced magnetic switching process of the device under an in-plane magnetic field. (a-h) The SOT induced switching process under the positive current pulse at 10 mT in-plane magnetic field. (Hall bar length of 130 μm and width of 20 μm). Between each image, a current pulse is applied. In this example, the current density applied in the W layer is 3.8×10^6 A/cm^2 and the duration is 1 ms. (i-p) The SOT switching process under a negative current pulse and a 10 mT in-plane magnetic field. The investigated sample is the annealed SiO_2/W (4)/CoFeB (1)/MgO (2)/Ta (3).

In the next three sections, we will discuss the influence factors on the ultra-efficient SOT switching.

4.2 Dependence of SOT switching on depinning field

To investigate the ultra-low switching current, DW dynamics ought to be carefully studied. The DW velocity can be determined by measuring the average displacement of bubble-like domains under perpendicular magnetic field pulses H_z with pulse duration ranging from 3 μs to 10s. All measurements are conducted at room temperature. The DW velocity plotted in logarithmic scale in Figure 4-5 is given by the universal creep law according to Eq. (1.10) to (1.12). This thermally activated regime describes the collective pinning of the DW by structural defects presented in the ultra-thin films. For high fields, too many nucleation events occur, making it difficult to measure the DW velocity.

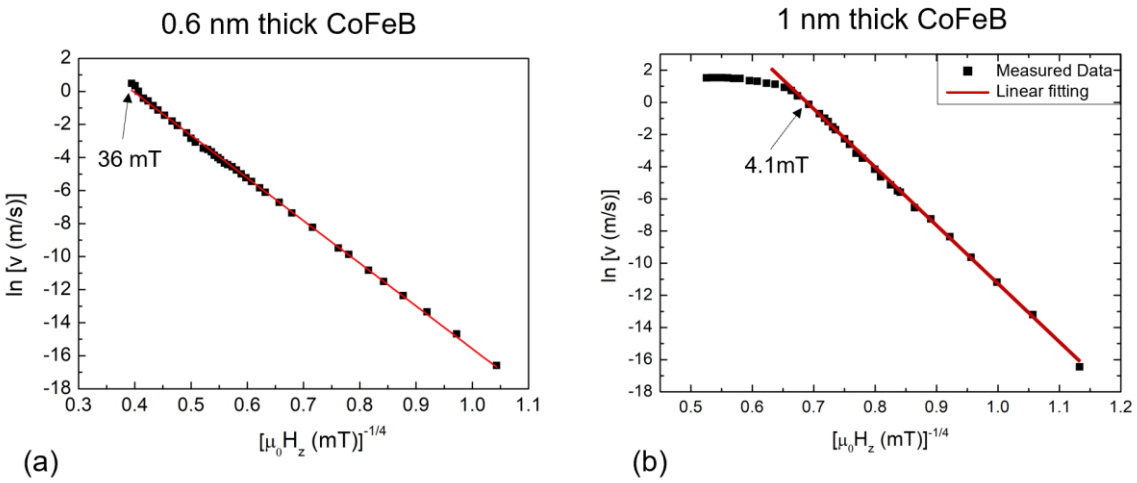

Figure 4-4. The DW motion velocity induced by out-plane magnetic fields (dot) measured by Kerr microscopy and fitting results with creep law (line) for 0.6 nm (a) and 1 nm (b) thick CoFeB.

Compared with Figure 4-4 (a) and (b), the DW motion leaves the creep regime when the applied perpendicular field is larger than 4.1 mT for 1 nm thick CoFeB, while the 0.6 nm thick CoFeB sample still in the creep region with the applied field at 36 mT. The intermediate depinning regime above the creep regime for 0.6 nm thick CoFeB is very limited since it is not possible to measure DW velocity at very high fields due to nucleation events. But it can be fitted by a depinning law which will be described in more detail in the next chapter.

Since the intrinsic DW depinning field H_{dep} can be regarded as an indicator of the strength of the intrinsic pinning effect, 4.1 mT for 1 nm thick CoFeB means a much smoother interface (less pinning events) compared with 0.6 nm. In addition, 4.1 mT of depinning field is also very low compared with that of other materials such as Co[177], which is consistent with the statement that CoFeB is an ultra-soft material[178,179]. This low depinning field is one of the reasons for the efficient magnetic switching because it allows for the DW propagation under a weak magnetic field or SOT current.

4.3 Dependence of SOT switching on DMI

According to the literatures [180,181], the DW nucleation sites are indeed determined by the relative direction of in-plane field and DMI chirality. The symmetrical DW nucleation and propagation with the opposite in-plane field are shown in Figure 4-3 indicating an influence of DMI on SOT switching.

As shown in Table 3-3, the DMI of annealed 0.6 nm CoFeB measured by BLS is much larger than that of 1 nm CoFeB. We further confirm the DMI values by asymmetric DW propagation with an in-plane field [132]. We show the asymmetric DW velocity in Figure 3-15 (a) for 0.6

nm thick CoFeB and in Figure 4-5 for 1 nm thick CoFeB.

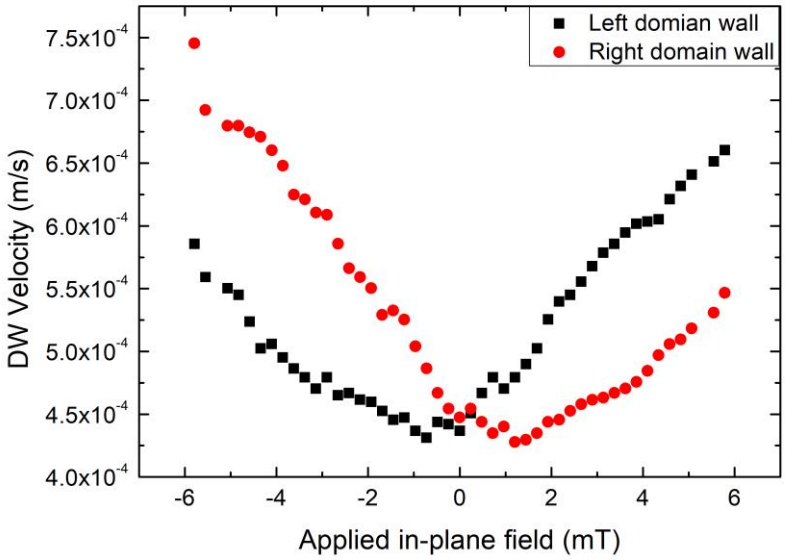

Figure 4-5. DW velocity induced by an out of plane field in the creep regime as a function of the in-plane applied field. In this measurement, the magnitude of the out of plane field is fixed at 3.2mT while the in-plane field sweeps. The investigated sample is the annealed SiO_2/W (4)/CoFeB (1)/MgO (2)/Ta (3).

For the 1 nm thick CoFeB, the minimum DW propagation velocity is observed when the perpendicular field remains constant while an in-plane field is around 1 ± 0.1 mT. According to the DW propagation mechanism [152], this field approximately equals to the effective DMI field $\mu_0 H_{DMI}$ and the DMI parameters can be calculated as $D = \mu_0 H_{DMI} M_s \Delta = 0.013\ \mathrm{mJ}/m^2$. For 0.6 nm thick CoFeB, $D = 0.3\ \mathrm{mJ}/m^2$ by this method. As we have mentioned above, values of D obtained from DW motion experiments and BLS always exhibit a certain degree of discrepancy.

No matter the means of obtaining the DMI value, the value of D for 1 nm thick CoFeB is small and such a small value is responsible for the efficient SOT switching. In fact, sample with small DMI induces a DW structure intermediate between a pure Bloch wall (BW) and a pure Néel wall (NW). As shown by the micromagnetic simulation in Figure 4-6, when an in-plane field is applied, the DW on one side is closer to a BW and closer to a NW on the other side (Figure 4-6 (b)). Since the SOT is more efficient for the NW, the DW on the right side propagates more easily. On the contrary, if the current direction (thus the switching direction) is changed (Figure 4-6 (c)), the DW in the left side propagates more easily. This analysis can explain why the DW nucleates and propagates from the two different ends of the microwire during the two different switching processes. In addition, the DW on the one side is closer to the Néel configuration when the DMI effective field is parallel to the external

in-plane field. In this case, the DW motion is facilitated and therefore, the weak DMI in the sample with 1 nm thick CoFeB favors a high efficient SOT switching.

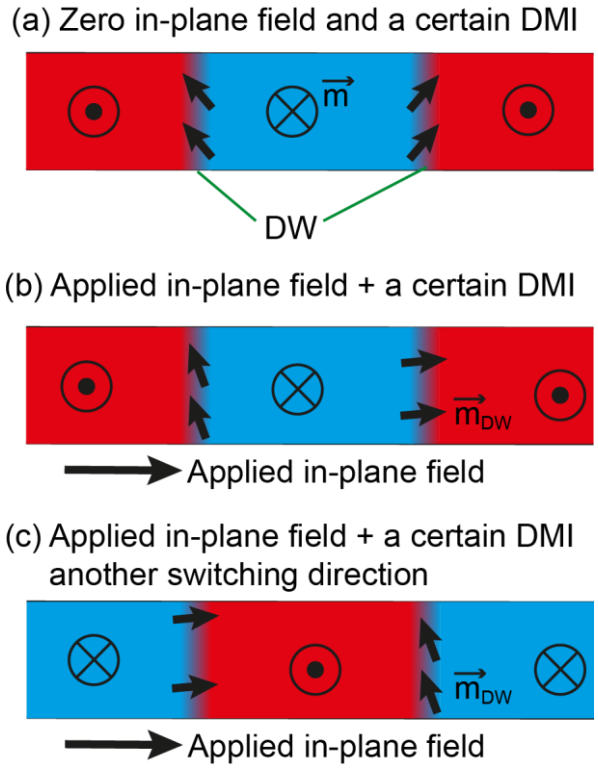

Figure 4-6. DW configuration in different cases. (a) with a small DMI and zero external in-planed field; (b) with a small DMI (i.e. < 0.1 mJ/m^2) and a certain external in-planed field; (c) with a small DMI and a certain external in-planed field, but opposite initial magnetization compared with that of (b).

Note that this conclusion is not in contradictory with the literatures[182,183] that DMI increases the switching current. In their case, a large DMI exists. When a spin torque is applied, the DMI strongly promotes non-uniform magnetic textures, making overall spin torque less efficient. In addition, if DMI is strong enough, the maze domain structure appears since this demagnetizing state is more energetically advantageous. In this case, it is very difficult to get a completely reversed state.

4.4 Influence of spin Hall angle on SOT switching

The generated spin current is proportional to the SHA of the heavy metal. A large SHA layer is beneficial for efficient SOT induced switching according to Eq. (1.9). To quantify the SHA of the W layer in the studied device, the second harmonic method has been performed on the sample with 1 nm thick CoFeB, through which both the field-like torque and the damping-like torque can be obtained. Figure 4-7 (a) shows the structure of the second harmonic measurement, where a small sinusoidal current $I = I_{ac}\sin(2\pi ft)$ with peak value $I_{ac} =$

1.4 mA and frequency $f = 133.33$ Hz is applied along the path. The first and second harmonic signals are measured by a lock-in technique where the in-plane external field is applied along the longitudinal (transverse) direction. The damping-like (ΔH_x) and field-like (ΔH_y) effective fields can be obtained by the following equations[45]: $\Delta H_{x(y)} = -2\frac{\partial V_{2\omega}}{\partial H_{x(y)}}/\frac{\partial^2 V_{\omega}}{\partial H_{x(y)}^2}$. Figure 4-7 (b, c) show the measured first and second harmonic signal, which could be well fitted by the parabolic and linear function, respectively. In the inset is the result for the whole range of magnetic field. The effective damping-like torque efficiency defined by $\frac{\Delta H_x}{J_{ac}}$ is about 0.53 mT/(10^6 A/cm^2), which is obtained by the linear fitting of the current as a function of applied magnetic field shown in Figure 4-7 (d). The SHA can be calculated from the damping-like field by $\theta_{SHA} = -\frac{2|e|M_s t_F}{\hbar} \times \frac{\Delta H_x}{J_{ac}}$. The SHA is found to be about -0.164, larger than that of Ta (<0.12)[184,185,186] in the same structure configuration. Considering the spin current density is inversely proportional to SHA, this relatively high angle is favorable to the efficient SOT-induced switching.

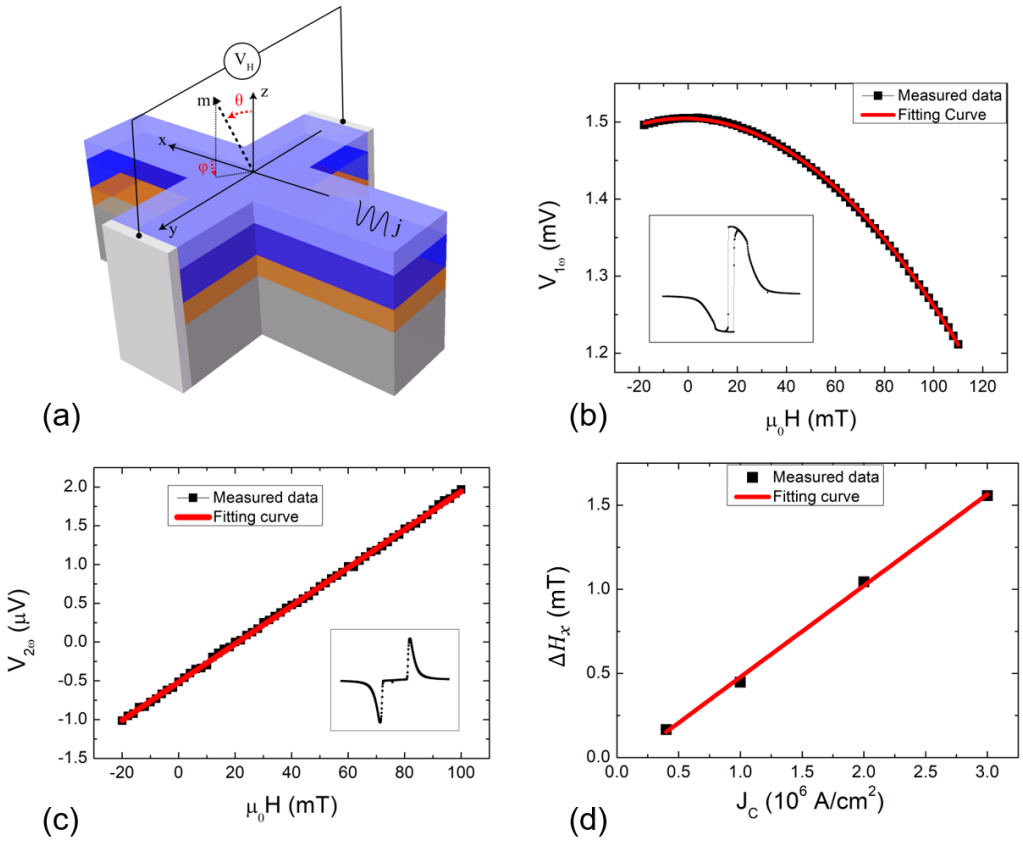

Figure 4-7. (a) Schematic illustration of Hall bar device and the measurement layout of the second harmonic method. (b, c) The measured first and second harmonic signal (dot) and the fit curve (line), inset is the signal in large magnetic field range. (d) The calculated effective damping-like field versus current density.

4.5 Summary

In this chapter, we have systematically studied the SOT switching in perpendicular W/$Co_{20}Fe_{60}B_{20}$/MgO structures. By choosing a CoFeB thickness of 1 nm, the switching current density can be as low as 1.15×10^6 A/cm^2 with an assisting in-plane magnetic field, much lower than other heavy metal systems (Pt, Ta). The SOT induced switching process is observed by Kerr microscopy, showing that magnetic switching is dominated by the DW nucleation and propagation. A series of experiments have been performed to understand the ultra-efficient SOT-induced switching. We have demonstrated that the ultra-efficient SOT-induced magnetic switching in the W/CoFeB (1nm)/MgO is due to the combination of high SHA in the tungsten and the low DW depinning field. The weak DMI is also helpful for the efficient switching as the SOT induced DW propagation from one side is favored when the effective DMI field is parallel to the in-plane field.

Chapter 5 Modulation of SOT Magnetic Switching in W/CoFeB/MgO Structures by Ion Irradiation

In the previous chapter, we have evidenced ultra-efficient SOT switching in W(4 nm)/$Co_{20}Fe_{60}B_{20}$ (1 nm)/ MgO(2 nm)/Ta(3 nm) structures, due to the combination of high SHA, low DW depinning field and small DMI. As mentioned in the chapter 3, ion irradiation is a valuable method to modulate the spin dependent interfacial effects, which could help for the enhancement of SOT switching efficiency and provide new functions for spintronic devices. In this chapter, I investigate this approach by using He^+ ion irradiation. In order to illustrate the modulation of interfacial effects with large window, the samples W(4 nm)/$Co_{20}Fe_{60}B_{20}$(0.6 nm)/MgO(2 nm)/Ta(3 nm) have been used, which present strong interfacial PMA and DMI.

5.1 Enhancement of DW velocity through irradiation

As shown previously, annealed W/$Co_{20}Fe_{60}B_{20}$(0.6 nm)/MgO structure show much stronger effective PMA and large DMI values than 1nm thick CoFeB layer. In order to investigate the influence of interface modulations induced by ion irradiation on the SOT switching, we first perform measurements of domain wall motion by using Kerr microscopy.

Fluences from 2×10^{18} to 3×10^{19} ions/m^2 of He^+ ions are used. However, up to 1×10^{19} ions/m^2, the interfacial PMA becomes too close to the in-plane transition to get a stable magnetic domain configuration and it is not possible to measure DW dynamics, as shown in Figure 5-1.

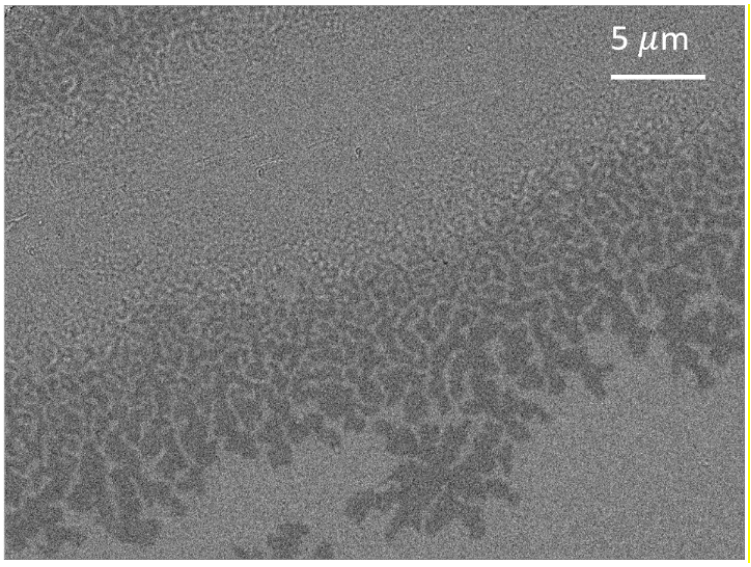

Figure 5-1. Differential-mode Kerr microscope image recorded after 10 seconds' waiting, indicating a spontaneous demagnetized state for the annealed W(4 nm)/$Co_{20}Fe_{60}B_{20}$(0.6 nm)/MgO(2 nm)/Ta(3 nm) sample after irradiation at 2×10^{19} ions/m^2.

The domain wall velocity is determined in the bubble-like domains under perpendicular magnetic field pulses H_z. All measurements are conducted at room temperature. According to the creep law, the linear behaviour of the ln(v) vs. $\mu_0 H_z^{1/4}$ is presented in Figure 5-2 with different ion irradiation fluences (ID). A strong increase of the DW velocity in the creep regime upon He^+ irradiation is observed.

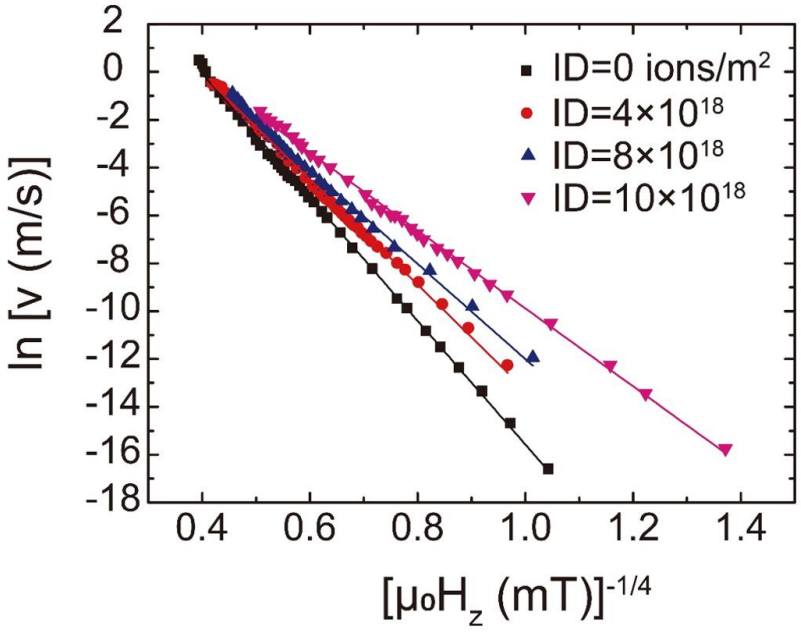

Figure 5-2 DW velocity as a function of perpendicular magnetic field $H_z^{-1/4}$ for different fluences. The sample is the annealed W(4 nm)/$Co_{20}Fe_{60}B_{20}$(0.6 nm)/MgO(2 nm)/Ta(3 nm).

Surprisingly, the result of the increasing DW velocity is opposite to that of Ta-CoFeB-MgO systems [73], where irradiation induced intermixing leads to a strong reduction of DW velocity due to an increase of the pinning potential. To provide a deeper understanding of the increase of DW velocity in the creep regime, as illustrated in Figure 5-3, we plot

$$S = \left(\frac{U_C}{k_B T}\right) H_{dep}^{\mu}, \tag{5.1}$$

as a function of fluence, which represents the slope of the linear variation as seen in Figure 5-2. The slope *S* shows a linear reduction as a function of the fluence, which is consistent with a progressive increase of DW velocity at a given field. H_{dep} is usually estimated by determining the intersection between the creep and the intermediate depinning regime using a fitting procedure [68,74]. We apply this procedure (see Figure 5-4 (a)) here but take into account

that the intermediate depinning regime above the creep regime is very limited since it is not possible to measure DW velocity at very high fields due to nucleation events. As seen in Figure 5-4 (b), a strong reduction of H_{dep} from 40 to 20 mT is observed upon irradiation, indicating a decrease of the pinning potential strength. As described in Ref [73], H_{dep} includes a dependence on magnetic anisotropy K_{eff}, saturation magnetization M_s and the pinning density n_i through

$$H_{dep} \propto \frac{\sqrt{K_{eff}} n_i^{\frac{2}{3}}}{M_s}. \tag{5.2}$$

From the values of M_s and K_{eff}, which both decrease upon irradiation, we can deduce that the reduction of H_{dep} by a factor of 2 is mainly driven by the reduction of the pinning density n_i since the ratio $K_{eff}^{\frac{1}{2}}/M_s$ is nearly constant from ID= 0 to ID=10×10^{18} ions/m^2. In addition, by considering the value of H_{dep} in Eq. (5.1), the reduction of the parameter S is also found to be mainly driven by the reduction of H_{dep} since $\frac{U_C}{k_B T}$ is nearly constant (varying from 15 to 12).

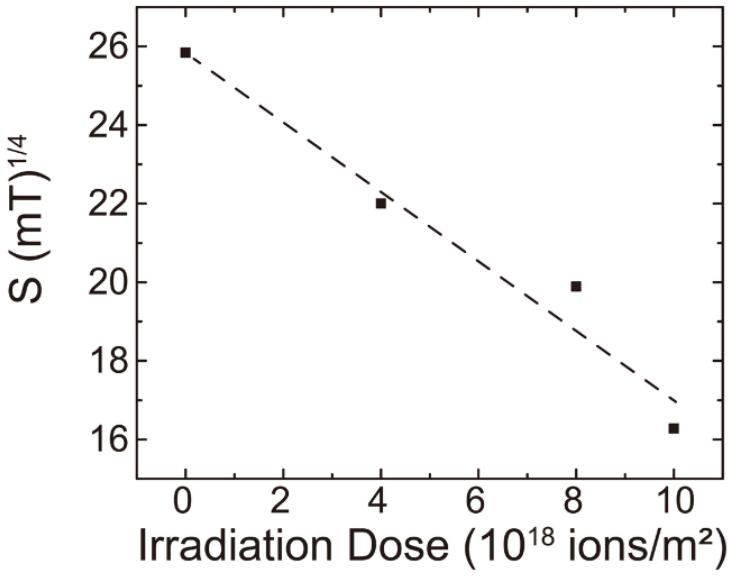

Figure 5-3 Coefficient *S* (linear slope of the DW velocity vs field seen in Figure 4-2(b)) as a function of the irradiation fluences.

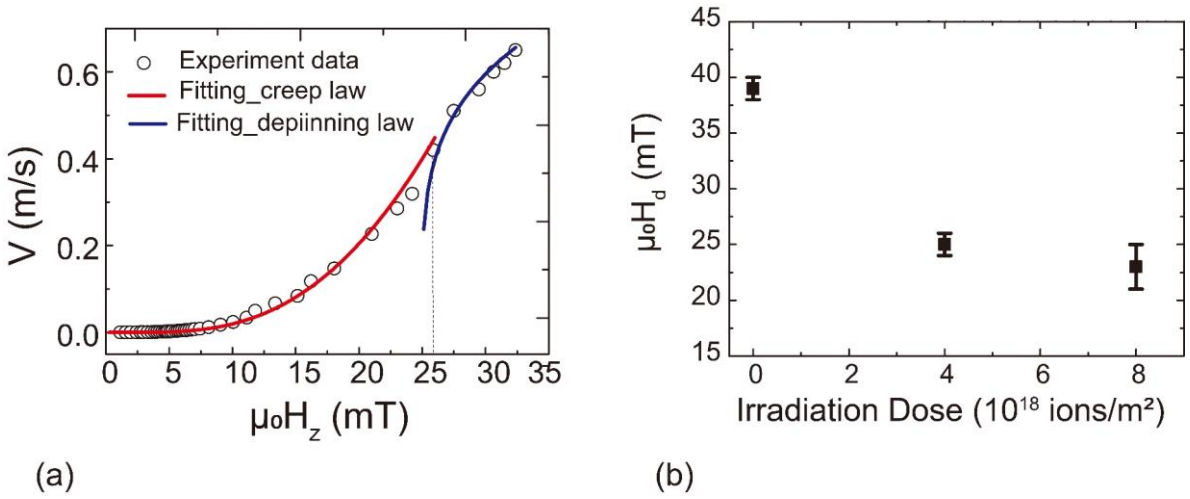

Figure 5-4 (a) H_{dep} fitting procedure described in Ref [74], (b) the value of H_{dep} as a function of irradiation fluence.

The increase of domain wall velocity is correlated to a reduction of the density of the pinning centres in our samples driven by ion irradiation induced intermixing. This is opposite to the Ta-CoFeB (1nm)-MgO case where irradiation induced intermixing leads to a strong increase of DW pinning. In order to explain this result, we first note that the DW velocity in the non-irradiated Ta-CoFeB (1nm)-MgO system [73] is 1 to 2 orders of magnitude larger than that of W-CoFeB (0.6nm)-MgO at a given field for similar K_{eff} and M_s values. This is related to a higher pinning strength in pristine W-CoFeB (0.6nm)-MgO structures as illustrated by the different H_{dep} values (H_{dep} =8 mT [73] and H_{dep} =40 mT for Ta-CoFeB-MgO and W-CoFeB-MgO systems, respectively). Beyond the fact that a 0.6nm thick magnetic layer is more disordered than a 1nm thick layer, our further assumption is that since the W-CoFeB interface is less sensitive to intermixing than the Ta-CoFeB interface (see enthalpy of mixing in Figure 3-11), the interface disorder may be dominated by roughness in pristine W-CoFeB-MgO structures (flat terraces separated by atomic steps at the W-CoFeB interface) and by intermixing in thicker Ta-CoFeB-MgO structures. Since the strength of pinning is higher for atomic steps [187], this can explain the difference in domain wall velocity with respect to the pristine films. As sketched in Figure 3-12, upon irradiation, intermixing is induced at the W-CoFeB interface, erasing the atomic steps and smoothening the interface. This leads to a reduction of the pinning consistent with the increase of DW velocity.

5.2 Irradiation induced high-efficient SOT magnetization switching

We then investigate the magnetization switching of irradiated samples induced by spin-orbit torque. The studied samples are the patterned Hall bars of Type A, B, C and D as mentioned

in the Chapter 2.1.4, with the CoFeB thickness of 0.6 nm. All samples are pre-annealed at 400°C for 2 hours. The applied irradiation fluences are 4×10^{18}, 8×10^{18}, 1×10^{19} and 1.5×10^{19} ions/m^2. For the Type A and B, where only the Hall cross(es) is (are) irradiated, the interesting multi-level resistances are presented and will be discussed in detail in the next section. This section will focus on the fully irradiated Hall devices, namely Type C.

The SOT induced switching under different in-plane magnetic fields are measured using a VersaLab system. Ten milliseconds current pulses are applied ranging from 10 mA to −10 mA. The switching properties for the sample irradiated at 4×10^{18} ions/m^2 are shown in Figure 5-5. When the in-plane field decreases to 2 mT, the current required for the magnetic switching increases substantially. As the in-plane field further decreases, the magnetization cannot be fully switched.

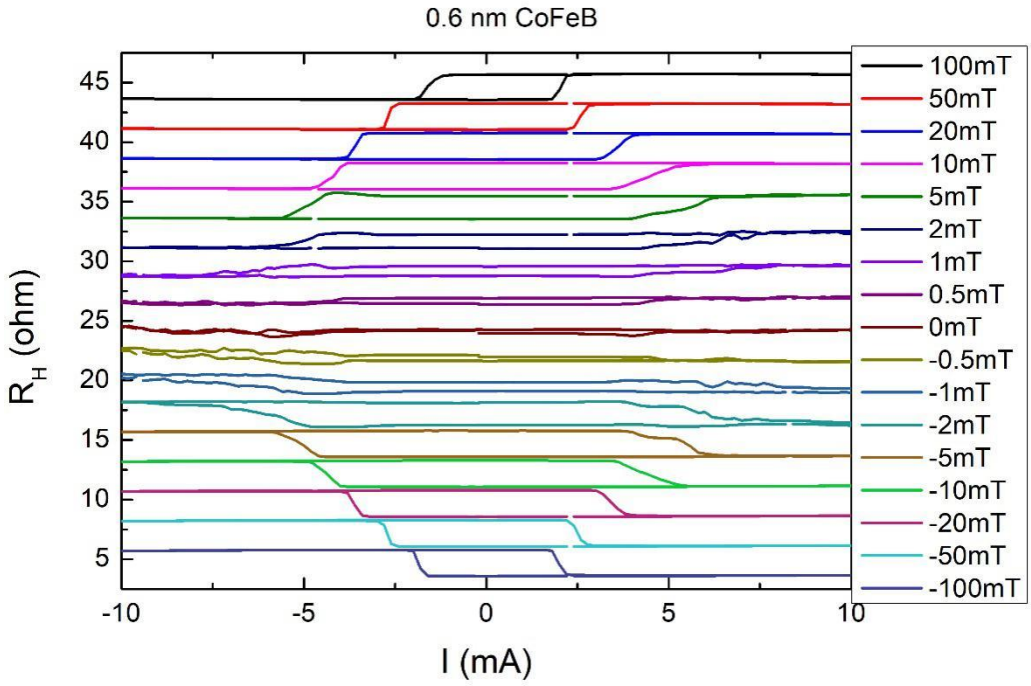

Figure 5-5. The current induced SOT switching under different in-plane magnetic fields measured in using a VersaLab system. The investigated sample is the annealed SiO_2/W (4)/CoFeB (0.6)/MgO (2)/Ta (3).

The phase diagram of the critical switching current density versus the strength of the in-plane magnetic field is summarized in Figure 5-6. The higher the fluence applied to the sample, the smaller the critical switching current is. For the non-irradiated sample, the critical switching current density is 3.03 MA/cm^2 under 100 mT in-plane magnetic field, while that of the sample irradiated at 10×10^{18} ions/m^2 could reach 0.98 MA/cm^2. We have seen in chapter 4, that SOT switching is characterized by DW nucleation followed by DW motion. The decrease

of the critical current density can be explained by the following reasons. First, according to the analysis in section 3.1.4, perpendicular magnetic anisotropy is reduced with the increasing *ID*, so that a smaller current is required to induced DW nucleation. Second, since irradiation tends to smooth the W/CoFeB interface, rapid DW propagation can occur. Third, based on the analysis in section 4.3, a large DMI promotes strongly non-uniform magnetic textures, which make overall spin torques less efficient [188,189]. The variation of DMI from 0.3 to 0.2 mJ/m^2 for the non-irradiated and *ID*=10×10^{18} ions/m^2 irradiated samples could be one of the reasons for the more efficient switching.

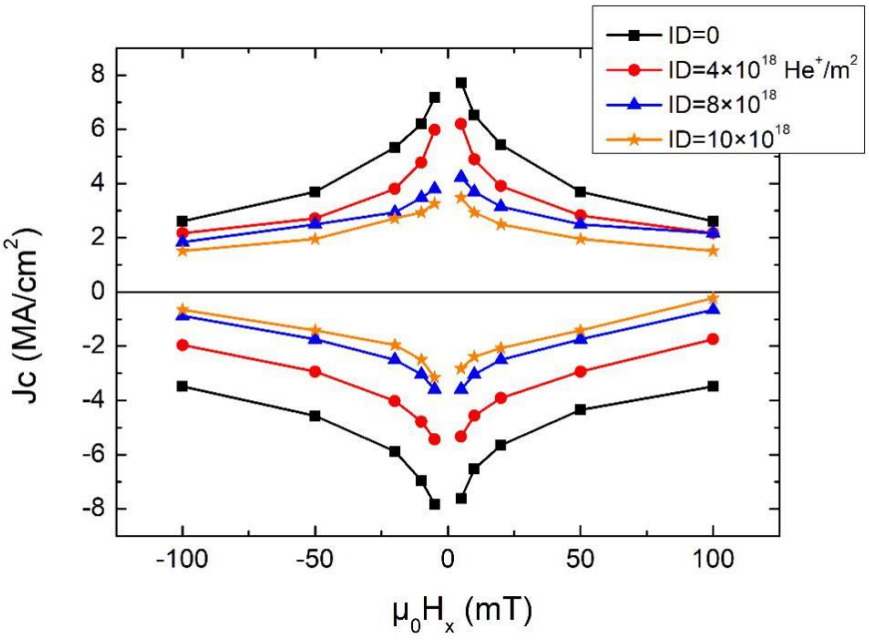

Figure 5-6. Phase diagram of critical current density and assistant in-plane magnetic field versus magnetic state. The investigated sample is the annealed SiO_2/W (4)/CoFeB (0.6)/MgO (2)/Ta (3).

5.3 Spin orbit torque driven multi-state resistance in irradiated Hall cross

In this part, we will present the switching process in the partially irradiated Hall bars, i.e. Type A and B. In Figure 5-7, 5-8 and 5-9, SOT induced magnetization switching under ±50 mT in-plane magnetic fields for Type A, B and C is presented. We can observe that Type A and B have the same loop shape, indicating that the ion irradiation of one Hall cross does not affect the measurement of the other one. On the other hand, for Type A and B, multi-level resistance occurs at high irradiation fluence, while the fully irradiated sample of Type C does not. To illustrate this behavior, we will focus on the analysis of sample of Type B irradiated at a fluence of 1×10^{19} ions/m^2 as shown in Figure 5-10.

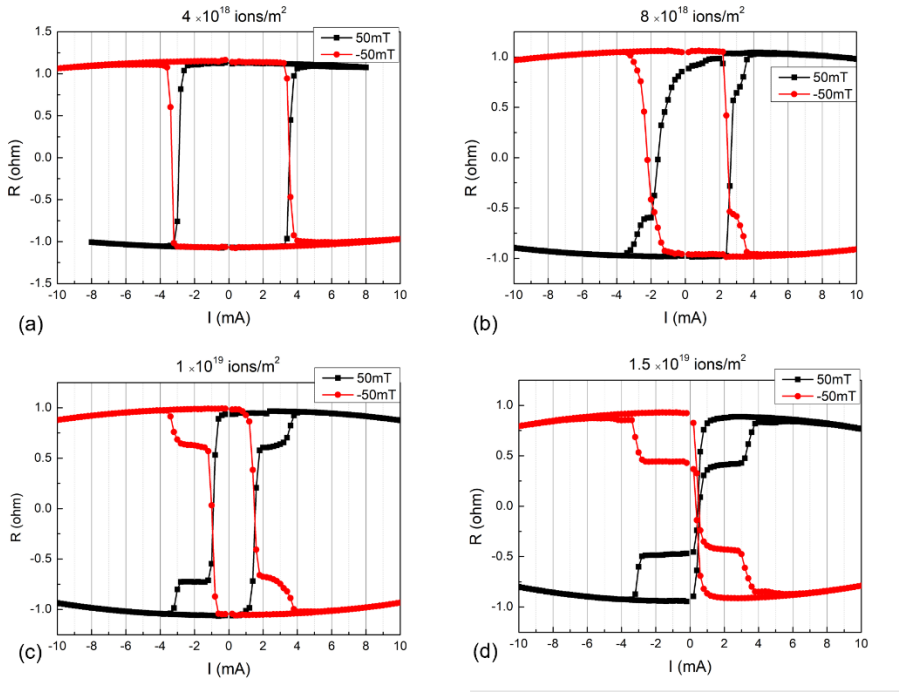

Figure 5-7. Anomalous resistance loops measured under ±50 mT in-plane fields by sweeping the pulse current for the Type A sample irradiated at (a) 4×10^{18} ions/m^2, (b) 8×10^{18} ions/m^2, (c) 1×10^{19} ions/m^2 and (d) 1.5×10^{19} ions/m^2.

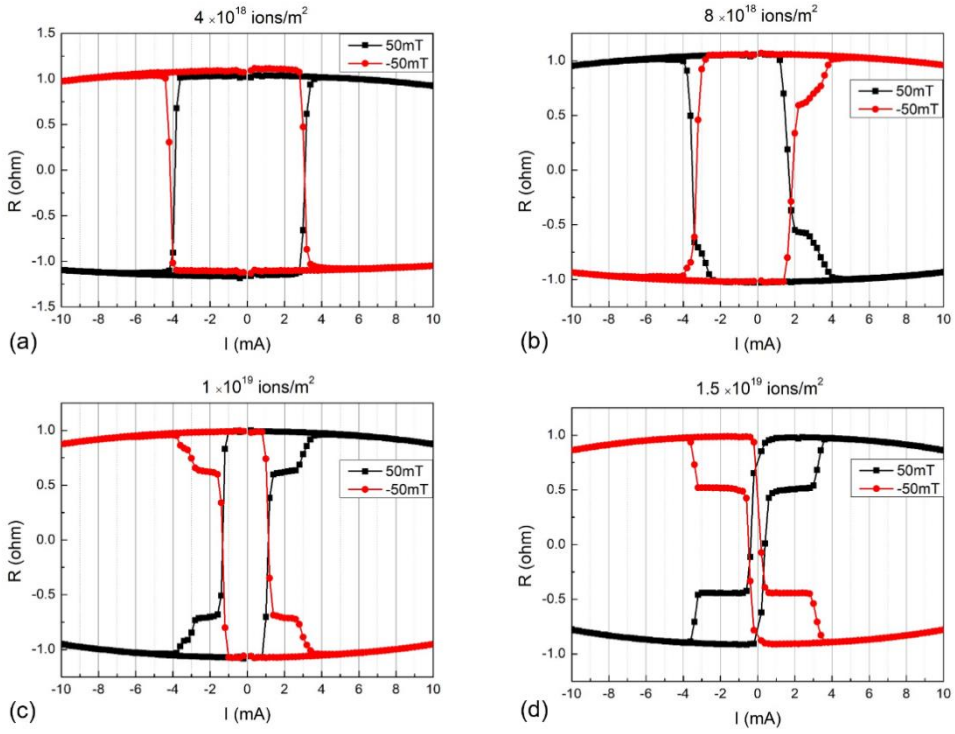

Figure 5-8. Anomalous Hall resistance loops measured under ±50 mT in-plane fields by sweeping the pulse current for the Type B sample irradiated at (a) 4×10^{18} ions/m^2, (b) 8×10^{18} ions/m^2, (c) 1×10^{19} ions/m^2 and (d) 1.5×10^{19} ions/m^2.

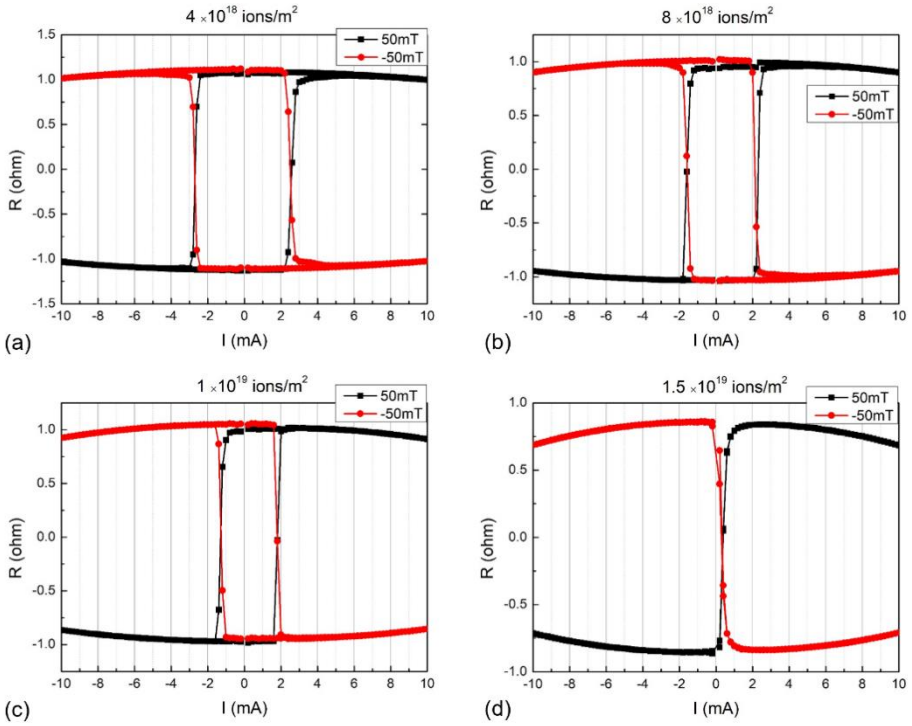

Figure 5-9. Anomalous resistance loops measured under ±50 mT in-plane fields by sweeping the pulse current for the Type C sample irradiated at (a) 4×10^{18} ions/m^2, (b) 8×10^{18} ions/m^2, (c) 1×10^{19} ions/m^2 and (d) 1.5×10^{19} ions/m^2.

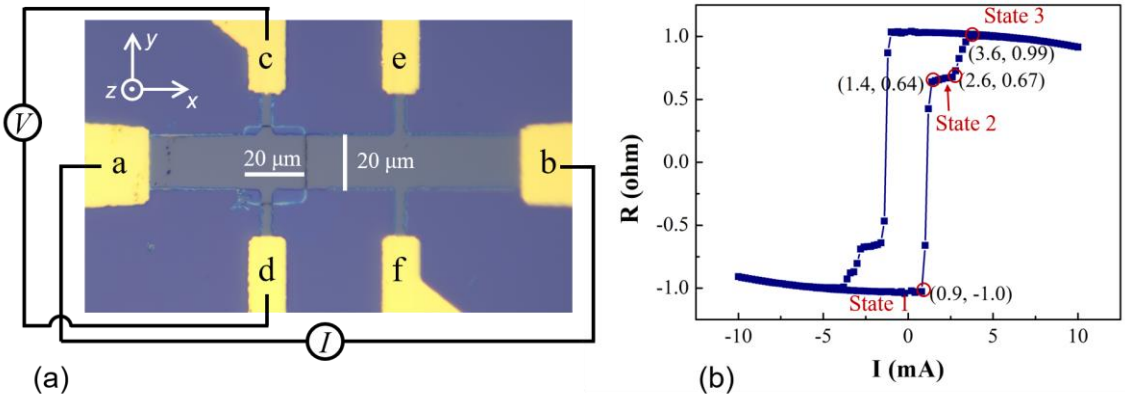

Figure 5-10. (a) Microscope image of Type B Hall bar structure, where electrodes a and b corresponding to the current pads while c and d correspond to the Hall voltage electrodes. (b)The same switching curve of Figure 4-7(c), but with the label of the resistance state.

As indicated in Figure 5-10 (b), when sweeping the current from -10mA to +10mA, we observe 3 different states: $R_H = -1\ \Omega$ at $I_{S1} \leq 0.9$ mA (State 1), $0.64\ \Omega < R_H < 0.67\ \Omega$ at 1.4 mA$< I_{S2} <$ 2.6 mA (State 2) and $R_H = 1\ \Omega$ at $I_{S3} \geq 3.6$ mA (State 3).

To gain deeper insight into the multi-state magnetization, we use a high-resolution Kerr microscope with electrical probes to directly observe the SOT switching. To maintain the consistency, we apply a 50 mT in-plane magnetic field and 5 ms current pulses with 0.02 mA step.

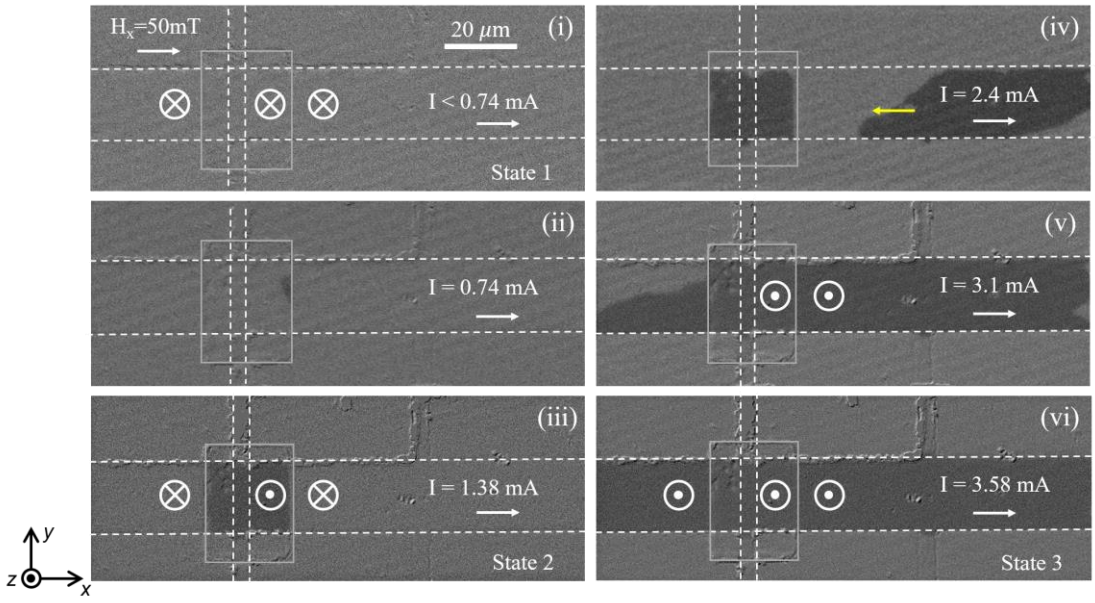

Figure 5-11. Kerr images showing the SOT induced magnetization switching process of the Hall bar under a 50 mT in-plane magnetic field. (i), (iii) and (vi) show the three magnetization states, while (ii), (iv) and (v) are the intermediate states. The white dashed lines indicate the current and voltage pads of the Hall bar. Inside the gray box is the irradiation area. The yellow arrow in (iv) shows the direction of domain wall motion.

A large perpendicular magnetic field is first applied to the sample to pre-saturate the magnetization along the -z axis. When the current pulse increases from 0 to 0.74 mA, reversed domains at some specific locations in the right panel of the irradiation region (delimited in the gray box in Figure 5-11) appear, as indicated by the dark domain in Figure 5-11 (ii). On the one hand, the reduced anisotropy induced by ion irradiation requires smaller external excitation, i.e. the magnetic field or current, to reverse the magnetization, leading to the switching of the irradiated region before the non-irradiated [60]. On the other hand, due to the existence of DMI, the preferential nucleation at one edge (on the right of the irradiation panel) are expected [180], as mentioned in Chapter 2.

After nucleation, the irradiated region is fully reversed by rapid DW propagation with increasing the current as shown in Figure 5-11 (iii) with I = 1.38 mA. After that, DW motion prevent from propagation outside the irradiated area showing a pinning at the edges of the irradiated and non-irradiated area. When the current increases up to 1.82 mA, new nucleation events happen at the right side of the Hall bar. When increasing the current pulse, the new nucleated domains propagate along the electron flow, whose direction is determined by the positive sign of DMI [167,190] and the negative spin Hall angle of tungsten [191]. When the current gets higher than 2.4 mA, reversed domains also propagate *or* nucleate at the left side of the irradiation region. Figure 5-11 (v) shows the domain configuration at I = 3.1 mA,

where the up domains have filled up the right side and the half of the left side of the irradiation region. Increasing the current up to 3.58 mA, all the magnetization has reversed to +z direction, as seen in Figure 5-11 (vi).

The Kerr microscopy images show that the values of the current for the different magnetic states shown in Figure 5-11 correspond to those on the SOT induced switching loop. In particular, for the first stage indicated in Figure 5-10 (b) (from State 1 to State 2), the sharp reverse induced by the current corresponds to the domain nucleation [192]. The value I_{S1} =0.9 mA (Figure 5-10 (b)) corresponding to the sharp switching is consistent with the value I = 0.74-1.38 mA measured in Figure 5-11 where the nucleation/propagation process is observed. It is worth noting that the current values obtained from the *R-I* curve and the Kerr microscopy show some discrepancy due to the different spatial resolution of these two techniques. Note that in Figure 5-11(iii)-(iv) the DW at the edges of the irradiated region is strongly pinned and cannot propagate outside of the irradiated region. This is due to the fact that at the irradiated-non irradiated border, there is a strong anisotropy gradient inducing a potential step for DW propagation as shown recently by Zhang *et al* [176] in nanodots.

Now let's discuss the switching process between state 2 and state 3 where DW nucleation occurs at the right side of the Hall bar and DW is pinned within the irradiated region. The state described in Figure 5-11 (iv) corresponds to a current of 2.4 mA, which is in the range of State 2 in Figure 5-10 (b) (1.4-2.6 mA). The DWs nucleated at the right of the Hall bar move toward the irradiated region, reversing the entire Hall bar on the right side. Another domain is present on the left side reversing the rest of the Hall bar. The reversal of the two Hall bars apart of the irradiated region may be the reason of the evolution of the Hall voltage between State 2 and State 3.

In order to verify this conjecture, we fabricate Hall bar with different sizes: the width of the current path is 10 μm and 6 μm, while that of the voltage path is 3 μm. We have fabricated the same irradiated region on the Hall cross and applied the same irradiation dose. Figure 5-12 presents the switching loops of the partially irradiated Hall bars with different current path widths, from which we figure out that the larger ratio of the current pad width and the voltage pad width (4 for 20 μm current pad, 3.3 for 10 μm and 2 for 6 μm), the more multi-level resistance is observed.

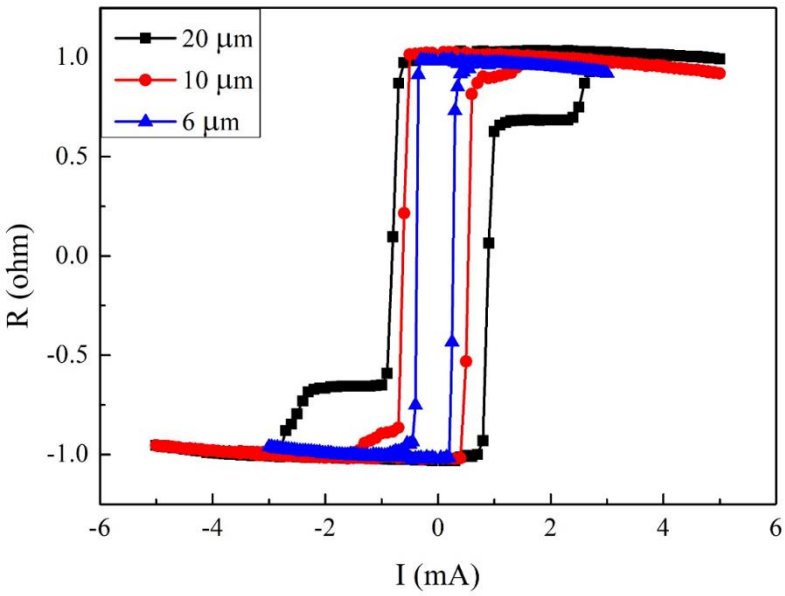

Figure 5-12. SOT induced switching under 50 mT in-plane magnetic field. The black, red and blue lines represent the switching loops of partially irradiated Hall bars with the width of current pad of 20 μm, 10 μm and 6 μm, respectively.

To further confirm this conclusion, we then develop the simulation using COMSOL Multiphysics [193] to simulate the current density distribution in the Hall cross. Due to the current flowing through the arms of the Hall cross[50], the current density in the center spread out from the voltage path, as shown in Figure 5-13. According to the current distribution, for the 20 μm width current path (Figure 5-13 (c)), the lateral dimension of the current distribution is as large as 38 μm, indicating that the Hall voltage is sensitive to the magnetization distribution far beyond the irradiated region (width of 20 μm). In other words, both the magnetizations inside and adjacent outside the irradiation area contribute to the Hall resistance, and the multi-state resistances (state 2 to 3) is attributed to the switching outside of the irradiated region.

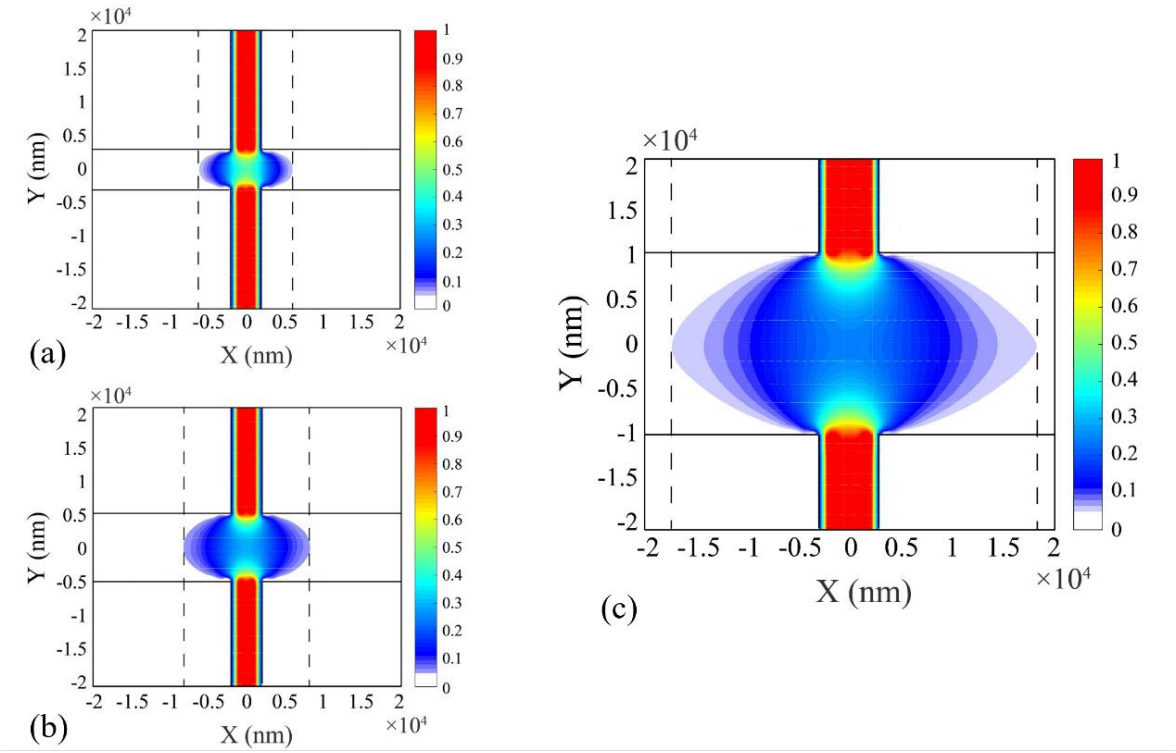

Figure 5-13. Simulations of the current density distribution in the Hall cross performed by COMSOL. Current is flowing along the y-direction, that is, the voltage pads. The solid line in the x-direction represents the edge of current path, where the width of it is 6 μm (a), 10 μm (b) and 20 μm (c). The dashed lines in the y-direction frame the current density distributions.

For the current pads of 10 μm and 6 μm, the current distribution along the x-axis is 17 and 11 μm, respectively, which show that in principle the Hall voltage is not sensitive to the non-irradiated region. In other words, no multi-states is expected. However, a small step in Figure 5-11 related to the 10 μm wire is observed. This is because the voltage pads are not at the absolute center of the irradiation region. The current may spread out of the irradiated region, leading to the small step in the switching loop.

For comparison, we plot the current distribution width as a function of the ration of the current and -voltage pad width, as shown in Figure 5-14. An exponential type behavior is observed. Based on this, the position of the multi-state can be controlled by adjusting the current-voltage pad width, which provides a method to realize multi-level devices.

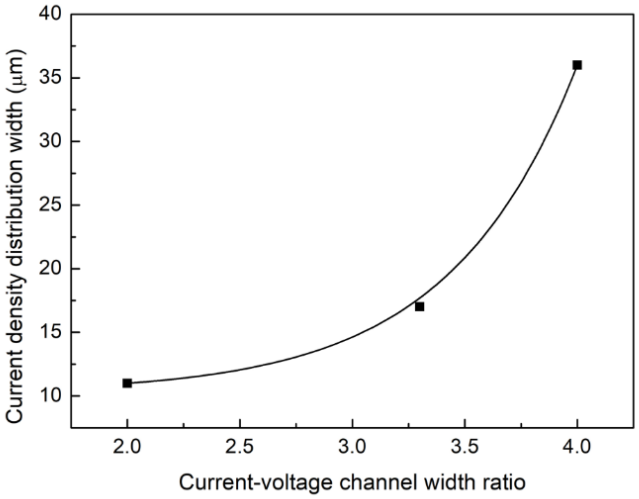

Figure 5-14. Current density distribution width as a function of the current-voltage pad width ratio in a Hall bar, the black line is the exponential fitting.

5.4 Summary

In this chapter, I have investigated the modulation of DW dynamics and then the SOT switching properties of He^+ irradiation devices. A strong increase of the DW velocity in the creep regime upon He^+ irradiation has been observed, which is due to the reduction of pinning centres induced by interface intermixing.

He^+ irradiation also provides a method to reduce the critical switching current in SOT devices, where a reduction over 60% in the critical current density is obtained.

In addition, multi-states magnetization switching loops induced by the SOT in a perpendicularly magnetized heterostructure is also demonstrated. This multi-states is attributed to the sensitivity of the Hall voltage not only to the irradiated region but also to the non-irradiated wire.

Conclusions and Perspectives

General conclusion

This thesis focuses on the modulation of spin-dependent interfacial effects in CoFeB-MgO based structures, including PMA, DMI, DW dynamics and SOT switching. The innovative approach to modulate the spin-dependent interfacial effects is light ion irradiation, which can control the degree of intermixing at interfaces.

The main contributions of this thesis are:

1. We have demonstrated the dependence of PMA on sputtering conditions in Ta-CoFeB-MgO structures, and also showed in agreement with previous studies that thermal annealing has a strong influence on the PMA through the crystallization process and the interface sharpness. A more original study has focused on interface engineering using ion irradiation. Asymmetric in-plane field-driven domain expansion experiments has shown that the DMI value is slightly reduced upon ion irradiation and a direct relationship between DMI and interface anisotropy has been demonstrated.
2. We have then presented that the SOT switching current density in W/$Co_{20}Fe_{60}B_{20}$(1nm)/MgO structure can be as low as 1.15×10^{6} A/cm^{2} with an assisting in-plane magnetic field, much lower than that of other heavy metal systems. The SOT induced switching process has also been observed by Kerr microscopy, showing that the magnetic switching is dominated by DW nucleation and propagation. We have evidenced that the ultra-efficient SOT-induced magnetic switching in the W/CoFeB/MgO is due to the combination of high SHA in tungsten, the low DW depinning field and the weak DMI.
3. More than 4-fold increase of DW velocity in the creep regime has been observed after ion irradiation. The improved interface intermixing leads to the reduction of pinning centers and magnetic anisotropy.
4. A reduction over 60% of the critical switching current in SOT devices has been realized in He^{+} irradiated devices. In addition, multi-states magnetization switching loops induced by the SOT in a perpendicularly magnetized heterostructure have also been demonstrated.

Perspectives

This thesis has shown that ion irradiation has proven to be a useful method to tailor high performance spintronic devices. However, there are still several questions to address in the near future:

1. We estimate the DMI constant by probing the asymmetric propagation of circular DW in the creep regime according to $\mathrm{D} = \mu_0 H_{DM} M_s \sqrt{\frac{A}{K_{eff}}}$, where A is the exchange stiffness constant. We have assumed A to be constant for all the samples. However, it is expected that the exchange stiffness constant is also very sensitive to the interface structures in ultrathin systems. But based on the previous studies, the quantification of A in ultra-thin films is always a difficult issue. The commonly used methods to measure A are mainly based on the spin wave dispersion and ferromagnetic resonance, in which the FM layers are thicker than 10 nm and considered to be a bulk material. However, for ultrathin films less than 10 nm, the above methods become less useful because they are not sufficiently sensitive to detect spin waves. Moreover, it is found that the value of A in the ultra-thin film is different from that in bulk material, whose thickness is larger than 10 nm due to the interfacial effect. Further studies are needed to develop high-resolution techniques to extract the interfacial exchange stiffness, especially for the samples that the interface conditions are slightly tuned.
2. Since annealing and irradiation are both efficient techniques to control the film interface, further experiments can be conducted to explore the combination of these two methods. Irradiation might raise the efficiency of annealing to gain good PMA, which could be a method to solve the integration problems of the STT/SOT devices and CMOS chips.
3. Focused ion beam (FIB) irradiation can be involved in future studies to locally modulate magnetic properties. It is a more powerful technique for which resolution down to 3 nm can be reached.

Bibliography

[1] Von Neumann. J & Kurzweil R. The Computer and the Brain[J]. Yale Univ. Press (2012).

[2] Kim N S, Austin T, Blaaww D, et al. Leakage Current: Moore's Law Meets Static Power [J]. IEEE Computer Society, 2003, 12: 68–74.

[3] Zhao W, Prenat G, Spintronics-Based Computing [M]. Berlin: Springer Berlin Heidelberg, 2015.

[4] Wang Y, Liu Y, Li S, et al. A 3us wake-up time nonvolatile processor based on ferroelectric flip-flops [C], 2012 Proceedings of the ESSCIRC (ESSCIRC). IEEE, 2012: 149-152.

[5] Xue C J, Sun G, Zhang Y, et al. Emerging non-volatile memories: opportunities and challenges[C], 2011 Proceedings of the Ninth IEEE/ACM/IFIP International Conference on Hardware/Software Codesign and System Synthesis (CODES+ ISSS). IEEE, 2011: 325-334.

[6] Kang W, Zhang Y, Wang Z, et al. Spintronics: Emerging ultra-low-power circuits and systems beyond MOS technology[J]. ACM Journal on Emerging Technologies in Computing Systems (JETC), 2015, 12(2): 16.

[7] Baibich M N, Broto J M, Fert A, et al. Giant magnetoresistance of (001) Fe/(001) Cr magnetic superlattices[J]. Physical review letters, 1988, 61(21): 2472.

[8] Binasch G, Grünberg P, Saurenbach F, et al. Enhanced magnetoresistance in layered magnetic structures with antiferromagnetic interlayer exchange[J]. Physical review B, 1989, 39(7): 4828.

[9] Tang D D, Wang P K, Speriosu V S, et al. Spin-valve RAM cell[J]. IEEE transactions on magnetics, 1995, 31(6): 3206-3208.

[10] Grochowski E. Emerging trends in data storage on magnetic hard disk drives[J]. Datatech (September 1998), ICG Publishing, 1998: 11-16.

[11] Chappert C, Fert A, Van Dau F N. The emergence of spin electronics in data storage[M], Nanoscience And Technology: A Collection of Reviews from Nature Journals. 2010: 147-157.

[12] Zhao W S, Wang Z H, Peng S Z, et al. Recent progresses in spin transfer torque-based magnetoresistive random access memory (STT-MRAM)[J]. Scientia Sinica Physica, Mechanica & Astronomica, 2016, 46(10): 107306.

[13] Prinz G A. Magnetoelectronics[J]. Science, 1998, 282(5394): 1660-1663.

[14] Miyazaki T, Tezuka N. Giant magnetic tunneling effect in Fe/Al2O3/Fe junction[J]. Journal of Magnetism and Magnetic Materials, 1995, 139(3): L231-L234.

[15] Moodera J S, Kinder L R, Wong T M, et al. Large magnetoresistance at room temperature in ferromagnetic thin film tunnel junctions[J]. Physical review letters, 1995, 74(16): 3273.

[16] Parkin S S P, Kaiser C, Panchula A, et al. Giant tunnelling magnetoresistance at room temperature with MgO (100) tunnel barriers[J]. Nature materials, 2004, 3(12): 862.

[17] Yuasa S, Nagahama T, Fukushima A, et al. Giant room-temperature magnetoresistance in single-crystal Fe/MgO/Fe magnetic tunnel junctions[J]. Nature materials, 2004, 3(12): 868.

[18] Ikeda S, Hayakawa J, Ashizawa Y, et al. Tunnel magnetoresistance of 604% at 300 K by suppression of Ta diffusion in CoFeB/ MgO/ CoFeB pseudo-spin-valves annealed at high temperature[J]. Applied Physics Letters, 2008, 93(8): 082508.

[19] Parkin S S P, Roche K P, Samant M G, et al. Exchange-biased magnetic tunnel junctions and application to nonvolatile magnetic random access memory[J]. Journal of Applied Physics, 1999, 85(8): 5828-5833.

[20] Durlam M, Naji P J, Omair A, et al. A 1-Mbit MRAM based on 1T1MTJ bit cell integrated with copper interconnects[J]. IEEE Journal of Solid-State Circuits, 2003, 38(5): 769-773.

[21] Bernard Dieny. Slide of the InMRAM summer school 2017, MRAM.

[22] Engel B N, Akerman J, Butcher B, et al. A 4-Mb toggle MRAM based on a novel bit and switching method[J]. IEEE Transactions on Magnetics, 2005, 41(1): 132-136.

[23] Berger L. Emission of spin waves by a magnetic multilayer traversed by a current[J]. Physical Review B, 1996, 54(13): 9353.

[24] Slonczewski J C. Current-driven excitation of magnetic multilayers[J]. Journal of Magnetism and Magnetic Materials, 1996, 159(1-2): L1-L7.

[25] Gilbert T L. A phenomenological theory of damping in ferromagnetic materials[J]. IEEE Transactions on Magnetics, 2004, 40(6): 3443-3449.

[26] Xiao J, Zangwill A, Stiles M D. Macrospin models of spin transfer dynamics[J]. Physical Review B, 2005, 72(1): 014446.

[27] Katine J A, Albert F J, Buhrman R A, et al. Current-driven magnetization reversal and spin-wave excitations in Co/Cu/Co pillars[J]. Physical review letters, 2000, 84(14): 3149.

[28] https://phys.org/news/2005-12-renesas-grandis-collaborate-nm-mram.html.

[29] Hosomi M, Yamagishi H, Yamamoto T, et al. A novel nonvolatile memory with spin torque transfer magnetization switching: Spin-RAM[C], IEEE InternationalElectron Devices Meeting, 2005. IEDM Technical Digest. IEEE, 2005: 459-462.

[30] Takemura R, Kawahara T, Miura K, et al. 2 Mb SPRAM design: Bi-directional current write and parallelizing-direction current read schemes based on spin-transfer torque switching[C], 2007 IEEE International Conference on Integrated Circuit Design and Technology. IEEE, 2007: 1-4.

[31] Ikeda S, Miura K, Yamamoto H, et al. A perpendicular-anisotropy CoFeB–MgO magnetic tunnel junction[J]. Nature materials, 2010, 9(9): 721.

[32] Nowak J J, Robertazzi R P, Sun J Z, et al. Voltage and size dependence on write-error-rates in STT MRAM down to 11 nm junction size[J]. IEEE Magn. Lett, 2016, 7: 1-4.

[33] Wei L, Alzate J G, Arslan U, et al. 13.3 A 7Mb STT-MRAM in 22FFL FinFET Technology with 4ns Read Sensing Time at 0.9 V Using Write-Verify-Write Scheme and Offset-Cancellation Sensing Technique[C], 2019 IEEE International Solid-State Circuits Conference-(ISSCC). IEEE, 2019: 214-216.

[34] Amara-Dababi S, Sousa R C, Chshiev M, et al. Charge trapping-detrapping mechanism of barrier breakdown in MgO magnetic tunnel junctions[J]. Applied Physics Letters, 2011, 99(8): 083501.

[35] Zhao W S, Zhang Y, Devolder T, et al. Failure and reliability analysis of STT-MRAM[J].

Microelectronics Reliability, 2012, 52(9-10): 1848-1852.

[36] Miron I M, Gaudin G, Auffret S, et al. Current-driven spin torque induced by the Rashba effect in a ferromagnetic metal layer[J]. Nature materials, 2010, 9(3): 230.

[37] Liu L, Moriyama T, Ralph D C, et al. Spin-torque ferromagnetic resonance induced by the spin Hall effect[J]. Physical review letters, 2011, 106(3): 036601.

[38] Miron I M, Garello K, Gaudin G, et al. Perpendicular switching of a single ferromagnetic layer induced by in-plane current injection[J]. Nature, 2011, 476(7359): 189.

[39] Cubukcu M, Boulle O, Drouard M, et al. Spin-orbit torque magnetization switching of a three-terminal perpendicular magnetic tunnel junction[J]. Applied Physics Letters, 2014, 104(4): 042406.

[40] Liu L, Lee O J, Gudmundsen T J, et al. Current-induced switching of perpendicularly magnetized magnetic layers using spin torque from the spin Hall effect[J]. Physical review letters, 2012, 109(9): 096602.

[41] Liu L, Pai C F, Li Y, et al. Spin-torque switching with the giant spin Hall effect of tantalum[J]. Science, 2012, 336(6081): 555-558.

[42] Pai C F, Liu L, Li Y, et al. Spin transfer torque devices utilizing the giant spin Hall effect of tungsten[J]. Applied Physics Letters, 2012, 101(12): 122404.

[43] Garello K, Miron I M, Avci C O, et al. Symmetry and magnitude of spin–orbit torques in ferromagnetic heterostructures[J]. Nature nanotechnology, 2013, 8(8): 587.

[44] Emori S, Bauer U, Ahn S M, et al. Current-driven dynamics of chiral ferromagnetic domain walls[J]. Nature materials, 2013, 12(7): 611.

[45] Kim J, Sinha J, Hayashi M, et al. Layer thickness dependence of the current-induced effective field vector in Ta| CoFeB| MgO[J]. Nature materials, 2013, 12(3): 240.

[46] Zhang C, Yamanouchi M, Sato H, et al. Magnetization reversal induced by in-plane current in Ta/CoFeB/MgO structures with perpendicular magnetic easy axis[J]. Journal of Applied Physics, 2014, 115(17): 17C714.

[47] Kim K W, Seo S M, Ryu J, et al. Magnetization dynamics induced by in-plane currents in ultrathin magnetic nanostructures with Rashba spin-orbit coupling[J]. Physical Review B, 2012, 85(18): 180404.

[48] Lee K S, Lee S W, Min B C, et al. Threshold current for switching of a perpendicular magnetic layer induced by spin Hall effect[J]. Applied Physics Letters, 2013, 102(11): 112410.

[49] Fukami S, Zhang C, DuttaGupta S, et al. Magnetization switching by spin–orbit torque in an antiferromagnet–ferromagnet bilayer system[J]. Nature materials, 2016, 15(5): 535.

[50] van den Brink A, Vermijs G, Solignac A, et al. Field-free magnetization reversal by spin-Hall effect and exchange bias[J]. Nature communications, 2016, 7: 10854.

[51] Safeer C K, Jué E, Lopez A, et al. Spin–orbit torque magnetization switching controlled by geometry[J]. Nature nanotechnology, 2016, 11(2): 143.

[52] Yu G, Upadhyaya P, Fan Y, et al. Switching of perpendicular magnetization by spin–orbit torques in the absence of external magnetic fields[J]. Nature nanotechnology, 2014, 9(7): 548.

[53] Parkin S S P, Hayashi M, Thomas L. Magnetic domain-wall racetrack memory[J]. Science, 2008, 320(5873): 190-194.

[54] Anthony Beguivin. Domain wall behavior in magnetic nanowires [D]. Cambridge: University of Cambridge, 2014.

[55] Zhang S, Li Z. Roles of nonequilibrium conduction electrons on the magnetization dynamics of ferromagnets[J]. Physical Review Letters, 2004, 93(12): 127204.

[56] Khomskii D I, Freimuth A. Charged vortices in high temperature superconductors[J]. Physical review letters, 1995, 75(7): 1384.

[57] Chauve P, Giamarchi T, Le Doussal P. Creep and depinning in disordered media[J]. Physical Review B, 2000, 62(10): 6241.

[58] Nattermann T, Pokrovsky V, Vinokur V M. Hysteretic dynamics of domain walls at finite temperatures[J]. Physical Review Letters, 2001, 87(19): 197005.

[59] Brazovskii S, Nattermann T. Pinning and sliding of driven elastic systems: from domain walls to charge density waves[J]. Advances in Physics, 2004, 53(2): 177-252.

[60] Lemerle S, Ferré J, Chappert C, et al. Domain wall creep in an Ising ultrathin magnetic film[J]. Physical review letters, 1998, 80(4): 849.

[61] Krusin-Elbaum L, Shibauchi T, Argyle B, et al. Stable ultrahigh-density magneto-optical recordings using introduced linear defects[J]. Nature, 2001, 410(6827): 444.

[62] Setter N, Damjanovic D, Eng L, et al. Ferroelectric thin films: Review of materials, properties, and applications[J]. Journal of applied physics, 2006, 100(5): 051606.

[63] Kim D H, Choe S B, Shin S C. Direct observation of Barkhausen avalanche in Co thin films[J]. Physical review letters, 2003, 90(8): 087203.

[64] Metaxas P J. Creep and flow dynamics of magnetic domain walls: weak disorder, wall binding, and periodic pinning[M], Solid State Physics. Academic Press, 2010, 62: 75-162.

[65] Gilbert T L. A Lagrangian formulation of the gyromagnetic equation of the magnetization field[J]. Phys. Rev., 1955, 100: 1243.

[66] Metaxas P J, Jamet J P, Mougin A, et al. Creep and flow regimes of magnetic domain-wall motion in ultrathin Pt/Co/Pt films with perpendicular anisotropy[J]. Physical review letters, 2007, 99(21): 217208.

[67] Cayssol F, Ravelosona D, Chappert C, et al. Domain wall creep in magnetic wires[J]. Physical review letters, 2004, 92(10): 107202.

[68] Jeudy V, Mougin A, Bustingorry S, et al. Universal pinning energy barrier for driven domain walls in thin ferromagnetic films[J]. Physical review letters, 2016, 117(5): 057201.

[69] Tybell T, Paruch P, Giamarchi T, et al. Domain Wall Creep in Epitaxial Ferroelectric P b (Z r 0.2 T i 0.8) O 3 Thin Films[J]. Physical review letters, 2002, 89(9): 097601.

[70] Le Doussal P, Wiese K J, Moulinet S, et al. Height fluctuations of a contact line: A direct measurement of the renormalized disorder correlator[J]. EPL (Europhysics Letters), 2009, 87(5): 56001.

[71] Bonamy D, Santucci S, Ponson L. Crackling dynamics in material failure as the signature of a self-organized dynamic phase transition[J]. Physical review letters, 2008, 101(4): 045501.

[72] Jagla E A, Kolton A B. A mechanism for spatial and temporal earthquake clustering[J]. Journal of Geophysical Research: Solid Earth, 2010, 115(B5).

[73] Herrera Diez L, García-Sánchez F, Adam J P, et al. Controlling magnetic domain wall motion in the creep regime in He+-irradiated CoFeB/MgO films with perpendicular anisotropy[J]. Applied Physics Letters, 2015, 107(3): 032401.

[74] Pardo R D, Torres W S, Kolton A B, et al. Universal depinning transition of domain walls in ultrathin ferromagnets[J]. Physical Review B, 2017, 95(18): 184434.

[75] Herrera Diez L, Voto M, Casiraghi A, et al. Enhancement of the Dzyaloshinskii-Moriya interaction and domain wall velocity through interface intermixing in Ta/CoFeB/MgO[J]. Physical Review B, 2019, 99(5): 054431.

[76] Tatara G, Kohno H. Theory of current-driven domain wall motion: Spin transfer versus momentum transfer[J]. Physical review letters, 2004, 92(8): 086601.

[77] Thiaville A, Nakatani Y, Miltat J, et al. Micromagnetic understanding of current-driven domain wall motion in patterned nanowires[J]. EPL (Europhysics Letters), 2005, 69(6): 990.

[78] Moore T A, Miron I M, Gaudin G, et al. High domain wall velocities induced by current in ultrathin Pt/Co/AlOx wires with perpendicular magnetic anisotropy[J]. Applied Physics Letters, 2008, 93(26): 262504.

[79] Miron I M, Moore T, Szambolics H, et al. Fast current-induced domain-wall motion controlled by the Rashba effect[J]. Nature materials, 2011, 10(6): 419.

[80] Emori S, Bono D C, Beach G S D. Interfacial current-induced torques in Pt/Co/GdOx[J]. Applied Physics Letters, 2012, 101(4): 042405.

[81] Haazen P P J, Murè E, Franken J H, et al. Domain wall depinning governed by the spin Hall effect[J]. Nature materials, 2013, 12(4): 299.

[82] Koyama T, Chiba D, Ueda K, et al. Observation of the intrinsic pinning of a magnetic domain wall in a ferromagnetic nanowire[J]. Nature materials, 2011, 10(3): 194.

[83] Miron I M, Zermatten P J, Gaudin G, et al. Domain wall spin torquemeter[J]. Physical review letters, 2009, 102(13): 137202.

[84] Thiaville A, Rohart S, Jué É, et al. Dynamics of Dzyaloshinskii domain walls in ultrathin magnetic films[J]. EPL (Europhysics Letters), 2012, 100(5): 57002.

[85] Heide M, Bihlmayer G, Blügel S. Dzyaloshinskii-Moriya interaction accounting for the orientation of magnetic domains in ultrathin films: Fe/W (110)[J]. Physical Review B, 2008, 78(14): 140403.

[86] Khvalkovskiy A V, Cros V, Apalkov D, et al. Matching domain-wall configuration and spin-orbit torques for efficient domain-wall motion[J]. Physical Review B, 2013, 87(2): 020402.

[87] Peng S, Zhu D, Zhou J, et al. Modulation of Heavy Metal/Ferromagnetic Metal Interface for High-Performance Spintronic Devices[J]. Advanced Electronic Materials, 2019: 1900134.

[88] van Vleck J H. On the anisotropy of cubic ferromagnetic crystals[J]. Physical Review, 1937, 52(11): 1178.

[89] Néel L. Anisotropie magnétique superficielle et surstructures d'orientation[J]. Journal de Physique et le Radium, 1954, 15(4): 225-239.

[90] Siegmann H C, Stöhr J. Magnetism: From Fundamentals to Nanoscale Dynamics[M]. Springer Bln, 2006.

[91] Weller D, Wu Y, Stöhr J, et al. Orbital magnetic moments of Co in multilayers with perpendicular magnetic anisotropy[J]. Physical review B, 1994, 49(18): 12888.

[92] Ujfalussy B, Szunyogh L, Bruno P, et al. First-principles calculation of the anomalous perpendicular anisotropy in a Co monolayer on Au (111)[J]. Physical review letters, 1996, 77(9): 1805.

[93] Carcia P F, Meinhaldt A D, Suna A. Perpendicular magnetic anisotropy in Pd/Co thin film layered structures[J]. Applied Physics Letters, 1985, 47(2): 178-180.

[94] Yang H X, Chshiev M, Dieny B, et al. First-principles investigation of the very large perpendicular magnetic anisotropy at Fe| MgO and Co| MgO interfaces[J]. Physical Review B, 2011, 84(5): 054401.

[95] Yakata S, Kubota H, Suzuki Y, et al. Influence of perpendicular magnetic anisotropy on spin-transfer switching current in CoFeB⁄ MgO⁄ CoFeB magnetic tunnel junctions[J]. Journal of Applied Physics, 2009, 105(7): 07D131.

[96] Worledge D C, Hu G, Abraham D W, et al. Spin torque switching of perpendicular Ta｜CoFeB｜MgO-based magnetic tunnel junctions[J]. Applied Physics Letters, 2011, 98(2): 022501.

[97] Peng S, Wang M, Yang H, et al. Origin of interfacial perpendicular magnetic anisotropy in MgO/CoFe/metallic capping layer structures[J]. Scientific reports, 2015, 5: 18173.

[98] Peng S, Zhao W, Qiao J, et al. Giant interfacial perpendicular magnetic anisotropy in MgO/CoFe/capping layer structures[J]. Applied Physics Letters, 2017, 110(7): 072403.

[99] Sinha J, Gruber M, Kodzuka M, et al. Influence of boron diffusion on the perpendicular magnetic anisotropy in Ta| CoFeB| MgO ultrathin films[J]. Journal of Applied Physics, 2015, 117(4): 043913.

[100] Wang Z, Saito M, McKenna K P, et al. Atomic-Scale structure and local chemistry of CoFeB–MgO magnetic tunnel junctions[J]. Nano letters, 2016, 16(3): 1530-1536.

[101] Greer A A, Gray A X, Kanai S, et al. Observation of boron diffusion in an annealed Ta/CoFeB/MgO magnetic tunnel junction with standing-wave hard x-ray photoemission[J]. Applied Physics Letters, 2012, 101(20): 202402.

[102] Bai Z, Shen L, Wu Q, et al. Boron diffusion induced symmetry reduction and scattering in CoFeB/MgO/CoFeB magnetic tunnel junctions[J]. Physical Review B, 2013, 87(1): 014114.

[103] Khoo K H, Wu G, Jhon M H, et al. First-principles study of perpendicular magnetic anisotropy in CoFe/MgO and CoFe/Mg 3 B 2 O 6 interfaces[J]. Physical Review B, 2013, 87(17): 174403.

[104] Hallal A, Yang H X, Dieny B, et al. Anatomy of perpendicular magnetic anisotropy in Fe/MgO magnetic tunnel junctions: First-principles insight[J]. Physical Review B, 2013, 88(18): 184423.

[105] Ikeda S, Koizumi R, Sato H, et al. Boron composition dependence of magnetic anisotropy and tunnel magnetoresistance in MgO/CoFe (B) based stack structures[J]. IEEE Transactions on Magnetics, 2012, 48(11): 3829-3832.

[106] Cai G, Wu Z, Guo F, et al. First-principles calculations of perpendicular magnetic anisotropy in $Fe_{1-x}Co_x$/MgO (001) thin films[J]. Nanoscale research letters, 2015, 10(1): 126.

[107] Fert A, Cros V, Sampaio J. Skyrmions on the track[J]. Nature nanotechnology, 2013, 8(3): 152.

[108] Sampaio J, Cros V, Rohart S, et al. Nucleation, stability and current-induced motion of isolated magnetic skyrmions in nanostructures[J]. Nature nanotechnology, 2013, 8(11): 839.

[109] Ryu K S, Thomas L, Yang S H, et al. Chiral spin torque at magnetic domain walls[J]. Nature nanotechnology, 2013, 8(7): 527.

[110] Zhao X, Zhang X, Yang H, et al. Ultra-efficient spin–orbit torque induced magnetic switching in W/CoFeB/MgO structures[J]. Nanotechnology, 2019, 30(33): 335707.

[111] Heisenberg W. Zur theorie des ferromagnetismus[M], Original Scientific Papers Wissenschaftliche Originalarbeiten. Springer, Berlin, Heidelberg, 1985: 580-597.

[112] Fert A, Reyren N, Cros V. Magnetic skyrmions: advances in physics and potential applications[J]. Nature Reviews Materials, 2017, 2(7): 1-15.

[113] Khan R A, Shepley P M, Hrabec A, et al. Effect of annealing on the interfacial Dzyaloshinskii-Moriya interaction in Ta/CoFeB/MgO trilayers[J]. Applied Physics Letters, 2016, 109(13): 132404.

[114] Dupé B, Hoffmann M, Paillard C, et al. Tailoring magnetic skyrmions in ultra-thin transition metal films[J]. Nature communications, 2014, 5: 4030.

[115] Gross I, Martínez L J, Tetienne J P, et al. Direct measurement of interfacial Dzyaloshinskii-Moriya interaction in X| CoFeB| MgO heterostructures with a scanning NV magnetometer (X= Ta, TaN, and W)[J]. Physical Review B, 2016, 94(6): 064413.

[116] Bode M, Heide M, Von Bergmann K, et al. Chiral magnetic order at surfaces driven by inversion asymmetry[J]. Nature, 2007, 447(7141): 190.

[117] Fert A, Levy P M. Role of anisotropic exchange interactions in determining the properties of spin-glasses[J]. Physical Review Letters, 1980, 44(23): 1538.

[118] Fert A R. Magnetic and transport properties of metallic multilayers[C], Materials Science Forum. Trans Tech Publications, 1990, 59: 439-480.

[119] Boulle O, Vogel J, Yang H, et al. Room-temperature chiral magnetic skyrmions in ultrathin magnetic nanostructures[J]. Nature nanotechnology, 2016, 11(5): 449.

[120] Yang H, Boulle O, Cros V, et al. Controlling dzyaloshinskii-moriya interaction via chirality dependent atomic-layer stacking, insulator capping and electric field[J]. Scientific reports, 2018, 8.

[121] Yang H, Thiaville A, Rohart S, et al. Anatomy of dzyaloshinskii-moriya interaction at Co/Pt interfaces[J]. Physical review letters, 2015, 115(26): 267210.

[122] Jiang W, Upadhyaya P, Zhang W, et al. Blowing magnetic skyrmion bubbles[J]. Science, 2015, 349(6245): 283-286.

[123] Belabbes A, Bihlmayer G, Bechstedt F, et al. Hund's Rule-Driven Dzyaloshinskii-Moriya Interaction at 3 d− 5 d Interfaces[J]. Physical review letters, 2016, 117(24): 247202.

[124] Yang H, Chen G, Cotta A A C, et al. Significant Dzyaloshinskii–Moriya interaction at

graphene–ferromagnet interfaces due to the Rashba effect[J]. Nature materials, 2018, 17(7): 605.

[125] Varignon J, Vila L, Barthélémy A, et al. A new spin for oxide interfaces[J]. Nature Physics, 2018, 14(4): 322.

[126] Manchon A, Koo H C, Nitta J, et al. New perspectives for Rashba spin–orbit coupling[J]. Nature materials, 2015, 14(9): 871.

[127] Obata K, Tatara G. Current-induced domain wall motion in Rashba spin-orbit system[J]. Physical Review B, 2008, 77(21): 214429.

[128] Wang X, Manchon A. Diffusive spin dynamics in ferromagnetic thin films with a Rashba interaction[J]. Physical review letters, 2012, 108(11): 117201.

[129] Pesin D A, MacDonald A H. Quantum kinetic theory of current-induced torques in Rashba ferromagnets[J]. Physical Review B, 2012, 86(1): 014416.

[130] Van der Bijl E, Duine R A. Current-induced torques in textured Rashba ferromagnets[J]. Physical Review B, 2012, 86(9): 094406.

[131] Belabbes A, Bihlmayer G, Blügel S, et al. Oxygen-enabled control of Dzyaloshinskii-Moriya Interaction in ultra-thin magnetic films[J]. Scientific reports, 2016, 6: 24634.

[132] Cao A, Zhang X, Koopmans B, et al. Tuning the Dzyaloshinskii–Moriya interaction in Pt/Co/MgO heterostructures through the MgO thickness[J]. Nanoscale, 2018, 10(25): 12062-12067.

[133] Torrejon J, Kim J, Sinha J, et al. Interface control of the magnetic chirality in CoFeB/MgO heterostructures with heavy-metal underlayers[J]. Nature communications, 2014, 5: 4655.

[134] Zhao W, Zhao X, Zhang B, et al. Failure analysis in magnetic tunnel junction nanopillar with interfacial perpendicular magnetic anisotropy[J]. Materials, 2016, 9(1): 41.

[135] O'Sullivan E J. Magnetic tunnel junction-based MRAM and related processing issues[J]. Materials Science, 2005: 1-17.

[136] Mathon J, Umerski A. Theory of tunneling magnetoresistance of an epitaxial Fe/MgO/Fe (001) junction[J]. Physical Review B, 2001, 63(22): 220403.

[137] Butler W H, Zhang X G, Schulthess T C, et al. Spin-dependent tunneling conductance of Fe| MgO| Fe sandwiches[J]. Physical Review B, 2001, 63(5): 054416.

[138] Naik V B, Meng H, Sbiaa R. Thick CoFeB with perpendicular magnetic anisotropy in CoFeB-MgO based magnetic tunnel junction[J]. Aip Advances, 2012, 2(4): 042182.

[139] Yuasa S, Djayaprawira D D. Giant tunnel magnetoresistance in magnetic tunnel junctions with a crystalline MgO (0 0 1) barrier[J]. Journal of Physics D: Applied Physics, 2007, 40(21): R337.

[140] Le Boité M G, Traverse A, Bernas H, et al. Study of ion beam mixed multilayers via neutron scattering[J]. Materials Letters, 1988, 6(5-6): 173-176.

[141] Le Boité M G, Traverse A, Nevot L, et al. Characterization of ion-beam mixed multilayers via grazing x-ray reflectometry[J]. Journal of Materials Research, 1988, 3(6): 1089-1096.

[142] Chappert C, Bernas H, Ferré J, et al. Planar patterned magnetic media obtained by ion

irradiation[J]. Science, 1998, 280(5371): 1919-1922.

[143] Ultrathin magnetic structures II: Measurement techniques and novel magnetic properties[M]. Springer Science & Business Media, 2006.

[144] Devolder T. Light ion irradiation of Co/Pt systems: Structural origin of the decrease in magnetic anisotropy[J]. Physical Review B, 2000, 62(9): 5794.

[145] Ravelosona D, Devolder T, Bernas H, et al. Magnetic properties of irradiated highly anisotropic materials[J]. IEEE transactions on magnetics, 2001, 37(4): 1643-1645.

[146] Hauet T, Hellwig O, Park S H, et al. Influence of ion irradiation on switching field and switching field distribution in arrays of Co/Pd-based bit pattern media[J]. Applied Physics Letters, 2011, 98(17): 172506.

[147] Devolder T, Pizzini S, Vogel J, et al. X-ray absorption analysis of sputter-grown Co/Pt stackings before and after helium irradiation[J]. The European Physical Journal B-Condensed Matter and Complex Systems, 2001, 22(2): 193-201.

[148] Devolder T, Barisic I, Eimer S, et al. Irradiation-induced tailoring of the magnetism of CoFeB/MgO ultrathin films[J]. Journal of applied Physics, 2013, 113(20): 203912.

[149] Cayssol F, Menéndez J L, Ravelosona D, et al. Enhancing domain wall motion in magnetic wires by ion irradiation[J]. Applied Physics Letters, 2005, 86(2): 022503.

[150] Argyres P N. Theory of the Faraday and Kerr effects in ferromagnetics[J]. Physical Review, 1955, 97(2): 334.

[151] Allwood D A, Xiong G, Cooke M D, et al. Magneto-optical Kerr effect analysis of magnetic nanostructures[J]. Journal of Physics D: Applied Physics, 2003, 36(18): 2175.

[152] Je S G, Kim D H, Yoo S C, et al. Asymmetric magnetic domain-wall motion by the Dzyaloshinskii-Moriya interaction[J]. Physical Review B, 2013, 88(21): 214401.

[153] Cortés-Ortuño D, Landeros P. Influence of the Dzyaloshinskii–Moriya interaction on the spin-wave spectra of thin films[J]. Journal of Physics: Condensed Matter, 2013, 25(15): 156001.

[154] Di K, Zhang V L, Lim H S, et al. Direct observation of the Dzyaloshinskii-Moriya interaction in a Pt/Co/Ni film[J]. Physical review letters, 2015, 114(4): 047201.

[155] Zhang V L, Di K, Lim H S, et al. In-plane angular dependence of the spin-wave nonreciprocity of an ultrathin film with Dzyaloshinskii-Moriya interaction[J]. Applied Physics Letters, 2015, 107(2): 022402.

[156] Belmeguenai M, Gabor M S, Roussigné Y, et al. Brillouin light scattering investigation of the thickness dependence of Dzyaloshinskii-Moriya interaction in C o 0.5 F e 0.5 ultrathin films[J]. Physical Review B, 2016, 93(17): 174407.

[157] Nagaosa N, Sinova J, Onoda S, et al. Anomalous hall effect[J]. Reviews of modern physics, 2010, 82(2): 1539.

[158] Wang W X, Yang Y, Naganuma H, et al. The perpendicular anisotropy of Co40Fe40B20 sandwiched between Ta and MgO layers and its application in CoFeB/MgO/CoFeB tunnel junction[J]. Applied Physics Letters, 2011, 99(1): 012502.

[159] Isogami S, Tsunoda M, Komagaki K, et al. In situ heat treatment of ultrathin MgO layer for giant magnetoresistance ratio with low resistance area product in CoFeB/MgO/CoFeB

magnetic tunnel junctions[J]. Applied Physics Letters, 2008, 93(19): 192109.

[160] Hayakawa J, Ikeda S, Matsukura F, et al. Dependence of giant tunnel magnetoresistance of sputtered CoFeB/MgO/CoFeB magnetic tunnel junctions on MgO barrier thickness and annealing temperature[J]. Japanese Journal of Applied Physics, 2005, 44(4L): L587.

[161] Debski A, Debski R, Gasior W. New Features of Entall Database: Comparison of Experimental and Model Formation Enthalpies/Nowe Funkcje Bazy Danych Entall: Porównanie Doświadczalnych I Modelowych Entalpii Tworzenia[J]. Archives of Metallurgy and Materials, 2014, 59(4): 1337-1343.

[162] Sinha J, Hayashi M, Kellock A J, et al. Enhanced interface perpendicular magnetic anisotropy in Ta| CoFeB| MgO using nitrogen doped Ta underlayers[J]. Applied Physics Letters, 2013, 102(24): 242405.

[163] Ingvarsson S, Xiao G, Parkin S S P, et al. Thickness-dependent magnetic properties of Ni81Fe19, Co90Fe10 and Ni65Fe15Co20 thin films[J]. Journal of magnetism and magnetic materials, 2002, 251(2): 202-206.

[164] Nicolenco A, Tsyntsaru N, Fornell J, et al. Mapping of magnetic and mechanical properties of Fe-W alloys electrodeposited from Fe (III)-based glycolate-citrate bath[J]. Materials & Design, 2018, 139: 429-438.

[165] Devolder T, Ferré J, Chappert C, et al. Magnetic properties of He+-irradiated Pt/Co/Pt ultrathin films[J]. Physical Review B, 2001, 64(6): 064415.

[166] Belmeguenai M, Adam J P, Roussigné Y, et al. Interfacial Dzyaloshinskii-Moriya interaction in perpendicularly magnetized Pt/Co/AlO x ultrathin films measured by Brillouin light spectroscopy[J]. Physical Review B, 2015, 91(18): 180405.

[167] Jaiswal S, Litzius K, Lemesh I, et al. Investigation of the Dzyaloshinskii-Moriya interaction and room temperature skyrmions in W/CoFeB/MgO thin films and microwires[J]. Applied Physics Letters, 2017, 111(2): 022409.

[168] Yamanouchi M, Jander A, Dhagat P, et al. Domain structure in CoFeB thin films with perpendicular magnetic anisotropy[J]. IEEE Magnetics Letters, 2011, 2: 3000304-3000304.

[169] Ma X, Yu G, Tang C, et al. Interfacial Dzyaloshinskii-Moriya Interaction: Effect of 5 d Band Filling and Correlation with Spin Mixing Conductance[J]. Physical review letters, 2018, 120(15): 157204.

[170] Zimmermann B, Legrand W, Maccariello D, et al. Dzyaloshinskii-Moriya interaction at disordered interfaces from ab initio theory: Robustness against intermixing and tunability through dusting[J]. Applied Physics Letters, 2018, 113(23): 232403.

[171] Tacchi S, Troncoso R E, Ahlberg M, et al. Interfacial Dzyaloshinskii-Moriya interaction in Pt/CoFeB films: effect of the heavy-metal thickness[J]. Physical review letters, 2017, 118(14): 147201.

[172] Kim G W, Samardak A S, Kim Y J, et al. Role of the Heavy Metal's Crystal Phase in Oscillations of Perpendicular Magnetic Anisotropy and the Interfacial Dzyaloshinskii-Moriya Interaction in W/CoFeB/MgO Films[J]. Physical Review Applied, 2018, 9(6): 064005.

[173] Hao Q, Xiao G. Giant spin Hall effect and switching induced by spin-transfer torque in a W/Co 40 Fe 40 B 20/MgO structure with perpendicular magnetic anisotropy[J]. Physical

Review Applied, 2015, 3(3): 034009.

[174] Qiu X, Deorani P, Narayanapillai K, et al. Angular and temperature dependence of current induced spin-orbit effective fields in Ta/CoFeB/MgO nanowires[J]. Scientific reports, 2014, 4: 4491.

[175] Pai C F, Nguyen M H, Belvin C, et al. Enhancement of perpendicular magnetic anisotropy and transmission of spin-Hall-effect-induced spin currents by a Hf spacer layer in W/Hf/CoFeB/MgO layer structures[J]. Applied Physics Letters, 2014, 104(8): 082407.

[176] Zhang Y, Zhang X, Vernier N, et al. Domain-Wall Motion Driven by Laplace Pressure in CoFeB/MgO Nanodots with Perpendicular Anisotropy[J]. Physical Review Applied, 2018, 9(6): 064027.

[177] Shahbazi K, Kim J V, Nembach H T, et al. Domain-wall motion and interfacial Dzyaloshinskii-Moriya interactions in Pt/Co/Ir (t Ir)/Ta multilayers[J]. Physical Review B, 2019, 99(9): 094409.

[178] Zhang X, Vernier N, Zhao W, et al. Direct observation of domain-wall surface tension by deflating or inflating a magnetic bubble[J]. Physical Review Applied, 2018, 9(2): 024032.

[179] Zhang X, Vernier N, Cao Z, et al. Magnetoresistive sensors based on the elasticity of domain walls[J]. Nanotechnology, 2018, 29(36): 365502.

[180] Pizzini S, Vogel J, Rohart S, et al. Chirality-induced asymmetric magnetic nucleation in Pt/Co/AlO x ultrathin microstructures[J]. Physical review letters, 2014, 113(4): 047203.

[181] Han D S, Kim N H, Kim J S, et al. Asymmetric hysteresis for probing Dzyaloshinskii–Moriya interaction[J]. Nano letters, 2016, 16(7): 4438-4446.

[182] Jang P H, Song K, Lee S J, et al. Detrimental effect of interfacial Dzyaloshinskii-Moriya interaction on perpendicular spin-transfer-torque magnetic random access memory[J]. Applied Physics Letters, 2015, 107(20): 202401.

[183] Siracusano G, Tomasello R, Puliafito V, et al. Micromagnetic analysis of statistical switching in perpendicular STT-MRAM with interfacial Dzyaloshinskii–Moriya Interaction[J]. IEEE Transactions on Magnetics, 2017, 53(11): 1-5.

[184] Azevedo A, Vilela-Leão L H, Rodríguez-Suárez R L, et al. Spin pumping and anisotropic magnetoresistance voltages in magnetic bilayers: Theory and experiment[J]. Physical review B, 2011, 83(14): 144402.

[185] Ganguly A, Kondou K, Sukegawa H, et al. Thickness dependence of spin torque ferromagnetic resonance in Co75Fe25/Pt bilayer films[J]. Applied Physics Letters, 2014, 104(7): 072405.

[186] Sinova J, Valenzuela S O, Wunderlich J, et al. Spin hall effects[J]. Reviews of Modern Physics, 2015, 87(4): 1213.

[187] Ferré J, Repain V, Jamet J P, et al. Magnetisation reversal dynamics in an ultrathin magnetic film and the creep phenomenon[J]. physica status solidi (a), 2004, 201(7): 1386-1391.

[188] Jang P H, Song K, Lee S J, et al. Detrimental effect of interfacial Dzyaloshinskii-Moriya interaction on perpendicular spin-transfer-torque magnetic random access memory[J]. Applied Physics Letters, 2015, 107(20): 202401.

[189] Siracusano G, Tomasello R, Puliafito V, et al. Micromagnetic analysis of statistical switching

in perpendicular STT-MRAM with interfacial Dzyaloshinskii–Moriya Interaction[J]. IEEE Transactions on Magnetics, 2017, 53(11): 1-5.

[190] Soucaille R, Belmeguenai M, Torrejon J, et al. Probing the Dzyaloshinskii-Moriya interaction in CoFeB ultrathin films using domain wall creep and Brillouin light spectroscopy[J]. Physical Review B, 2016, 94(10): 104431.

[191] Lee O J, Liu L Q, Pai C F, et al. Central role of domain wall depinning for perpendicular magnetization switching driven by spin torque from the spin Hall effect[J]. Physical Review B, 2014, 89(2): 024418.

[192] Ferré J, Grolier V, Kirilyuk A, et al. Magnetization reversal in ultra-thin films with perpendicular anisotropy[J]. Journal of the Magnetics Society of Japan, 1995, 19: S1_79-83.

[193] www.comsol.com.

List of Abbreviations

AF	antiferromagnetic
AGM	alternating gradient magnetometer
AHE	anomalous Hall effect
BLS	Brillouin light scattering
BW	Bloch wall
CCD	charge coupled device
CIDWM	current-induced domain wall motion
DC	direct current
DLT	damping-like torque
DMI	Dzyaloshinskii-Moriya interaction
DRAM	dynamic random-access memory
DW	domain wall
FIB	focused ion beam
FLT	field-like torque
GMR	giant magnetoresistance
HM	heavy metal
ID	irradiation dose
IBE	ion beam etching
LLG	Landau-Lifshitz-Gilbert
MAE	magnetic anisotropy energy
ML	monolayer
MOKE	magneto-optical Kerr effect
MRAM	magnetic random-access memory
MTJ	magnetic tunneling junction
NW	Néel wall
PMA	perpendicular magnetic anisotropy
SHA	spin Hall angle
SHE	spin Hall effect
SIMS	secondary ion mass spectroscopy
SOC	spin-orbit coupling
SOT	spin-orbit torque
SQUID	superconducting quantum interface device
SRAM	static random-access memory
STT	spin-transfer torque
TEM	transmission electron microscopy
TMR	tunnel magnetoresistance
VSM	vibrating sample magnetometer

List of Publications

Journals

[1] **X. Zhao,** B. Zhang, N. Vernier, X. Zhang, M. Sall, T Xing, L. Herrera Diez, C. Hepburn, L. Wang, G. Durin, A. Casiraghi, M. Belmeguenai, Y. Roussigné, A. Stashkevich, S. Mourad Chérif, J. Langer, B. Ocker, S. Jaiswal, G. Jakob, M. Kläui, W. Zhao and D. Ravelosona, "Enhancing domain wall velocity through interface intermixing in W-CoFeB-MgO films with perpendicular anisotropy", *Applied Physics Letters*, **2019**, 115, 122404, doi: 10.1063/1.5121357 (**IF: 3.521, JCR: Q1**)

[2] **X. Zhao**, X. Zhang, H. Yang, W. Cai, Y. Zhao, Z. Wang and W. Zhao, "Ultra-efficient spin–orbit torque induced magnetic switching in W/CoFeB/MgO structures", *Nanotechnology*, **2019**, 30, 335707; doi:10.10.1088/1361-6528/ab1c02 (**IF: 3.399, JCR: Q1**)

[3] W. Zhao, **X. Zhao**, B. Zhang, K. Cao, L. Wang, W. Kang, Q. Shi, M. Wang, Y. Zhang, Y. Wang, S. Peng, J.-O. Klein, L. A. de Barros Naviner, D. Ravelosona, "Failure Analysis in Magnetic Tunnel Junction Nanopillar with Interfacial Perpendicular Magnetic Anisotropy", *Materials*, **2016**, 9(1): 41; doi: 10.3390/ma9010041 (**IF: 2.972, JCR: Q2**) (**First student author**)

[4] S. Peng, W. Kang, M. Wang, K. Cao, **X. Zhao**, L. Wang, Y. Zhang, Y. Zhang, Y. Zhou, K. L. Wang, W. Zhao, "Interfacial Perpendicular Magnetic Anisotropy of 1x nm Tunnel Junctions for Large-Capacity STT-MRAMs", *IEEE Magnetics Letters*, **2017**, 8, 1-5, doi: 10.1109/LMAG.2017.2693961 (**IF: 1.672, JCR: Q3**)

[5] B. Zhang, A. Cao, J. Qiao, M. Tang, K. Cao, **X. Zhao**, S. Eimer, Z. Si, N. Lei, Z. Wang, X. Lin, Z. Zhang, M. Wu, W. Zhao, "Influence of heavy metal materials on magnetic properties of Pt/Co/heavy metal tri-layered structures", *Applied Physics Letters*, **2017**, 110(1): 012405; doi: 10.1063/1.4973477 (**IF: 3.521, JCR: Q1**)

[6] Y. Wang, H. Cai, L. A. de Barros Naviner, Y. Zhang, **X. Zhao**, E. Deng, J-O. Klein, W. Zhao, "Compact Model of Dielectric Breakdown in Spin-Transfer Torque Magnetic Tunnel Junction", *IEEE Transactions on Electron Devices*, **2016**, 63(4), 1762-1767; doi: 10.1109/TED.2016.2533438 (**IF: 2.704, JCR: Q2**)

[7] Y. Wang, H. Cai, L. A. de Barros Naviner, **X. Zhao,** Y. Zhang, M. Slimani, J.-O. Klein, W. Zhao, "A process-variation-resilient methodology of circuit design by using asymmetrical forward body bias in 28 nm FDSOI", *Microelectronics Reliability*, **2016**, 64: 26-30; doi: 10.1016/j.microrel.2016.07.073 (**IF: 1.483, JCR: Q3**)

[8] M. Wang, Y. Zhang, **X. Zhao**, W. Zhao, "Tunnel Junction with Perpendicular Magnetic

Anisotropy: Status and Challenges, " *Micromachines*, **2015**, 6(8), 1023-1045; doi: 10.3390/mi6081023 (**IF: 2.426, JCR: Q3**)

Conferences

X. Zhao, N. Vernier, L. Herrera Diez, M. Sall, C. Hepburn, G. Durin, A. Casiraghi, M. Belmeguenai, Y. Roussigné, A. Stashkevich, S. Cherif, J. Langer, B. Ocker, W. Zhao and D. Ravelosona, "Enhancement of domain wall velocity in He^+ irradiated W-CoFeB-MgO films with perpendicular anisotropy" [C], Joint Magnetism and Magnetic Materials-IEEE International Magnetics Conference (Joint MMM-INTERMAG), Washington, DC, USA, January 14-18, 2019. (**Oral presentation**, AC-10)

Patents

W. Zhao, **X. Zhao**, X. Lin, B. Zhang, N. Lei, A. Cao, "An integrated system and application method of Ultra-thin film preparation, interface characterization and manipulation" [P], CN106555166 B, 2018-9-21 (First student author)

Workshops and Summer schools

[1] New Trends in Chiral Magnetism, École Polytechnique Fédérale de Lausanne, Lausanne, Switzerland, August 21-24, 2018

[2] Introductory course on Magnetic Random Access Memory (InMRAM), Spintec, Grenoble, France, July 2-4, 2018

[3] IEEE Magnetic Society Summer School, Santander, Spain, June 19-23, 2017.

Résumé en Français

La réduction continue des nœuds technologiques CMOS (*Complementary Metal Oxide Semiconductor*) entraine des problèmes de consommation d'énergie du à l'augmentation des courants de fuite et du trafic de données. Pour résoudre ces problèmes majeurs, l'utilisation de mémoires non volatiles a reçu beaucoup d'attention dans les centres de recherche académiques et industriels. En particulier, les mémoires MRAM (*Magnetic Random Access Memory*) non volatiles basées sur des jonctions tunnel magnétiques (*MTJ, Magnetic tunnel junction*) font parties des mémoires émergentes les plus prometteuses. Les jontions tunnel magnétiques peuvent être commutées par un mécanisme de couple de transfert de spin (*STT, spin transfer torque*) ou de couple de spin-orbite (*SOT, spin-orbit torque*), les rendant compatible avec la technologie CMOS. La MRAM est une technologie très prometteuse, en terme de vitesse de commutation, d'endurance infinie et de densité ultime, ce qui permet d'envisager le remplacement des SRAM (*Static Random Access Memory*) et DRAM (*Dynamic Random Access Memory*) qui arrivent à leurs limites physiques. Les MRAM basées sur une commutation par STT sont actuellement commercialisées pour des applications aux mémoires embarquées alors que la dernière génération basée sur une commutation de l'aimantation induite par SOT est la plus prometteuse en terme de faible densité de courant et de rapidité.

La structure typique pour les dispositifs basés sur une commutation par SOT est composée d'une couche ferromagnétique (*FM, ferromagnetic*) en contact avec une couche de métal lourd (*HM, heavy metal*) et une couche d'oxyde. Dans ces structures, l'effet d'interface devient pré-dominant dans la mesure où l'épaisseur des couches est de l'ordre du nanomètre. Dans ce cas, l'anisotropie magnétique venant des interfaces FM/Oxide et HM/FM est plus forte que celle de volume, entrainant un axe de facile aimantation perpendiculaire au plan (*PMA, perpendicular magnetic anisotropy*). Un autre phénomène fortement étudié aujourd'hui, est l'existence d'un couplage d'échange entre les atomes magnétiques et les atomes du métal lourd qui donne lieu à la présence de l'interaction de *Dzyaloshinskii-Moriya (DMI).* Cette interaction est responsable de l'existence de solitons topologiques tels que les parois chirales ou les skyrmions. D'autre part, les inhomogénéités à l'interface peuvent induire une distribution spatiale des propriétés magnétiques (PMA, DMI, ...) qui peut avoir une influence importante sur les processus de retournement de l'aimantation.

L'objectif principal de cette thèse est de clarifier l'influence de la structure des interfaces

sur le DMI et la dynamique de parois de domaine dans les couches minces et les nanodispositifs SOT à anisotropie magnétique perpendiculaire. Afin de manipuler la structure des interfaces, nous avons utilisé en particulier l'irradiation ionique par des ions légers qui permet de contrôler les propriétés structurales de films minces à l'échelle atomique.

Deux types de structures ont été étudiées: Ta (3 nm) / MgO (1 nm) / $Co_{20}Fe_{60}B_{20}$ (t) / Ta (2 nm) / Ru (5 nm) et W (4 nm) / $Co_{20}Fe_{60}B_{20}$ (t) / MgO (2 nm) / Ta (3 nm). Ces deux structures présentent une forte anisotropie perpendiculaire, et elles sont potentiellement intéressantes pour les dispositifs de SOT du à la présence de DMI et à la possibilité de les intégrer dans des jonctions tunnel pour la lecture.

Pour la première structure, nous avons étudié l'anisotropie magnétique perpendiculaire en en fonction des conditions de dépôt et de recuit, ainsi que de l'épaisseur de la couche de CoFeB. Pour caractériser les propriétés magnétiques nous avons utilisé différentes techniques telle que le VSM (*Vibrating-sample magnetometer*), le SQUID (*superconducting quantum interference device*) et un microscope à effet Kerr. En parallèle, la Microscopie électronique en transmission (*TEM, Transmission Electron Microscopy*), la réflectivité de rayons X (XRR *X-ray reflectivity*) et la diffraction de rayons X (*X-ray diffraction*) ont été utilisées pour caractériser la morphologie des couches.

La première structure ayant un DMI faible, cette thèse a essentiellement porté sur sur le mélange d'interface induit par irradiation pour la seconde structure. En complément des mesures sus-mentionnées, le DMI, la propagation de parois dans le régime de creep et la commutation induite par SOT ont été étudiés par microscopie à effet Kerr, par BLS (*Brillouin light spectroscopy*) et par mesure de transport électrique.

Nous avons d'abord mis en évidence le rôle dominant et direct de la structure des interfaces dans plusieurs expériences. Tout d'abord, la réduction de la pression d'Ar pendant la croissance permet d'améliorer la PMA dans les couches de Ta-CoFeB-MgO en raison d'une interface moins désordonnée et plus lisse. D'autre part, l'anisotropie magnétique atteint un maximum puis diminue avec la température de recuit qui a aussi une forte influence sur le mélange et la planéité des interfaces.

En plus du contrôle de la structure d'interface en variant les conditions de pulvérisation cathodique et de recuit, l'irradiation par des ions légers est une autre méthode qui permet d'ajuster les propriétés magnétiques en induisant un mélange aux interfaces. Nous avons monté que dans les structures de W-CoFeB-MgO, un mélange limité aux interfaces induit par l'irradiation permet de réduire d'un facteur deux le champ de dépiégeage des parois

magnétiques tout en maintenant une valeur élevée de l'anisotropie et du DMI. Nous avons aussi démontré que l'anisotropie de l'interface K_i et le DMI se comportent de la même façon en fonction du mélange aux interfaces. Ceci indique qu'ils ont une origine commune: le couplage spin-orbite à l'interface HM/FM, comme le montre la figure 1.

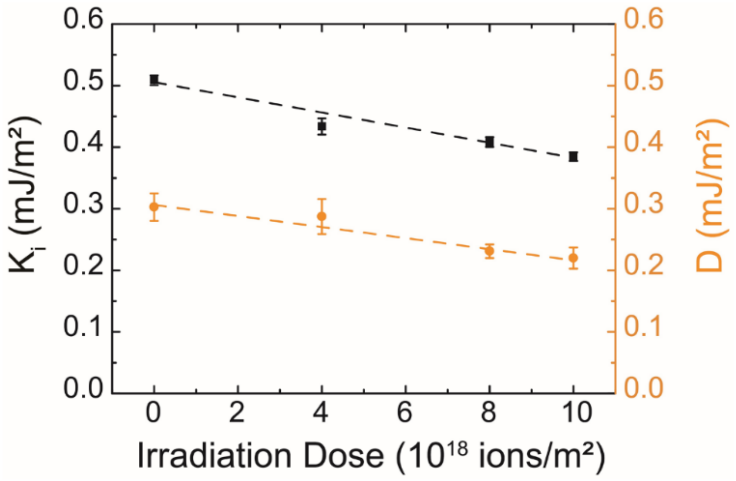

Figure 1. Anisotropie d'interface énergie K_i (carrés noirs) et DMI (carrés orange) en fonction de la dose d'irradiation dans une structure de W-CoFeB-MgO. Une dose elevée correspond à un mélange plus important aux interfaces

La dynamique de propagation de parois et la commutation d'aimantation induite par SOT ont été étudiées dans les structures de W-CoFeB-MgO avant et après un traitement par irradiation. Les mesures indiquent que la vitesse de parois magnétiques dans le régime de creep varie fortement en raison du mélange d'interface induit par l'irradiation. On observe que la vitesse de paroi de domaine augmente d'un facteur 4 après l'irradiation, ce qui est compatible avec une réduction de la force de piegeage (figure 2). Nous avons démontré que cette réduction de la force de piegeage des parois magnétiques est lié à un lissage de l'interface W-CoFeB du au mélange induit par l'irradiation.

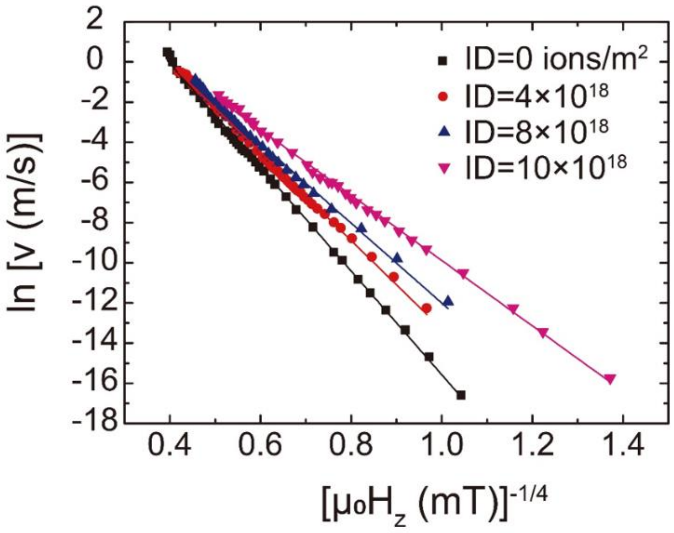

Figure 2. La vitesse de parois magnétiques en fonction du champ magnétique perpendiculaire $H_z^{-1/4}$ pour différentes doses d'irradiation.

Nous avons fabriqué des barres de Hall afin de mesurer la commutation de l'aimantation induite par SOT. Le centre des croix de Hall a été irradié afin de diminuer localement l'anisotropie. Nous avons observé une réduction de 60% de la densité de courant critique après l'irradiation (figure 3) correspondant au retournement des croix de Hall irradiés.

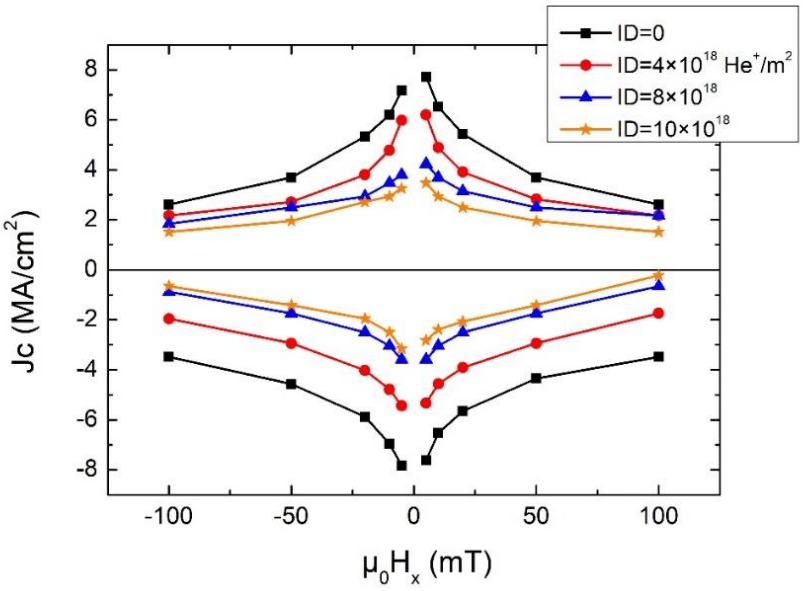

Figure 3. Diagramme de phase de la densité de courant critique en fonction du champ magnétique et pour différentes doses d'irradiation

Le processus de commutation a été confirmé par microscopie à effet Kerr (Fig. 4) qui montre une nucléation de parois induit par SOT puis une propagation dans la partie irradiée.

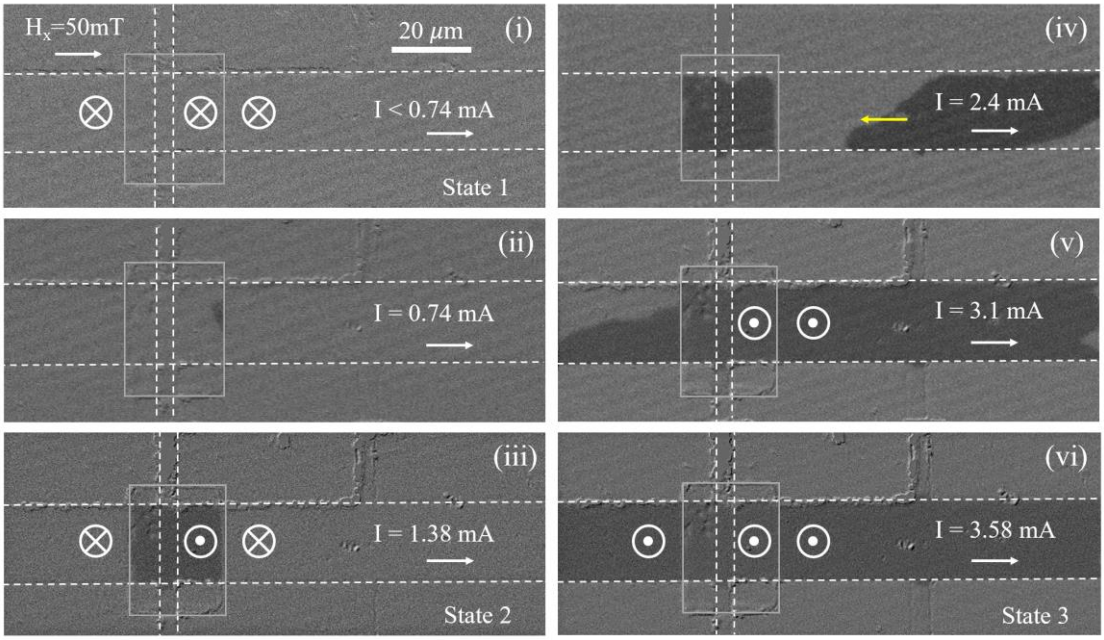

Figure 4. Images de microscopie à effet Kerr montrant le processus de commutation de l'aimantation induite par le SOT dans la barre de Hall sous un champ magnétique de 50 mT dans le plan. Les lignes pointillées blanches indiquent la piste magnétique et la barre de Hall. Le carré gris correspond à la zone d'irradiation. La flèche jaune en (iv) indique la direction de propagation de la paroi du domaine.

ÉCOLE DOCTORALE
Physique et ingénierie : électrons, photons, sciences du vivant (EOBE)

Titre: Etude des effets d'interfaces sur le retournement de l'aimantation dans des structures à anisotropie magnétique perpendiculaire

Mots clés: Spintronique, interfaces, anisotropie magnétique perpendiculaire, parois magnétiques, couple de spinorbite, irradiation

Résumé: Les mémoires MRAM (Magnetic Random Access Memory) sont l'une des technologies émergentes visant à devenir un dispositif de mémoire «universelle» applicable à une grande variété d'applications. La combinaison du couple de spin-orbite (SOT) résultant de l'effet Hall de spin (SHE) et de l'interaction de Dzyaloshinskii – Moriya (DMI) aux interfaces entre un métal lourd et une couche ferromagnétique s'est révélée être un mécanisme efficace pour induire une propagation de parois magnétiques chirales à des faibles densité de courant. Les dispositifs à parois magnétiques devraient constituer la prochaine génération de supports d'information en raison de leur potentiel pour des densités de stockage très elevées. Cependant, une limitation cruciale est la présence de défauts structuraux qui piègent les parois magnétiques et induisent des courants de seuil élevés ainsi que des effets stochastiques importants. L'origine du piégeage résulte de la présence de défauts structuraux aux interfaces entre la couche magnétique ultra-mince et les autres couches (isolants et/ou métaux lourds) qui induisent une distribution spatiale des propriétés magnétiques comme l'anisotropie magnétique perpendiculaire (PMA) ou le DMI. Comprendre l'influence de la structure des interfaces sur la propagation de parois et sur le DMI en particulier est cruciale pour la conception de futurs dispositifs basse consommation.
C'est dans ce contexte très novateur que mon doctorat s'est focalisé sur la manipulation de la structure des interfaces dans des couches ultra-minces à anisotropie magnétique perpendiculaire. Des structures de CoFeB-MgO ont été utilisées afin de mieux comprendre l'impact de la structure des interfaces sur l'anisotropie, le DMI, la propagation de parois et les phénomènes de SOT. L'approche innovante que nous avons utilisée est basée sur l'irradiation par des ions légers pour contrôler le degré de mélange aux interfaces. Sous l'effet du mélange induit par l'irradiation, nous avons observé dans des structures de W-CoFeB-MgO une forte augmentation de la vitesse de parois dans le régime de creep, compatible avec une réduction de la densité des centres de piegeage. Nous avons aussi démontré que l'anisotropie de l'interface K_i et le DMI mesuré par propagation assymmétrique de parois se comportent de la même façon en fonction du mélange aux interfaces.
Finalement, nous avons fabriqué des barres de Hall afin de mesurer la commutation de l'aimantation induite par SOT. Le centre des croix de Hall a été irradié afin de diminuer localement l'anisotropie. Nous avons observé une réduction de 60% de la densité de courant critique après l'irradiation correspondant au retournement des croix de Hall irradiés par propagation de parois. Notre étude fournit de nouvelles pistes concernant le développement de mémoires magnétiques à faible consommation, de dispositifs logiques et neuromorphiques.

Université Paris-Saclay
Espace Technologique / Immeuble Discovery
Route de l'Orme aux Merisiers RD 128 / 91190 Saint-Aubin, France

ÉCOLE DOCTORALE
Physique et ingénierie : électrons, photons, sciences du vivant (EOBE)

Title: Study of Interface Effects on Magnetization Reversal in Magnetic Structures with Perpendicular Magnetic Anisotropy

Keywords: Spintronics, interface, perpendicular magnetic anisotropy, magnetic domain wall, spin-orbit torque, irradiation

Abstract: Magnetic Random Access Memory (MRAM), as one of the emerging technologies, aims to be a "universal" memory device for a wide variety of applications. The combination of the spin orbit torque (SOT) resulting from the spin Hall effect (SHE) and the Dzyaloshinskii–Moriya interaction (DMI) at interfaces between heavy metals and ferromagnetic layers has been demonstrated to be a powerful mean to drive efficiently domain-wall (DW) motion, which are expected to be the promising next generation of information carriers owing to ultra-low driving currents and ultra-fast DW motion. However, the crucial limitation of SOT induced domain wall motion results from the presence of pinning defects that can induce large threshold currents and stochastic behaviors. Such pinning defects are strongly related to structural inhomogeneities at the interfaces between the ultra-thin ferromagnetic layer and the other materials (insulator and/or heavy metals) that induce a spatial distribution of magnetic properties such as perpendicular magnetic anisotropy (PMA) or DMI. Therefore, understanding the role of the interface structure on DW motion and DMI is crucial for the design of future low power devices.

It is under this innovative context that my Ph.D. research has focused on the manipulation of interface structure in ultra-thin magnetic films with perpendicular magnetic anisotropy. CoFeB-MgO structures have been used in order to understand the impact of interface structure on anisotropy, DMI, domain wall motion and SOT phenomena. The innovative approach we have used in this PhD research is based on light ion irradiation to control the degree of intermixing at interfaces. In W-CoFeB-MgO structures with high DMI, we have observed a large increase of the DW velocity in the creep regime upon He^+ irradiation, which is attributed to the reduction of pinning centres induced by interface intermixing. Asymmetric in-plane field-driven domain expansion experiments show that the DMI value is slightly reduced upon irradiation, and a direct relationship between DMI and interface anisotropy is demonstrated. Using local irradiated Hall bars in SOT devices, we further demonstrate that the current density for SOT induced magnetization switching through DW motion can be significantly reduced by irradiation. Our finding provides novel insights into the development of low power spintronic-memory, logic as well as neuromorphic devices.

Université Paris-Saclay
Espace Technologique / Immeuble Discovery
Route de l'Orme aux Merisiers RD 128 / 91190 Saint-Aubin, France